

Robust Quantitative Magnetization Transfer Magnetic Resonance Imaging in the Presence of Radiofrequency Field Inhomogeneities

Mathieu Boudreau, M.Sc.
Department of Biomedical Engineering
McGill University, Montreal, Canada
December 14th, 2017

A thesis submitted to McGill University in partial fulfillment of the
requirements for the degree of Doctor of Philosophy

© Mathieu Boudreau, 2017

Contents

CONTENTS	2
LIST OF FIGURES	6
LIST OF TABLES	11
ACKNOWLEDGEMENTS	12
PREFACE.....	14
CONTRIBUTION OF AUTHORS	15
OTHER PUBLICATIONS.....	16
ABSTRACT.....	18
RÉSUMÉ	20
ORIGINAL CONTRIBUTIONS.....	22
CHAPTER 1 INTRODUCTION.....	23
1.1 MOTIVATION	23
1.2 OBJECTIVES	25
1.3 THESIS OUTLINE	26
CHAPTER 2 BACKGROUND	28
2.1 MULTIPLE SCLEROSIS.....	28
2.1.1 <i>Overview</i>	28
2.1.2 <i>Role of MRI in MS</i>	30
2.2 QUANTITATIVE MR IMAGING.....	31
2.2.1 <i>Tissue Relaxation Properties (T_1, T_2)</i>	31
2.2.2 <i>Field Properties (B_0, B_1)</i>	36
2.3 MAGNETIZATION TRANSFER IMAGING.....	42

2.3.1	<i>Two-Pool Model of MT</i>	42
2.3.2	<i>MTR and MT_{sat}</i>	45
2.3.3	<i>Quantitative Magnetization Transfer Imaging</i>	49
CHAPTER 3	<i>B₁</i> MAPPING FOR BIAS-CORRECTION IN QUANTITATIVE T₁ IMAGING OF THE BRAIN AT 3T USING STANDARD PULSE SEQUENCES	56
3.1	PREFACE	56
3.2	ABSTRACT	59
3.3	INTRODUCTION	60
3.4	MATERIALS AND METHODS	62
3.4.1	<i>Measurements</i>	63
3.4.2	<i>B₁ Mapping</i>	65
3.4.3	<i>T₁ Mapping</i>	67
3.4.4	<i>Data Analysis</i>	67
3.5	RESULTS	68
3.6	DISCUSSION	75
3.7	ACKNOWLEDGMENTS.....	80
CHAPTER 4	<i>B₁</i>-SENSITIVITY ANALYSIS OF QUANTITATIVE MAGNETIZATION TRANSFER IMAGING	81
4.1	PREFACE	81
4.2	ABSTRACT	84
4.3	INTRODUCTION	84
4.4	METHODS.....	87
4.4.1	<i>Simulations</i>	87
4.4.2	<i>Sensitivity Analysis</i>	89
4.4.3	<i>B₁-Sensitivity of qMT in Healthy Subjects</i>	90

4.4.4	<i>B₁</i> Method Comparison	93
4.5	RESULTS	94
4.5.1	<i>Simulations</i>	94
4.5.2	<i>Sensitivity Analysis</i>	97
4.5.3	<i>B₁-Sensitivity of qMT in Healthy Subjects</i>	98
4.5.4	<i>B₁ Mapping Method Comparison</i>	101
4.6	DISCUSSION	103
4.7	CONCLUSION	106
4.8	APPENDIX A.....	106
4.9	ACKNOWLEDGEMENTS	109
CHAPTER 5 SENSITIVITY-REGULARIZATION OF THE CRAMÉR-RAO LOWER BOUND TO MINIMIZE <i>B₁</i> NONUNIFORMITY EFFECTS IN QUANTITATIVE MAGNETIZATION TRANSFER IMAGING.....		110
5.1	PREFACE	110
5.2	ABSTRACT	113
5.3	INTRODUCTION	114
5.4	THEORY	116
5.5	METHODS.....	118
5.5.1	<i>Uniform Protocols</i>	119
5.5.2	<i>Protocol Optimization</i>	120
5.5.3	<i>Monte Carlo Simulations</i>	121
5.6	RESULTS	123
5.6.1	<i>Uniform Protocols</i>	123
5.6.2	<i>Protocol Optimization</i>	125
5.6.3	<i>Monte Carlo Simulations</i>	129

5.7	DISCUSSION	132
CHAPTER 6 CONCLUSION.....		137
6.1	SUMMARY.....	137
6.2	FUTURE WORK	140
BIBLIOGRAPHY		143

List of Figures

- Figure 2-1. Simplified pulse sequence diagrams of two T_1 mapping techniques: Inversion Recovery (IR) and Variable Flip Angle (VFA). TR: repetition time, TI: inversion time, α : excitation flip angle, IMG: image acquisition (k-space readout), SPOIL: spoiler gradient. 34
- Figure 2-2. Simplified pulse sequence diagrams for three widely used B_1 mapping methods: Double Angle (DA), Actual Flip angle Imaging (AFI), and Bloch-Siegert shift (BS). TR: repetition time, α : excitation flip angle, Δ : off-resonance frequency, IMG: image acquisition (k-space readout), SPOIL: spoiler gradient. 38
- Figure 2-3. Two-pool model of the magnetization transfer effect. a – example relative spectral lineshapes for “free pool” hydrogen (e.g. in water) and “restricted pool” hydrogen (e.g. macromolecules in myelin). b – evolution of the magnetization of the two pools during the exchange process. $M_{0,f}$: equilibrium magnetization of the free pool, $M_{z,f}$: longitudinal magnetization of the free pool, $M_{0,r}$: equilibrium magnetization of the restricted, $M_{z,r}$: longitudinal magnetization of the restricted pool, k_f : magnetization transfer exchange rate from the free pool to the restricted pool, k_r : magnetization transfer exchange rate from the restricted pool to the free pool, $R_{1,f}$: longitudinal relaxation rate of the free pool, $R_{1,r}$: longitudinal relaxation rate of the restricted pool. 43
- Figure 2-4. Energy level (left) and magnetization (right) diagrams of restricted and free pool hydrogen a) at thermal equilibrium, b) after an off-resonance RF pulse that pumps energy into the restricted pool, and c) after cross-relaxation/MT-exchange, which distributes excess spin energy from the restricted pool amongst both spin populations through dipolar coupling (spin remain in the same pool) or chemical exchange (spin switch pools). 44
- Figure 2-5. Pulse sequence diagram for a pulsed MT-weighted spoiled gradient echo (SPGR) pulse sequence with a Gaussian MT pulse shape. RF: radiofrequency pulse, SS: slice-selective gradient, PE: phase-encoding gradient, RO: readout gradient, AQ: data acquisition..... 46
- Figure 2-6. Sled and Pike qMT model for a pulsed MT-weighted spoiled gradient echo (SPGR) pulse sequence experiment. (Reproduced with permission from Mag. Res. Med. 46, 923-931 (2001) [145]. Copyright 2001 John Wiley and Sons)..... 52

Figure 3-1. Tissue classification maps (black = 0%, gray = 100%) of a healthy subject calculated from INSECT [172] using MP-RAGE T_{1w} data ($1 \times 1 \times 1\text{mm}^3$) and resampled to $2 \times 2 \times 5\text{mm}^3$. Tissue percentages were estimated by calculating the ratio of INSECT tissue-classified voxels (1mm^3) for a given tissue type (WM, GM, CSF) that were located inside the corresponding low-resolution voxels ($2 \times 2 \times 5\text{mm}^3$), for which the quantitative maps (B_1 , T_1) were acquired.....	64
Figure 3-2. Normalized histograms of single-slice unfiltered B_1 (a) and T_1 (b) map values masked for WM in six healthy subjects. The abbreviation “n.u.” stands for normalized units.....	70
Figure 3-3. a: Acquisition images for each acquired B_1 method: Ref. DA (reference single-slice double angle), AFI (actual flip angle imaging), BS (Bloch-Siegert shift), and EPI-DA (double angle using an interleaved multislice EPI acquisition). b: Unfiltered single-slice B_1 maps, and corresponding WM-masked VFA T_1 maps fitted using flip-angles scaled voxelwise using each B_1 map. The “Nominal” column represents VFA T_1 fitting using no B_1 correction ($B_1 = 1\text{ n.u.}$).....	70
Figure 3-4. Unfiltered (a) and Gaussian filtered (b) B_1 maps of a single subject. (c) Relative differences between unfiltered and filtered maps shown as percent difference maps.....	73
Figure 3-5. Whole-brain coverage of axial MP-RAGE T_{1w} slices, unfiltered AFI B_1 maps, and unfiltered EPI-DA B_1 maps in one subject.....	74
Figure 4-1. Quantitative measurements used in our magnetization transfer (MT)-prepared spoiled gradient quantitative MT study. Solid arrows are used for required measurements; dotted arrows are used for specific methods of a particular measurement. The double angle (DA) method is an explicitly measured B_1 map. $B_{1,\text{Flat}}$ maps are generated using a single value in all voxels. Variable flip angle (VFA) is a T_1 mapping methods that also requires B_1 as a support measurement, unlike inversion recovery (IR).....	92
Figure 4-2. Simulated differences (%) in fitted quantitative magnetization transfer (qMT) F values in the presence of a wide range of B_1 and T_1 errors ($B_{1,\text{true}} = 1\text{ n.u.}$, $T_{1,\text{true}} = 0.9\text{ s}$). The superimposed lines plot the T_1 distribution for a B_1 -independent T_1 mapping method (inversion recovery [IR], solid line, and variable flip angle [VFA], dashed line). n.u. = normalized units.....	95

Figure 4-3. Simulated errors (%) in fitted quantitative magnetization transfer (qMT) parameters for $\pm 30\%$ B_1 errors (a: pool size ratio [F], b: magnetization exchange rate [k_f], c: free pool T_2 [$T_{2,f}$], d: restricted pool T_2 [$T_{2,r}$]). Fits using a B_1 -independent T_1 measure (inversion recovery [IR]) are shown in red, and those using variable flip angle (VFA) T_1 mapping are shown in blue. The IR curve in d) is underneath the VFA line. Note: The solid and dashed lines in Figure 4-3 to show the dependence of IR and VFA T_1 on B_1 . n.u. = normalized units. 96

Figure 4-4. Sensitivity analysis of the magnetization transfer signal relative to B_1 (a, b) and fitting variables (c–f). The plots (note scale changes) show the magnitudes of the sensitivity values (Eq. (4-2)). 98

Figure 4-5. Single-subject comparison of quantitative magnetization transfer parameter maps fitted using double angle and $B_{1,Flat} = 1$ maps using (a) variable flip angle (VFA) T_1 maps corrected using the corresponding B_1 map, and (b) inversion recovery (IR) T_1 maps independent of B_1 100

Figure 4-6. Pooled (all subjects, voxel-wise) whole brain Pearson correlation coefficients (a) and linear regression slopes (b) for qMT F values between the measured double angle B_1 maps and generated $B_{1,Flat}$ maps. IR = inversion recovery; n.u. = normalized units; VFA = variable flip angle. 101

Figure 4-7. B_1 map comparison in a single subject using three different acquisition techniques: double angle method, actual flip angle imaging (AFI), and Bloch-Siegert shift. n.u. = normalized units. 102

Figure 4-8. Single-subject white matter pool-size ratio (F) (a, b) and magnetization transfer (MT) exchange coefficient (k_f) (c, d) distributions for three B_1 mapping methods, using inversion recovery (IR) T_1 mapping (a, c) or variable flip angle (VFA) T_1 mapping (b, d). χ^2 values of the actual flip angle (AFI) and Bloch-Siegert shift (BS) histograms were calculated relative to double angle. 103

Figure 5-1. Simulated qMT parameter errors due to B_1 -inaccuracies ($-30\% < \Delta B_1 < 30\%$) considering a B_1 -independent T_1 measurement (red: IR – inversion recovery) and a B_1 -dependent T_1 -measurement (blue: VFA – variable flip angle). Solid lines are parameter errors calculated from minimizing Eq. (5-2) (first-order approximation of the Taylor expansion),

and dashed lines are parameter errors calculated from fitting the qMT signal according to the Sled & Pike model. The tissue parameters (white matter) and qMT protocol (uniform) were matched to those presented in Boudreau et al. 2017 (see Fig. 3 of the paper). 123

Figure 5-2. Simulated qMT parameter errors estimated from Eq. (5-2) for $\Delta B_1=0.05$ for a wide range of logarithmically-uniform (offsets) qMT protocols. Single (blue, orange, yellow), dual (purple, green, light blue), and triple (red) flip angle combinations of 150° , 400° , and 600° were compared. The number of offset frequencies were uniformly distributed between 300 Hz and 20 kHz, and matched for the total number of acquisition points (# offsets \times # flip angles). 125

Figure 5-3. Sensitivity values (magnitudes) for each qMT fitting parameters (F , k_f , $T_{2,f}$, $T_{2,r}$) and B_1 measurement values considering a B_1 -independent T_1 measure (IR – inversion recovery) and a B_1 -dependent T_1 measure (VFA – variable flip angle). The 312-point protocol shown (12 flip angles \times 26 offset frequencies) represents the initial search-space used for protocol optimization. The sets of sensitivity values for each fitting parameter (a–d) consists of the matrix columns of the Jacobian sensitivity matrix (S_p in Eqs. (5-2) and (5-5)). 126

Figure 5-4. Variance-efficiency (a) and ΔF (b) (Eq. (5-2), $\Delta B_1 = 5\%$) values during the iterative optimization of the sensitivity-regularized Cramér-Rao lower bound equation (Eq. (5-5)). Variance-efficiency is defined here as $(\text{variance} \times \# \text{ acq. points})^{-1/2}$, where the variance is interpreted to be the parameter-normalized Cramér-Rao lower bound (V , Eq. (5-3)). 128

Figure 5-5. Comparison between the 10-point protocols iteratively optimized from a 312-point search space using solely the parameter-normalized CRLB ($\lambda = 0$) and regularized CRLB $_{\lambda=0.5}$. The different flip angle Z-spectrums of the initial optimization search-space are displayed in blue to emphasize the 10-point protocols. The flip angle Z-spectrums (150° to 700° , in 50° increments) range from the highest MT-signal values curve (150°) to lowest (700°). 129

Figure 5-6. Means (a, b) and standard deviations (c, d) of the distribution of pool-size ratios (F) for sets of Monte Carlo simulations (10,000 runs, SNR = 100) fitted using a range of B_1 errors ($\Delta B_1 = \pm 30\%$, $B_1 = 1$ n.u.) and for two sets of qMT parameters (white matter – a,c; grey matter – b, d). Mean F values (% error) shown here were compared relative to the accurate B_1 value case ($\Delta B_1 = 0$), and the grey region represents the region of $\pm 1\%$ relative error. Simulated signal values were generated and fitted for three different 10-point qMT protocols:

Uniform (blue) – two-FA protocol with logarithmically-uniform off-resonance frequency values, CRLB (red) – protocol optimized by iteratively minimizing the increase in the parameter-normalized Cramér-Rao lower bound of the system, and $\text{CRLB}_{\lambda=0.5}$ (yellow) – protocol optimized similar to CRLB, regularized by the estimated error of F (ΔF) in the presence of a B_1 error (Eq. (5-5)). 130

Figure 5-7. Means (a, b) and standard deviations (c, d) of the distribution of pool-size ratio values (F) for sets of Monte Carlo simulations (10,000 runs) fitted using a range of SNR values (25, 50, 75, 100, 150, and 200) and for two sets of qMT parameters (white matter – a,c; grey matter – b, d). Mean F values (% error) shown here were compared relative to data fitted for an ideal SNR case (noiseless), and the grey region represents the region of $\pm 1\%$ relative error. Data was fitted assuming ideal B_1 values ($B_1 = 1$ n.u., solid lines) and a 15% overestimation in B_1 ($B_1 = 1.15$ n.u., dotted lines). Simulated signal values were generated and fitted for three different 10-point qMT protocols: Uniform (blue) – two-FA protocol with logarithmically-uniform off-resonance frequency values, CRLB (red) – protocol optimized by iteratively minimizing the increase in the parameter-normalized Cramér-Rao lower bound of the system, $\text{CRLB}_{\lambda=0.5}$ (yellow) – protocol optimized similar to CRLB, regularized by the estimated error of F (ΔF) in the presence of a B_1 error (Eq. (5-5)). 131

List of Tables

Table 3-1. Linear regression analysis of the pooled WM-masked B_1 and T_1 values (six subjects) for each rapid B_1 method relative to the Ref. DA method.....	71
Table 3-2. Mean and standard deviations of voxelwise percent differences (%) of B_1 and T_1 values in WM relative to the Ref. DA method for all subjects.....	72
Table 4-1. qMT Z-spectra sensitivity comparison metrics for B_1 (accounting for the B_1 -sensitivity of each T_1 method, IR and VFA) and each fitted qMT parameter.	97
Table 4-2. Pooled (all subjects) Pearson correlation coefficients and linear regression slopes for qMT values comparing measured DA B_1 maps and fictitious $B_{1,\text{Flat}} = 1$ maps ^a	100
Table 5-1. qMT tissue parameters used to simulate white matter and grey matter tissue values in the Monte Carlo simulations. The parameter definitions are: F – pool-size ratio, k_f – exchange rate constant, $T_{1,f}$ – longitudinal relaxation time of the free pool, $T_{1,r}$ – longitudinal relaxation time of the restricted pool, $T_{2,f}$ – transverse relaxation time of the free pool, $T_{2,r}$ – transverse relaxation time of the restricted pool. The fitting parameters for qMT are F, k_f , $T_{2,f}$, and $T_{2,r}$; $T_{1,f}$ is calculated from the observed T_1 and the fitting parameters, and $T_{1,r}$ is conventionally fixed to 1 s.....	122
Table 5-2. qMT protocols used in the Monte Carlo simulations. The repetition times, excitation flip angles, and number of acquisitions were matched for all protocols. The Uniform protocol is a two MT flip-angle with logarithmically uniform off-resonance frequencies. The CRLB protocol was optimized using Eq. (5-5) with the regularization parameter set to 0, and $\text{CRLB}_{\lambda=0.5}$ was optimized using a regularization parameter of 0.5.....	122

Acknowledgements

First and foremost, I would like to express my sincerest gratitude to my PhD advisor, Professor Bruce Pike, for all his guidance and support over the course of this degree. The mentorship you offered me was an invaluable experience that I will carry with me throughout my career. Thank you for letting me be increasingly autonomous as this project progressed, and for guiding in the right direction when I sometimes veered off track. I'd like to also thank the other members of my PhD committee, Dr. Douglas Arnold and Professor Robert Funnell, for your guidance and advice at every stage of this thesis work.

I am indebted to all the staff who I've leaned on during a variety of circumstances throughout these years. Thank you to Prof. Pike's administration coordinators (Naomi Takeda, Jennifer Chew, and Christa Collie) for all the hard work and rapid problem-solving you did for me, whether I was aware of it or not at the time. Thank you to all the staff of McGill's Department of Biomedical Engineering, particularly Pina Sorrini, Daniel Caron, and Nancy Abate. Thank you to the McConnell Brain Imaging Center's research assistants, Ilana Leppert and Michael Ferreira, for all the technical support you provided me throughout the years, and most importantly for the assistance you gave me during my initial transition into the lab.

Thank you to all the past and present members of our research group, for creating a rich learning environment full of fruitful ideas, and who were always open to sharing their expertise and insights: Eva Alonso-Ortiz, Silvain Beriault, Avery Berman, Jennifer Campbell, Halleh Ghaderi, Ye Gu, Ives Levesque, Yuhan Ma, Ethan MacDonald, Clarisse Mark, Erin Mazerolle, Melany Mclean, Nikola Stikov, Christine Tardif, and Marika Wallenburg. Special thanks to my deskmate, Yuhan Ma, for your patience while entertaining all my questions, debugging session, general

comments, and ideas. Sincere thanks to Prof. Nikola Stikov, a close collaborator on several projects within and beyond this thesis work, for all your great insights, your contagious enthusiasm for collaboration, and your strong encouragement to contribute to the world of open science. Lastly, thank you to Marika Wallenburg, a close colleague and friend, who passed away while also pursuing her PhD in our lab.

This work could not have been possible without the following sources of funding: the Natural Sciences and Engineering Research Council of Canada (NSERC) Alexander Graham Bell Canada Graduate Scholarship (CGS-D3), the McGill Biomedical Engineering Department Recruitment Award, the International Society for Magnetic Resonance in Medicine (ISMRM) Educational Stipend, the endMS Summer School program, and the McGill Biomedical Engineering Department Travel Award. This research was also funded by my PhD advisor's (Bruce Pike) research and operating grants from NSERC and the Canadian Institutes of Health Research (CIHR).

Last but not least, thank you to all my family and friends who supported me throughout this journey. I am immensely grateful to my wife, Gabrielle Lapointe, for your patience, support, and encouragement all these years. To my father, Valéri Boudreau, for igniting my passion of experimental science at an early age, by sharing your skills and time with me when I participated in science expos as a kid. And to my mother, Joanne Boudreau, for noticing and nourishing my interest in mathematics and physics, providing me with several math and logic exercise books during our visits bookstores and libraries, and for getting me a career day visit to the Physics and Astronomy Department of l'Université de Moncton, which gave me my first taste of academia.

Mathieu Boudreau

December 14th, 2017

13

Preface

The original research presented in this Ph.D. thesis is composed of the following three peer-reviewed international journal articles:

1. **Mathieu Boudreau**, Christine L. Tardif, Nikola Stikov, Wayne Lee, John G. Sled, G. Bruce Pike, “*B_I Mapping for Bias-correction in Quantitative T₁ Imaging of the Brain at 3 Tesla Using Standard Pulse Sequences*”, Journal of Magnetic Resonance Imaging, 46:1673-1682 (2017).
2. **Mathieu Boudreau**, Nikola Stikov, G. Bruce Pike, “*B_I-Sensitivity Analysis of Quantitative Magnetization Transfer Imaging*”, Magnetic Resonance in Medicine, 79: 276-285 (2018).
3. **Mathieu Boudreau** and G. Bruce Pike, “*B_I-Sensitivity Analysis of Quantitative Magnetization Transfer Imaging*”, Submitted to Magnetic Resonance in Medicine.

This thesis was written with the assumption that its readers already have a good fundamental background of MRI theory, the details of which are not presented here. Additional material to bridge the gap between basic MRI physics and the advanced quantitative MRI concepts required for understanding the original research work reported in this thesis is presented in the background section (Chapter 2).

Contribution of Authors

I am the first author of the three manuscripts included in this thesis. As such, I designed the studies, acquired the data, processed and analyzed the data, wrote (or customized) the majority of the simulation and analysis code needed, and wrote the manuscripts. The contributions of the co-authors of these articles are listed below.

- **Christine L. Tardif, PhD:** Previously implemented some of the quantitative imaging pulse sequences used (Actual Flip angle Imaging and spoiled Variable Flip Angle) as well as some data analysis code (for the Bloch-Siegert shift technique). Provided guidance during the planning stage of the study (Chapter 3). Edited the manuscript prior to submission (Chapter 3).
- **Nikola Stikov, PhD:** Provided general guidance throughout the studies (Chapters 3 and 4), and some data analysis code (Variable Flip Angle and Actual Flip angle Imaging). Edited the manuscripts prior to submission (Chapter 3 and 4).
- **John G. Sled, PhD:** Assisted in the implementation of the echo-planar imaging double angle B_1 mapping sequence on our scanner (Chapter 3). Edited the manuscript prior to submission (Chapter 3).
- **Wayne Lee, MSc:** Assisted in the implementation of the echo-planar imaging double angle B_1 mapping sequence on our scanner (Chapter 3). Edited the manuscript prior to submission (Chapter 3).
- **G. Bruce Pike, PhD:** Overall supervision, mentorship, guidance, assistance, and feedback throughout each stage of all three projects presented in this thesis. Edited all manuscripts and the thesis as a whole prior to submission.

Other Publications

The following list of peer-reviewed articles and conference presentations were also produced over the course of this PhD degree, but are not included in the thesis. In addition to the three first-authored manuscripts included this thesis, these other publications total five co-authored peer-reviewed journal articles, five first-authored peer-reviewed conference presentations, and three peer-reviewed co-authored conference presentations.

- J.S.W. Campbell, I.R. Leppert, S. Narayanan, **M. Boudreau**, T. Duval, J. Cohen-Adad, G.B. Pike, N. Stikov, “*Promise and pitfalls of g-ratio estimation with MRI*”, NeuroImage, doi:10.1016/j.neuroimage.2017.08.038 (2017).
- M. Mclean, M.E. MacDonald, R.M. Lebel, **M. Boudreau**, B. Pike, “*Accelerated z-Spectrum Imaging*”, Oral, International Society for Magnetic Resonance in Medicine Meeting (2017).
- J. Campbell, I.R. Leppert, **M. Boudreau**, S. Narayanan, T. Duval, J. Cohen-Adad, G.B. Pike, N. Stikov, “*Myelin g-ratio imaging: promises and pitfalls*”, Poster, International Society for Magnetic Resonance in Medicine Meeting (2016).
- J.-F. Cabana, Y. Gu, **M. Boudreau**, I.R. Levesque, Y. Atchia, J.G. Sled, S. Narayanan, D.L. Arnold, G.B. Pike, J. Cohen-Adad, N. Stikov, “*Quantitative Magnetization Transfer Imaging Made Easy with qMTLab: a Software for Data Simulation, Analysis and Visualisation*”, Concepts in Magnetic Resonance Part A, 44A: 263–277 (2016).
- N. Stikov, J.S.W. Campbell, T. Stroh, M. Lavalée, S. Frey, J. Novek, S. Nuara, M.-K. Ho, B.J. Bedell, R.F. Dougherty, I.R. Leppert, **M. Boudreau**, S. Narayanan, T. Duval, J. Cohen-Adad, P.-A. Picard, A. Gasecka, D. Côté, G.B. Pike, “*In vivo histology of the myelin g-ratio with magnetic resonance imaging*”, NeuroImage, 118:397-405 (2015).
- N. Stikov, J.S.W. Campbell, T. Stroh, M. Lavalée, St. Frey, J. Novek, S. Nuara, M.-K. Ho, B.J. Bedell, R.F. Dougherty, I.R. Leppert, **M. Boudreau**, S. Narayanan, T. Duval, J. Cohen-Adad, P.-A. Picard, A. Gasecka, D. Côté, G.B. Pike, “*Quantitative analysis of the*

myelin g-ratio from electron microscopy images of the macaque corpus callosum”, Data in Brief, 4:368-373 (2015).

- N. Stikov, **M. Boudreau**, I.R. Levesque, C.L. Tardif, J. Barral, G.B. Pike, “*On the Accuracy of T_1 Mapping: Searching for Common Ground.*” Magnetic Resonance in Medicine, 73:514-522 (2015).
- **M. Boudreau**, N. Stikov, G.B. Pike, “ *B_I -Sensitivity Analysis of qMT*”, Poster, International Society for Magnetic Resonance in Medicine Meeting (2015).
- N. Stikov, J. Campbell, **M. Boudreau**, S. Narayanan, T. Stroh, S. Nuara, J. Novek, S. Frey, M.-K. Ho, B. Bedell, G.B. Pike, “*In vivo histology of the myelin g-ratio*”, Poster, Organization for Human Brain Mapping Annual Meeting (2014).
- **M. Boudreau**, N. Stikov, G.B. Pike, “*A B_I -Insensitive qMT Protocol*”, Poster, International Society for Magnetic Resonance in Medicine Meeting (2014).
- **M. Boudreau**, C. Tardif, N. Stikov, G.B. Pike, “*A Comparison of B_I Mapping Methods for T_1 Mapping at 3T*”, Electronic Poster, International Society for Magnetic Resonance in Medicine Meeting (2014).
- **M. Boudreau**, N. Stikov, G.B. Pike, “*Effect of Different T_1 Mapping Techniques on a Quantitative Magnetization Transfer MRI Biomarker for Myelin Density*”, Poster, endMS Conference (2013).
- **M. Boudreau**, N. Stikov and G.B. Pike, “ *T_1 Mapping: Should We Agree To Disagree?*”, Poster, International Society for Magnetic Resonance in Medicine (2013).

Abstract

Quantitative magnetization transfer (qMT) imaging is a magnetic resonance imaging (MRI) technique that has demonstrated considerable promise for multiple sclerosis (MS) research. qMT improves on conventional MRI by probing the macromolecules present in myelin, providing a quantitative estimate called the pool-size ratio, which correlates strongly with myelin density in brain white matter. qMT requires several other quantitative MRI maps for calibration purposes: the main magnetic field (B_0), the radiofrequency field amplitude (B_1), and the longitudinal relaxation time (T_1). These maps can also depend on each other (e.g. some T_1 mapping techniques require B_1), meaning that the impact of B_1 -inaccuracies on the fitted pool-size ratio may depend on the choice of T_1 mapping technique. The focus of this thesis is to characterize and minimize the B_1 -sensitivity of qMT.

The first aim of this thesis was to compare several whole-brain B_1 mapping techniques, their potential sources of inaccuracies, and their impact on a widely used, B_1 -sensitive, T_1 mapping technique (variable flip angle – VFA). This study was done in the context of validating a B_1 mapping technique using a standard MRI pulse sequence and comparing it against two other advanced B_1 -mapping techniques. The second aim was to characterize the B_1 -sensitivity of qMT for two different T_1 mapping techniques: B_1 -dependent (VFA) and B_1 -independent (inversion recovery– IR). qMT data were simulated and fitted for a wide range of B_1 -inaccuracies, and *in vivo* qMT data were acquired in healthy subjects and fitted using both VFA and IR T_1 mapping, along with multiple B_1 mapping techniques. The final aim was to develop an optimization framework for qMT protocols to further improve the robustness against B_1 -inaccuracies. A sensitivity-regularized Cramér-Rao lower bound expression was developed theoretically as an iterative

optimization condition, and the iteratively optimized protocols were tested for a wide range of conditions (signal-to-noise ratios, B_1 -inaccuracies, tissue types) using Monte Carlo simulations. Overall, this thesis presents a characterization and optimization of the robustness of qMT to B_1 -inaccuracies, and concludes that it may be even possible to develop an imaging protocol that could omit B_1 maps altogether without substantially impacting the accuracy of the pool-size ratio estimates.

Résumé

L'imagerie par transfert d'aimantation quantitative (qMT) est une technique d'imagerie par résonance magnétique (IRM) qui s'est avérée très prometteuse pour la recherche sur la sclérose en plaques (SEP). qMT améliore l'IRM conventionnelle en sondant les macromolécules présentes dans la myéline, fournissant ainsi une quantité nommée le rapport taille de réservoirs, qui est fortement corrélée avec la concentration de la myéline dans la substance blanche du cerveau. qMT nécessite plusieurs autres cartes d'IRM quantitatives à des fins d'étalonnage: le champ magnétique principal (B_0), l'amplitude du champ magnétique variable (B_1) et le temps de relaxation longitudinal (T_1). Ces cartes peuvent également dépendre les unes des autres (par exemple, certaines techniques de cartographie T_1 doivent être étalonnées avec B_1), ce qui signifie que l'impact des imprécisions de B_1 sur le rapport taille de réservoirs estimé par ajustement de courbe peut dépendre du choix de la technique de mappage T_1 . L'objectif de cette thèse est de caractériser et minimiser l'impact d'inexactitudes de B_1 envers qMT.

Le premier objectif de cette thèse était de comparer plusieurs techniques de cartographie B_1 capables d'imager le cerveau entier, leurs sources potentielles d'inexactitudes, et leur impact sur une technique de cartographie T_1 très sensible à B_1 (angle de bascule variable - VFA). Cette étude a été réalisée dans le contexte d'une validation de technique de cartographie B_1 en utilisant une séquence d'impulsions IRM standard et en la comparant à deux autres techniques avancées de cartographie B_1 . L'objectif second était de caractériser la sensibilité à B_1 de qMT pour deux techniques différentes de cartographie T_1 : dépendante de B_1 (VFA) et indépendante de B_1 (inversion récupération - IR). Les signaux de qMT ont été simulés et ajustés pour une large plage d'inexactitudes de B_1 , et des cartes qMT ont été acquises chez des sujets sains en utilisant à la fois

la cartographie T_1 VFA et IR, ainsi que de trois techniques de cartographie B_1 . L'objectif final était de développer un cadre d'optimisation des protocoles qMT pour améliorer la robustesse lors de mesures de B_1 inexactes. Une expression théorique de la borne de Cramér-Rao régularisée par la sensibilité a été développée comme condition d'optimisation itérative, et les protocoles optimisés itérativement ont été testés avec des simulations de Monte-Carlo pour une large gamme de conditions (rapports signal sur bruit, inexactitudes de B_1 , types de tissus). Dans l'ensemble, cette thèse présente une caractérisation et optimisation de la robustesse de qMT, conséquent à des inexactitudes de B_1 , et conclut qu'il serait même possible de développer un protocole d'imagerie qMT qui pourrait omettre complètement les cartes B_1 , sans impact considérable sur la précision du rapport taille de réservoirs de qMT.

Original Contributions

The original contributions of the thesis are:

- i. Demonstration that rapid whole-brain B_1 mapping using a standard product imaging sequence provides sufficient quality B_1 maps to produce accurate variable flip angle T_1 maps in white matter, and of similar quality to other widely used advanced B_1 mapping methods that require advanced pulse sequence programming.
- ii. Characterization of the sensitivity of quantitative magnetization transfer (qMT) imaging to B_1 -inaccuracies, and its dependence on the choice of T_1 mapping method.
- iii. Discovery and demonstration that a robust measurement of the qMT biomarker for myelin density (pool-size ratio) can be maintained in the presence of large B_1 inaccuracies if the variable flip angle T_1 mapping method is used in the qMT processing pipeline.
- iv. Development and validation of an iterative optimization strategy of qMT acquisition protocols to minimize the sensitivity to B_1 -inaccuracies, potentially eliminating the requirement of B_1 maps from qMT acquisition protocols.

Chapter 1

Introduction

1.1 Motivation

Quantitative magnetic resonance imaging (MRI) is a subset of MRI techniques that measures specific properties of tissues or physical quantities of the imaging environment. Unlike qualitative MRI techniques that are commonly used in clinical diagnostic radiology, in which the signal intensity of a pixel reflects a combination of several factors that aren't all precisely known and likely vary between scanners or subjects, quantitative MRI promises more specificity, accuracy, and reproducibility for estimates of biological or system properties. These techniques are therefore of particular interest in a research setting. If clinical MRI is conceptualized to be a camera capable of non-invasively capturing pictures of inside a body, quantitative MRI should be interpreted to be the scientific instrument analogue of this camera.

Clinical MRI is used as a diagnostic tool for numerous diseases that could benefit from quantitative MRI to study *in vivo* their biological origin/properties, progression, and treatments. In particular, one neurological disease that has widely benefited from the advent of MRI is multiple sclerosis (MS), an autoimmune disease of the central nervous system that results in the destruction of myelin surrounding axons. This loss of myelin, which acts as an electrical insulator between the Nodes of Ranvier, inhibits efficient signal transmission between neurons, resulting in physical and/or cognitive impairments. MS is a disease that has benefited substantially from MRI, both for diagnostic purposes and to study the disease in research settings. However, clinical MRI protocols for MS are not specific to myelin loss and can have confounding factors. Several quantitative MRI techniques have been developed in an effort to provide better specificity and quantification of

myelin density, one of which is called quantitative magnetization transfer (MT) imaging. Quantitative MT (qMT) improves on clinical MRI techniques by probing the macromolecules of myelin, which is typically unobservable using conventional clinical imaging techniques because of rapid signal decay. One fitted qMT parameter, called the pool-size ratio, has been shown to correlate strongly with myelin density in post-mortem histological studies of MS, and was shown to be significantly different between healthy white matter in control subjects, de/remyelinated MS lesions, and normal appearing white matter in MS patients.

Magnetization transfer is a phenomenon where energy that is selectively transmitted (using radiofrequency (RF) pulses) to hydrogen in macromolecules (“restricted” pool) is transferred to nearby hydrogen in water molecules (“free” pool) through dipolar coupling and/or chemical exchange. Imaging regions containing a higher density of myelin (mostly composed of lipid and protein macromolecules) will result in greater signal loss in the presence of an MT effect. To estimate quantitative tissue values (e.g. pool-size ratio) from qMT data, several MT images must be acquired (typically 10 or more, varying in frequency and amplitude of the MT RF pulse) to fit the data for all the parameters in the mathematical model (typically four independent fitting parameters). Three additional calibration measurements are also necessary: a B_0 map to account for main magnetic field inhomogeneity, a B_1 map for radiofrequency field amplitude inhomogeneity, and a T_1 map to constrain a subset of the fitting parameters. In general, the absence or inaccurate estimate of any of these additional measurements will also result in an error of the estimate of one or more of the quantitative MT fitting parameters. Because the calibration measures do not have perfect accuracy and can be sensitive to different error sources (e.g. technique-dependent artifacts), it is desirable to reduce the sensitivity of the qMT to inaccuracies of the calibration measurements (e.g. from noise or artifacts). However, some of the calibration

methods required for qMT can themselves also require calibration maps. For example, the widely used whole-brain T_1 mapping technique called Variable Flip Angle (VFA) also requires a B_1 map as a calibration measurement, unlike several other T_1 mapping techniques that are B_1 -independent (e.g. inversion recovery – IR). Therefore, the error propagation due to inaccuracies in B_1 maps likely impacts the qMT fitting parameters (in particular, the pool-size ratio) differently depending on which T_1 mapping technique is chosen: B_1 -dependent (e.g. VFA) or B_1 -independent (e.g. IR).

1.2 Objectives

The broad objective of this thesis is to improve the robustness of qMT against potential inaccuracies in measured B_1 , the amplitude of the transmitted radiofrequency electromagnetic field, to improve the estimates of the pool-size ratio, a promising biomarker for myelin density. The rationale is that lower B_1 -sensitivity of the pool-size ratio will improve estimates of the myelin density, since B_1 maps can have regional inaccuracies and artifacts, and could differ between scanning sessions in longitudinal studies. If the B_1 -sensitivity of the pool-size ratio is sufficiently decreased, it might even be possible to develop an imaging protocol in which the B_1 map could be entirely omitted, reducing the total acquisition time. The three specific aims of this thesis are:

- i. To identify and compare potential sources of B_1 -inaccuracies amongst common whole-brain B_1 mapping methods, and investigate the impact of B_1 -inaccuracies on a B_1 -dependent T_1 mapping method (VFA). This will be explored in the context of a study comparing state-of-the-art whole-brain B_1 mapping techniques with a B_1 mapping technique capable of being implemented using standard MRI pulse sequences that are typically available on clinical scanners. The target audience of this manuscript are

researchers who require VFA T_1 mapping in their studies but may omit B_1 correction due to a lack of access to advanced whole-brain B_1 mapping pulse sequences.

- ii. To fully characterize the sensitivity of qMT parameters to B_1 -inaccuracies, and compare the impact of using B_1 -dependent (e.g. VFA) and B_1 -independent (e.g. IR) T_1 mapping techniques. qMT benefits from B_1 maps to correct the MT-sensitizing RF pulse and excitation pulse flip angles for fluctuations in B_1 amplitude that naturally occur in a loaded RF coil. However, T_1 maps, which are required to constrain model parameters in qMT, can also depend on B_1 as a flip angle correction factor, meaning that B_1 -error propagation to qMT will behave differently depending on the choice of T_1 mapping technique. The aim of this study is to determine which T_1 mapping technique results in the lowest B_1 sensitivity of the qMT pool-size ratio estimate for a particular qMT acquisition protocol.
- iii. To develop a qMT acquisition protocol optimization algorithm to further improve the B_1 -insensitivity of the pool-size ratio estimate. Having established the optimal T_1 mapping technique for a given qMT acquisition protocol in objective ii), this objective will explore optimizing the qMT acquisition protocol itself (e.g. off-resonance frequencies and MT flip angles) for improved robustness against B_1 -inaccuracies. A theoretical framework for an iterative optimization algorithm for B_1 -insensitivity will be developed and validated using Monte Carlo simulations for a wide range of specified conditions (e.g. B_1 error, signal-to-noise level, tissue types).

1.3 Thesis Outline

This thesis is written in a manuscript-style format and contains three completed manuscripts of which, as of the time of initial submission, two have been published and one has been submitted, all in peer-reviewed international scientific journals. Chapter 2 contains a brief review of relevant

background material on MS and all the quantitative MRI techniques relevant to the later chapters. This thesis is written with the assumption the reader has a solid foundation in the basics of MRI physics, and this chapter looks to bridge the potential knowledge gap required to understand the specifics of the manuscripts, which deals with more advanced MRI techniques. For a more introductory presentation of MRI physics and pulse sequence concepts, the reader is directed to [1-3]. Chapter 3 contains the first manuscript titled “ B_1 Mapping for Bias-Correction in Quantitative T_1 Imaging of the Brain at 3T Using Standard Pulse Sequences”, which was published in the *Journal of Magnetic Resonance Imaging* (2017, 46: 1673-1682). This work presents a comparison in B_1 (and resulting VFA T_1) map quality between modern whole-brain B_1 mapping pulse sequences typically not available to most researchers/clinicians, with a B_1 mapping technique implemented using only the standard pulse sequences available on most clinical MRI scanners. Chapter 4 contains the second manuscript titled “ B_1 -Sensitivity Analysis of Quantitative Magnetization Transfer”, which was published in the journal *Magnetic Resonance in Medicine* (2018, 79: 276-285). This work presents a characterization of the B_1 -sensitivity of qMT fitted parameters using simulations and *in vivo* measurements, comparing between the use of B_1 -dependent and B_1 -independent T_1 mapping techniques. Chapter 5 contains the last manuscript titled “Sensitivity-Regularization of the Cramér-Rao Lower Bound to Minimize B_1 Nonuniformity Effects in Quantitative Magnetization Transfer Imaging”, which was submitted to the journal of *Magnetic Resonance in Medicine*. This work proposes a sensitivity-regularized approach of the Cramér-Rao lower bound as an optimization condition for minimizing B_1 -sensitivity, and uses Monte Carlo simulations to compare several qMT acquisition protocols to determine their robustness under several conditions (signal-to-noise level, B_1 errors, tissue type). Lastly, Chapter 6 presents a summary of the thesis research and briefly explores potential avenues of future work.

Chapter 2

Background

2.1 Multiple Sclerosis

2.1.1 Overview

Multiple sclerosis (MS) is an autoimmune disease that attacks the central nervous system, damaging the myelin sheets surrounding signal-conducting axons. Canada has one of the highest prevalence of MS in the world [4], where approximately 1 in 340 Canadians have MS [5]. Affecting women disproportionately relative to men (3:1), the rate of incidence has also been observed to increase in the last century [6]. The origin of the disease remains unknown, however both environmental and genetic factors have been shown to increase the risk of getting the disease [7-9]. Populations of countries at higher latitudes have a higher incidence rate of MS [10-12], and individuals are at a higher risk if an immediate family member also suffers from the disease (up to a 25% for identical twins) [13]. Clinical onset of MS mostly begins between the ages of 15 and 40 [14]. Typical physical and cognitive symptoms include vision problems, incoordination, fatigue, difficulty speaking and/or swallowing, pain, spasms, depression, and impaired information processing speeds [15,16]. For most people living with MS, symptoms will initially be temporary (called “attacks” or “flare-ups”) lasting between days up to several months [17], with partial or complete recovery of the disabling symptoms; this stage of MS is called relapse-remitting multiple sclerosis (RRMS). This is followed by the secondary progressive multiple sclerosis (SPMS) stage later on in life, when there is a gradual increase in disability over time, even between attacks. There is no cure for MS. Treatment strategies mostly involve drug therapies to reduce the frequency of attacks (e.g. interferon beta-1a) or hasten recovery after an attack has already begun (e.g.

corticosteroids) [18]. One particularly promising recent Canadian study reported that stem-cell treatment after immunoablation was effective at suppressing long term inflammatory activity in a population with early-aggressive MS [19]. Development of drug therapies that promote remyelination is also an active area of research [20,21], and one of the important challenges in this field is accurately quantifying myelin regeneration *in vivo*. Clinical MRI techniques typically used for diagnosing MS are not specific enough to myelin density for this purpose; quantitative MRI techniques are expected to emerge as a useful tool for remyelination quantification in clinical trials [21,22].

The mechanisms regulating damage in MS are still not completely understood. Broadly, demyelination in MS white matter (WM) lesions is believed to be a result of an immunologically-mediated attack on myelin and oligodendrocytes [23,24]. In active MS lesions, T-cells mistakenly recognize myelin antigens as a foreign body and respond by emitting cytokines, attracting more lymphocytes to the site which disrupts the blood-brain barrier and amplifies the immune system response. Macrophages responding to the released cytokines in turn destroy the myelin sheets. Following this immunological response, if local oligodendrocytes are still present, some remyelination may occur [25]. However, after repeated attacks, irreversible damage will happen, such as axonal transection and degeneration. Several other pathological characteristics have been observed over the course of the disease progression, such as gliosis (scarring), degeneration of the distal segment of transected axons (Wallerian Degeneration), abnormalities in the non-lesion WM (a.k.a. normal appearing white matter – NAWM), brain atrophy, and cortical lesions. Although MS has mostly been described as a WM disease, post-mortem histological studies have reported that cortical grey matter (GM) is also abnormal in MS patients. GM lesions are characterized by

demyelination, axonal and dendritic transection, neuronal apoptosis and limited inflammatory cell content compared to WM lesions [26,27].

2.1.2 Role of MRI in MS

Since 2001, the gold standard criteria for diagnosing MS with MRI has been the McDonald Criteria [28], subsequently getting two revisions in 2005 and 2010 [29,30], with a most recent update in 2016 by the European group MAGNIMS (Magnetic Resonance Imaging in MS) [31]. These criteria require that hyperintense lesions in T₂-weighted MRI images be observed to disseminate in space (three out of the following lesions: at least 3 periventricular, 1 cortical/juxtacortical, 1 infratentorial, 1 optic nerve, or 1 spinal cord) and in time (new lesions relative to a previous scan). In addition, these can both be determined in a single imaging session if a gadolinium-enhancing T₁ lesion is observed, instead of the dissemination in time condition mentioned above (suggesting a disruption in the blood-brain barrier of an early lesion). It's important to note that the presence of a lesion in one part of the brain is not always a predictor of a symptom in the corresponding anatomical/physiological region [32], and that the criteria above is not sufficient in itself for diagnosing MS. MRI provides an additional tool for the diagnostics of MS when supplementing the patient's history and a physical exam performed by a neurologist [33].

Beyond clinical MRI, there are numerous other MRI techniques that are widely used to study MS in research settings, of which we will mention a select few here. Brain atrophy in MS has been shown to correlate more with disability than clinically identified lesions [34,35], and can be estimated with manual or automated tissue segmentation using structural images (e.g. T₂-weighted fluid attenuated inversion recovery – FLAIR) [36,37]. Magnetization transfer and diffusion tensor imaging have both demonstrated better sensitivity to abnormalities in NAWM [38,39], which is

widespread throughout the brain and in regions preceding lesion formation. In post-mortem studies, diffusion and magnetization transfer metrics have both been shown to correlate with myelin content and axonal count [40-42]. Blood-oxygen-level dependent (BOLD) functional MRI (fMRI) has been used in MS to study cognitive dysfunctions and motor/cognitive reorganization during the disease progression [43,44]. Lastly, the role of GM pathology in MS has been increasingly investigated for its possible role in cognitive dysfunction, which become evident during the progressive stage of the disease. Although cortical GM has low myelin content relative to WM, magnetization transfer techniques have demonstrated sensitivity to demyelination in cortical GM lesions [45,46] and as a useful tool to investigate and/or segment cortical lesions and atrophy [47-49].

2.2 Quantitative MR Imaging

Prior to presenting the theory behind quantitative MT (qMT) imaging, which is the focus of this thesis, several other quantitative imaging techniques must be discussed, as qMT requires these measurements for calibration and to constrain fitting parameters. The following section briefly presents the relevant tissue relaxation and field properties of interest for qMT, and explains the measurement techniques for these that are relevant for the manuscripts in the later chapters. Countless other quantitative measurement techniques for these properties exist, but are not presented here.

2.2.1 Tissue Relaxation Properties (T_1 , T_2)

Longitudinal Relaxation Time (T_1)

The longitudinal (or spin-lattice) relaxation time (T_1) is a value that describes the time constant of the longitudinal magnetization's (M_z) return to its thermal equilibrium values (M_0) after excitation.

The longitudinal relaxation rate ($R_1 = 1/T_1$) is sometimes defined instead of T_1 . For the simplest case (e.g. liquids), this behavior is mono-exponential, whereas longitudinal relaxation in solids typically behave non-exponentially [50]. At clinical field strengths, T_1 is approximately several seconds for liquids, near one second for soft tissues, and between one and several seconds for solids. T_1 has a dependency on field strength (proportionally) for the range commonly used to image humans (0.1 to 10 Tesla), because nearby spins must create higher frequency fluctuating magnetic fields to exchange energy (relaxation) due to the higher energy level differences of the spins (Zeeman effect) at high field strength. For example, one study measured T_1 values at 1.5/3.0/7.0 Tesla to be 650/840/1130 ms for WM and 1200/1600/1940 ms for GM. Knowledge of T_1 values for tissues is important in several applications, such as optimizing pulse sequences for signal-to-noise (e.g. in steady-state pulse sequences), to maximize contrast (e.g. FLAIR), and to assist the estimation of other quantitative parameters (e.g. dynamic contrast enhancement – DCE [51,52]). For qMT, T_1 is a necessary parameter to constrain several fitting parameters in the two-pool exchange model, which will be discussed later.

The most widely known T_1 mapping pulse sequence, generally considered the gold standard, is Inversion Recovery (IR) [53,54]. A simplified pulse sequence diagram for IR is presented in Figure 2-1. In this experiment, the longitudinal magnetization is initially inverted with an inversion pulse (180°). After a certain time interval (inversion time – TI) to allow the longitudinal magnetization to relax towards its equilibrium state, an excitation pulse (typically 90°) is applied and magnetization is sampled. By repeating this experiment for several TI values (allowing for a wide range of longitudinal relaxation to occur), an estimate of T_1 can be determined by fitting the image data voxel-by-voxel for each TI. The IR data can be fitted using a number of different equations, and an overview of them are covered in depth by Barral et al. [55]. For complex data (magnitude

and phase), the fitting equation that was demonstrated to be most robust against inaccuracies of the inversion and saturation flip angles and to shorter TRs (shorter than the $\text{TR} \approx 5T_1$ needed for full recovery [55,56]) is the following 5-parameter model, which assuming a single tissue/ T_1 within each voxel:

$$I_n = a + b e^{-\frac{T_{I_n}}{T_1}} \quad (2-1)$$

where a and b are complex fitting parameters and I_n is the complex voxel-wise signal value for the n^{th} TI measurement (TI_n). If only magnitude data is available, a modified version of Eq. (2-1) must be used (see Eqs. 20-24 of Ref. [55]). Note that IR fitting using this equation, unlike some other forms of Eq. 2-1, is very robust against flip angle (i.e. B_1) inaccuracies [55,56]. Inversion recovery is typically limited to a single-slice technique in practice, because it requires a long TR value ($\text{TR} > T_1$) relative to other steady-state techniques. Modified inversion recovery T_1 mapping techniques have been developed to accelerate the acquisition, such as Look-Locker [57,58], which acquires several TIs within a single TR using a small flip angle. Another inversion recovery-based T_1 mapping technique that has become increasingly used, due to its increasing availability on most MRI scanners, is Magnetization Prepared 2 Rapid Acquisition of Gradient Echo (MP2RAGE) [59]. MP2RAGE simultaneously acquires a T_1 -weighted image and a parametric T_1 map, is a B_1 -independend measurements like IR, and has potential applications for MS research [60].

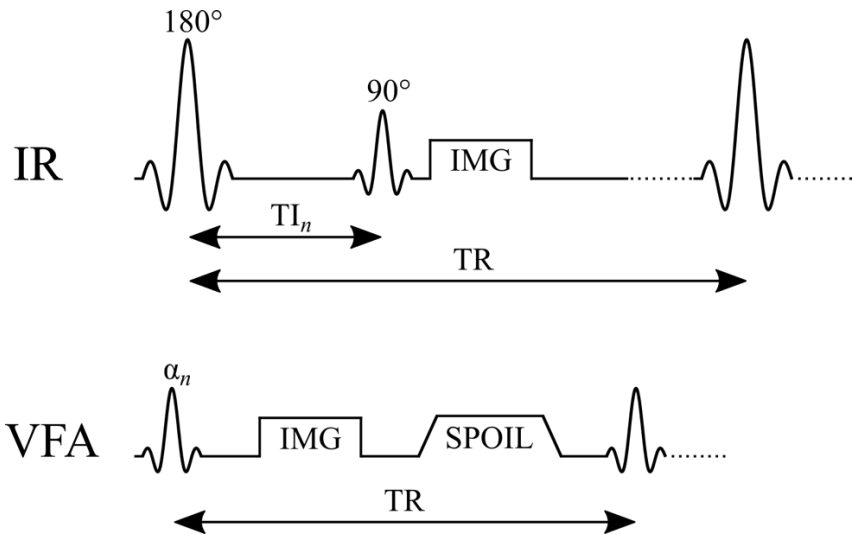


Figure 2-1. Simplified pulse sequence diagrams of two T_1 mapping techniques: Inversion Recovery (IR) and Variable Flip Angle (VFA). TR: repetition time, TI: inversion time, α : excitation flip angle, IMG: image acquisition (k -space readout), SPOIL: spoiler gradient.

Variable Flip Angle (VFA) is an alternative T_1 mapping technique that is capable of mapping T_1 throughout the brain in a clinically feasible acquisition time by using a steady-state spoiled gradient echo (SPGR) imaging approach [61,62]. VFA is sometimes also called DESPOT1 (Driven Equilibrium Single Pulse Observation of T_1) [63]. A simplified pulse sequence diagram for VFA is presented in Figure 2-1. This technique takes advantage of the fact that the SPGR acquisition signal for short TR ($TR \ll T_1$, in the tens of ms range) is very sensitive to the excitation flip angle (α) and T_1 . By acquiring SPGR images using different flip angles, the T_1 values within a voxel can be estimated by fitting the magnitude image data to the steady-state SPGR signal equation:

$$I_n = K \frac{1 - e^{-\frac{TR}{T_1}}}{1 - \cos \alpha_n e^{-\frac{TR}{T_1}}} \sin \alpha_n \quad (2-2)$$

where K is a constant that contains tissue density and receiver coil sensitivity information. Although T_1 could be estimated by fitting Eq. (2-2) using non-linear curve fitting algorithms,

which can be time-consuming for high-resolution whole-brain scans, the terms in this equation can be rearranged so that a solution can be found in terms of a linear equation of the form $y = mx + b$ [56]:

$$\left(\frac{I_n}{\sin \alpha_n} \right) = e^{-\frac{TR}{T_1}} \left(\frac{I_n}{\tan \alpha_n} \right) + \text{constant} \quad (2-3)$$

where the constant does contain T_1/TR values, but not α_n or I_n [61]. Because α_n and TR are both known values, this equation can be solved for T_1 rapidly by linear fitting for a minimum of two flip angles (slope = $\exp\left(-\frac{TR}{T_1}\right)$). However, one caveat of this method is that, due to its sensitivity to the flip angle, it is a B_1 -dependent T_1 mapping method; a B_1 map must be acquired to scale the nominal flip angle to its correct value at every voxel to accurately estimate T_1 using VFA. One advantage of VFA T_1 mapping is that SPGR is a standard pulse sequence on most MRI scanners, making whole-brain T_1 mapping accessible to a wide range of researchers and clinicians. However, the requirement for a B_1 mapping sequence, which is not always available, limits its accuracy in practice [64], particular for DCE studies [52,65,66].

Transversal Relaxation Time (T_2)

The transverse (or spin-spin) relaxation time (T_2) is a time constant that describes the decay of the transverse magnetization (M_{xy}) to its thermal equilibrium value (zero) in the absence of static magnetic field inhomogeneities. For the simplest case (e.g. liquids), this behavior is mono-exponential. T_2 is typically smaller or equal to T_1 , exceeding this limit only under very extreme circumstances [67-70]. In general, T_2 is longer in liquids (~seconds) than in solids (~microseconds), and tissues have an intermediate T_2 range of 25-100 ms [71]. Macromolecules, such as proteins and lipids in myelin, have T_2 values closer to solids (~10 microseconds) [72], due

to a longer rotational correlation time of hydrogen in these molecules [73]. T_2 does not have a strong dependence on field strength (unlike T_1); however, T_2^* – the apparent T_2 in the presence of static field inhomogeneities – does have a strong inversely proportional relationship with main magnetic field strength in humans [74].

qMT does not require a quantitative T_2 map for calibration or as a constraint. However, most qMT models do inherently fit the data for T_2 values. In the two-pool qMT model (to be discussed in detail later), two different T_2 fitting parameters are used: T_2 of the “free-pool” ($T_{2,f}$, on the order of milliseconds) and T_2 of the “restricted pool” ($T_{2,r}$, on the order of microseconds). Some groups choose to fix the $T_{2,r}$ values to the average whole-brain value in their fitting models [75], in part because histopathology studies have not observed a correlation between $T_{2,r}$ and myelin density [42]. Nevertheless, quantitative T_2 mapping is an important technique in and of itself for MS, as it is used to estimate the myelin water fraction (MWF) [76,77], a measure that has also shown to correlate with myelin content [78,79]. MWF is calculated as the ratio of T_2 distribution of water trapped between the myelin layers (~40-50 ms) over the total water content (myelin water and intra/extracellular water, having a $T_2 \sim 100$ ms). These T_2 distributions are typically estimated by fitting multi-component T_2 signal decay curves with multi-echo spin-echo pulse sequences; a comprehensive technical review of MWF acquisition methods is presented in Alonso-Ortiz et al. 2015 [80].

2.2.2 Field Properties (B_0 , B_1)

B_1 Mapping

The transmit radio-frequency (RF) field amplitude (“ B_1^+ ”, but more frequently written simply as “ B_1 ” in the context of quantitative MRI imaging) is a quantity that directly impacts the actual flip

angle that magnetization in a voxel rotates due to on-resonance RF pulses. Spatial inhomogeneity of B_1 leads to spins across the sample experiencing different flip angles, which can lead to differences in image signal intensity throughout a homogeneous sample. Although B_1 can refer to the actual RF magnetic field amplitude (on the order of microteslas [81]), in the context of quantitative MRI it's more frequently represented as a normalized correction factor of the nominal flip angle set by the user at the scanner ($\alpha_{\text{actual}} = B_1 \cdot \alpha_{\text{nominal}}$). B_1 maps are measured as a calibration measurement for quantitative MRI techniques, however some interesting parameters can be derived directly from B_1 maps, such as the electrical conductivity and permittivity of tissues [82] and the local specific absorption rate (SAR) [83]. Even if B_1 is calibrated to a high degree of homogeneity in an empty scanner (e.g. using pickup coils and RF transmit coil design optimization), electrodynamic interactions with tissues (loading/boundaries) will distort the B_1 amplitude profile [84]. For a human head, this pattern is generally elliptical [85]. B_1 -inhomogeneity is also heavily influenced by field strength due to the lengthening of the RF wavelength, worsening at higher field strengths. B_1 inhomogeneity is particularly a challenge at ultra-high fields (7T and higher) due to an RF wavelength on the order of the size of the human head, leading to constructive/destructive interference of the RF wave [86].

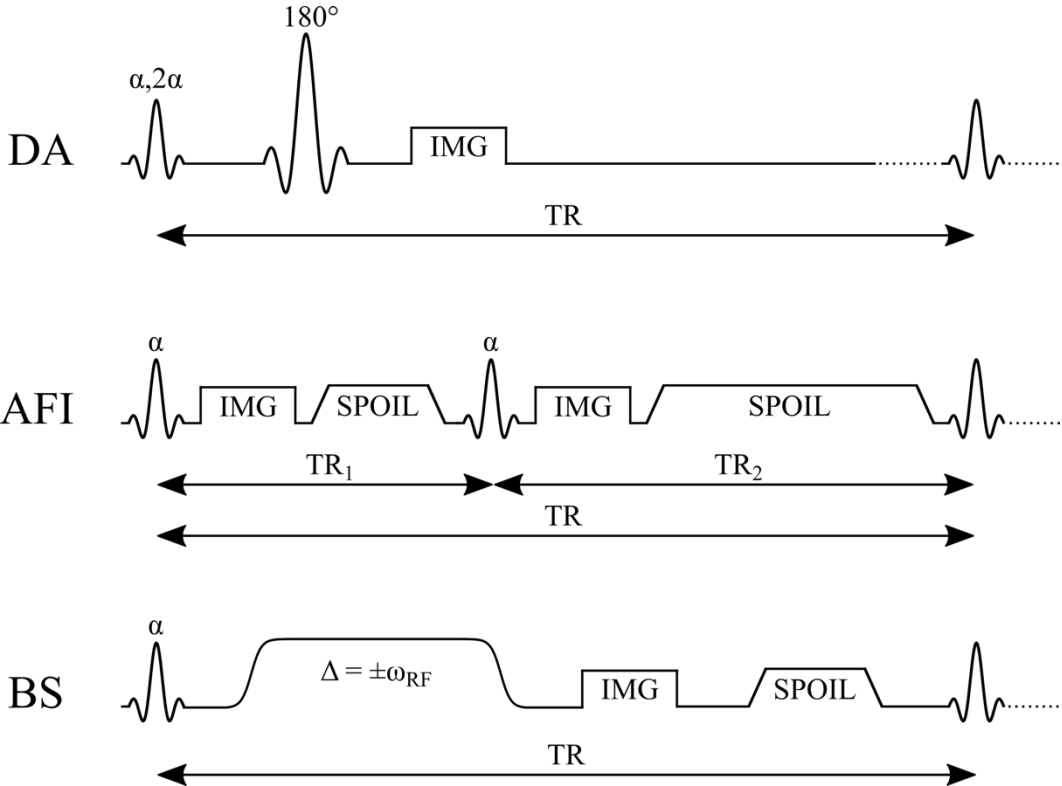


Figure 2-2. Simplified pulse sequence diagrams for three widely used B_1 mapping methods: Double Angle (DA), Actual Flip angle Imaging (AFI), and Bloch-Siegert shift (BS). TR: repetition time, α : excitation flip angle, Δ : off-resonance frequency, IMG: image acquisition (k-space readout), SPOIL: spoiler gradient.

One of the simplest ways to map B_1 *in vivo* is to acquire two otherwise identical images using different excitation flip angles. The actual voxel-wise flip angles can be then estimated with simple trigonometry, by calculating the ratio in expected signal amplitudes. Using the Double Angle (DA) method, one image is acquired with double the excitation flip angle than the other, which results in a very simple equation for a spin-echo acquisition pulse sequence (Figure 2-2) [87,88]:

$$B_1^{DA} = \frac{\arccos\left(\frac{I_{2\alpha}}{2I_\alpha}\right)}{\alpha} \quad (2-4)$$

Another implementation of the DA method uses a spin-echo pulse sequence with an inversion pulse of 2α instead 180° , since some MRI scanner manufacturer set their spin-echo pulse sequence to be α -TE/2- 2α (TE: echo time). The equation for this DA B_1 mapping implementation differs

from the one above, and is presented in Wang et al 2005 [89]. DA B_1 mapping is easy to implement using pulse sequences available on most scanner. However, to minimize the influence of T_1 relaxation in the region of interest, it requires a long TR (at least longer than a few T_1 's [88], but ideally $TR \geq 5T_1$), usually limiting the pulse sequence to a single-slice technique. Other pulse sequence variations of the double angle technique have also been developed, to improve acquisition properties like acquisition time [89,90] and slice profile effects [91].

Numerous rapid whole-brain B_1 mapping techniques have been developed over the years. Two popular and highly cited techniques to have emerged in the past decade are Actual Flip angle Imaging (AFI) [92] and Bloch-Siegert (BS) shift [93] B_1 mapping (Figure 2-2). AFI is a 3D technique implemented using a steady-state imaging approach, whereas BS is a phase-based imaging technique. The AFI pulse sequence is a SPGR-based technique, in which, within a single TR, two acquisitions occur with different delays before the next excitation pulse (TR_1 and TR_2 , $TR_1 \neq TR_2$). The steady-state signal for each acquisition will be different because of the different durations allowed for relaxations relative to the previous excitation pulse. If TR_1 and TR_2 are both very short relative to T_1 , B_1 can be calculated from the following equation [92]:

$$B_1^{AFI} = \frac{\arccos\left(\frac{rn - 1}{n - r}\right)}{\alpha} \quad (2-5)$$

where $r = \frac{I_2}{I_1}$ and $n = \frac{TR_2}{TR_1}$. B_1 calculated from AFI is very insensitive to T_1 values *in vivo* [92], however it can be sensitive to incomplete RF and gradient spoiling [94,95]. The AFI pulse sequence is currently not typically available on most MRI scanners, and must be implemented on-site by an MRI pulse sequence programming expert. Despite some drawbacks, it is used in a wide array of research applications, particularly for B_1 mapping at very high fields strengths [96-99].

BS is a phase-based B_1 mapping technique that uses the Bloch-Siegert shift phenomenon [93]. The Bloch-Siegert shift is a change in precession frequency of spins in the presence of an off-resonance RF field, sufficiently off-resonance so that approximately no longitudinal↔transversal magnetization rotation occurs. Conceptually, the spins in the rotating frame at the off-resonance frequency of the RF pulse experience a non-zero B_z vector field, and far off-resonance this vector component will dominate over the B_1 field in transverse plane, such that the spins will precess about B_z at a rate proportional to the B_1 amplitude. This effect results in a relative phase accruement, which is also dependent on the B_1 amplitude of the off-resonance RF pulse. Typically, BS B_1 mapping is implemented by acquiring two images each using symmetrically off-resonance RF pulses ($\Delta=\pm\omega_{RF}$), applied between the excitation pulse and readout (Figure 2-2). B_1 values can be calculated from this experiment using the following equations [93]:

$$B_1^{BS} = \frac{\sqrt{\frac{\phi_+ - \phi_-}{2K_{BS}}} \int_0^T \gamma B_{1,normalized}(t) dt}{\alpha} \quad (2-6)$$

$$K_{BS} = \int_0^T \frac{(\gamma B_{1,normalized}(t))^2}{2\omega_{RF}} dt \quad (2-7)$$

where ϕ_+ is the voxel phase value for the $\Delta=+\omega_{RF}$ acquisition, ϕ_- is the voxel phase value for the $\Delta=-\omega_{RF}$ acquisition, γ is the gyromagnetic ratio of the spin population, T is the total duration of the off-resonance pulse, α is the excitation pulse flip angle, and $B_{1,normalized}$ is the pulse profile of the off-resonance B_1 pulse ($B_{1,normalized} = B_1/B_{1,max}$). The off-resonance RF pulse is typically very long (~5-10 ms) relative to the excitation pulse, and has a wide Fermi or Gaussian profile so that the spins experience a very small frequency band in practice (as a consequence of Fourier theory). BS also exhibits very low sensitivity to T_1 effects [93]; however, it is dependent

on reliable phase unwrapping, which can be challenging in the presence of phase artifacts like fringe lines and phase poles [100]. Conventional BS imaging has very high SAR, which is a potentially limiting factor for high field applications, although some modifications to the technique have been proposed to make BS feasible at high field strengths [96,101].

B₀ Mapping

The local main magnetic field (B₀) influences the resonant precession frequency of spins. In principle, it is much simpler to quantify B₀ compared to other quantitative MRI parameters. Most scanners come equipped with at least one pulse sequence to acquire a B₀ map (a.k.a. field map); this information is used during the automated shimming process of MRI scanners. The simplest technique used for acquiring B₀ is a basic SPGR pulse sequence executed with two different echo times (TE). Using a phase subtraction technique, B₀ – which in quantitative MRI is usually expressed in terms of a frequency – can be calculated from the following equation [102]:

$$B_0 \equiv \Delta\omega_0 = \frac{\Delta\varphi}{\Delta TE} \quad (2-8)$$

where φ is the phase in radians. For high B₀ or ΔTE values, the phase can exceed ±π radians, and the phase images will require phase unwrapping prior to calculating the difference, which can be challenging if certain artifacts are present (e.g. fringe lines and poles). Also, the B₀ field inhomogeneity can be caused by pulse sequence-specific factors, for example Eddy currents induced in the MRI hardware as a result of strong time-varying magnetic field gradients. Thus, for B₀ correction in quantitative MRI, it may be desirable to use a B₀ mapping pulse sequence that more closely reproduces the magnetic field environment of the quantitative MRI pulse sequence being used.

2.3 Magnetization Transfer Imaging

2.3.1 Two-Pool Model of MT

The largest contribution of signal from conventional MRI experiments originate from hydrogen in water molecules, which is plentiful and dense in most human organs, and generally has a slow transverse signal decay (~10 to 100 ms), allowing sufficient time for an imaging experiment. Hydrogen is also present in numerous other molecules, such as macromolecules (lipids and proteins) in myelin. However, the MRI signal from hydrogen in these macromolecules decays very quickly ($T_2 \sim \mu\text{s}$) due to their semi-solid nature and long rotational correlation times, making it very challenging to directly image the macromolecules of myelin. Another consequence of the short T_2 for these macromolecules is a very broad spectrum of resonant frequencies (~10's of kHz). In the 1970s and 1980s, researchers discovered that by selectively exciting the macromolecular hydrogen with off-resonance RF pulses prior to an NMR/MRI acquisition, longitudinal magnetization from water hydrogen is transferred to nearby macromolecules through a process called cross-relaxation, resulting in a lower MRI signal in regions where there is an abundant quantity of macromolecules near water [103-105]. This discovery lead to the development of the two-pool model of magnetization transfer model (Figure 2-3), where magnetization from hydrogen in water is referred to as the “free-pool”, and macromolecular hydrogen is referred to as the “restricted-pool”.

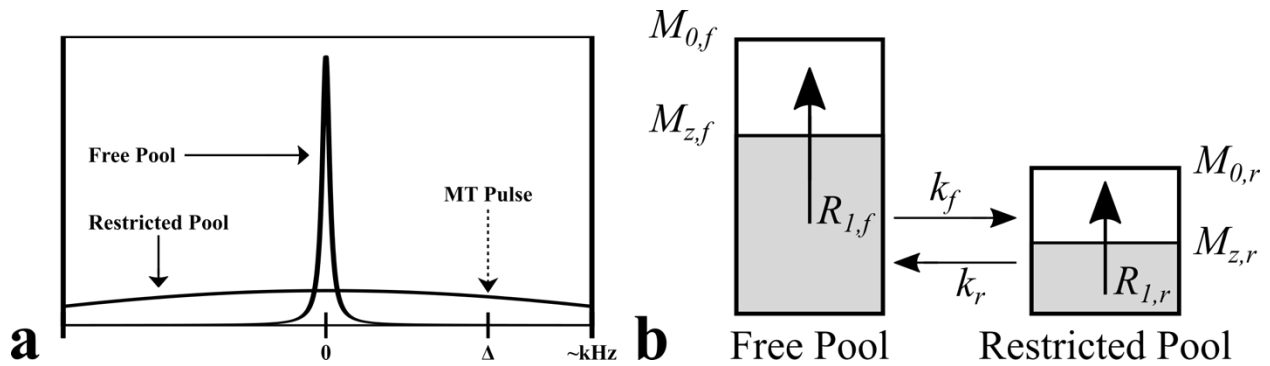


Figure 2-3. Two-pool model of the magnetization transfer effect. a – example relative spectral lineshapes for “free pool” hydrogen (e.g. in water) and “restricted pool” hydrogen (e.g. macromolecules in myelin). b – evolution of the magnetization of the two pools during the exchange process. $M_{0,f}$: equilibrium magnetization of the free pool, $M_{z,f}$: longitudinal magnetization of the free pool, $M_{0,r}$: equilibrium magnetization of the restricted, $M_{z,r}$: longitudinal magnetization of the restricted pool, k_f : magnetization transfer exchange rate from the free pool to the restricted pool, k_r : magnetization transfer exchange rate from the restricted pool to the free pool, $R_{I,f}$: longitudinal relaxation rate of the free pool, $R_{I,r}$: longitudinal relaxation rate of the restricted pool.

Conceptually, the magnetization transfer effect as discussed above and presented in Figure 2-3 is somewhat puzzling, since unlike energy and momentum, the net magnetization is not a conserved quantity. For example, if a 90° excitation pulse is applied followed by a strong crusher gradient, the equilibrium magnetization vector $M_0\hat{z}$ is converted to the null vector $\hat{0}$. In reality, it is more specifically *energy* of the spin populations between the two pools that is exchanged during the MT phenomenon, and the longitudinal magnetization of each pool differ as a result of this energy exchange, leading to an observed magnetization transfer. Figure 2-4 displays the energy level diagrams of two spin populations at three different stages of a magnetization transfer experiment. For simplicity, the relaxation rates of each pools are neglected in this diagram (which in reality are present).

Energy

Magnetization

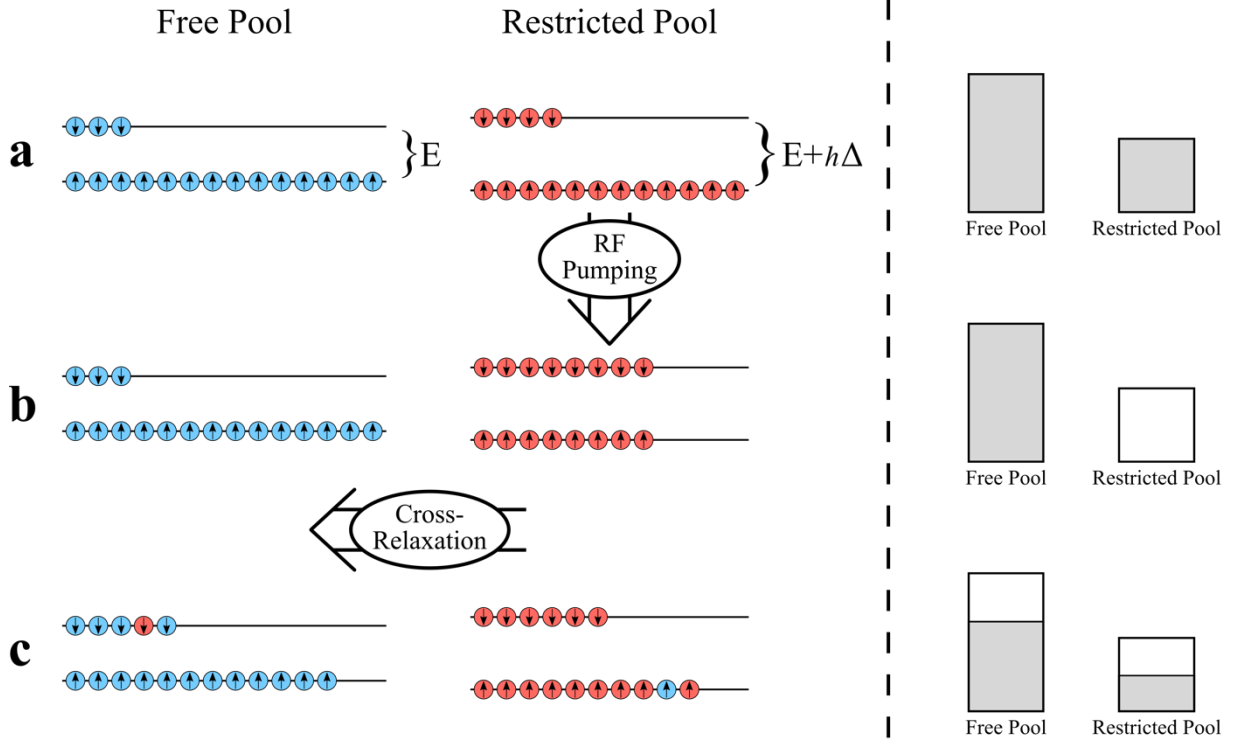


Figure 2-4. Energy level (left) and magnetization (right) diagrams of restricted and free pool hydrogen a) at thermal equilibrium, b) after an off-resonance RF pulse that pumps energy into the restricted pool, and c) after cross-relaxation/MT-exchange, which distributes excess spin energy from the restricted pool amongst both spin populations through dipolar coupling (spin remain in the same pool) or chemical exchange (spin switch pools).

Considering an initial condition of thermal equilibrium, the spin populations for both pools are distributed unevenly between the two energy levels caused by Zeeman splitting for spins in an external magnetic field (Figure 2-4a – left). An excess of spins in the low energy levels result in non-zero total longitudinal magnetization vectors (M_z) of $M_{0,f}$ and $M_{0,r}$ for the free and restricted pools (Figure 2-4a – right). The restricted pool is selectively saturated by using an off-resonance pulse, without impacting the energy of the free pool (Figure 2-4b; however, in practice there is some saturation of the free pool that needs to be modeled). The excess energy pumped into the restricted pool in this example reduces the total longitudinal magnetization vector of the spins to zero. Lastly, over time the excess energy pumped into the restricted pool will dissipate to nearby

hydrogen spins in the free pool by a stochastic process, through phenomena such as dipolar coupling and chemical exchange. The excess energy lost by the restricted pool results in an increase in longitudinal magnetization, while the excess energy gained by the free pool results in a reduction in longitudinal magnetization, resulting into an apparent magnetization exchange from the free pool to the restricted pool. The two-pool model is a simplified version of the phenomenon; a four-pool model (myelin water, intra/extracellular water, myelin semi-solids, non-myelin semi-solids) has also been proposed for MT, as also modeled in MWF imaging. However, it's been shown that the two-pool model is sufficient to model the quantitative MT phenomenon in WM [106]. Lastly, although the description above was framed in terms of an MT experiment, any pulse sequence that exposes macromolecules to off-resonance RF fields can result in an MT effect (sometimes unwanted), such as standard multislice imaging [107,108].

2.3.2 MTR and MT_{sat}

Magnetization Transfer Ratio (MTR)

The simplest and most widely used measure of the magnetization effect is the magnetization transfer ratio (MTR). In this experiment, two images are acquired with (I_{MT}) and without (I_0) an off-resonance RF pulse preceding the imaging pulse sequence, and MTR is the normalized difference of these two images calculated in terms of a percentage:

$$\text{MTR} = \frac{I_0 - I_{MT}}{I_0} \cdot 100 \quad (2-9)$$

As discussed in the previous section, the greater the MT effect (e.g. more macromolecular content), the less I_{MT} values will be, resulting in higher MTR values. In the context of MS, demyelinated lesions are expected to have lower MTR voxel values relative to normal appearing white matter

(NAWM). An example MT imaging pulse sequence (MT-prepared SPGR) is shown in Figure 2-5. In this pulse sequence, a conventional short-TR SPGR pulse sequence is preceded by a long off-resonance RF pulse with a widely shaped pulse envelope. Prior to the excitation RF pulse (on-resonance) of the SPGR imaging sequence, a spoiler gradient is applied to eliminate any potential free-pool (long T_2) magnetization that was excited by the MT pulse and rotated into the transverse plane in addition to any residual transverse magnetization from the excitation pulse of the previous TR. For the MT-off image (I_0), the same pulse sequence timings and gradients are used, but without the off-resonance RF pulse.

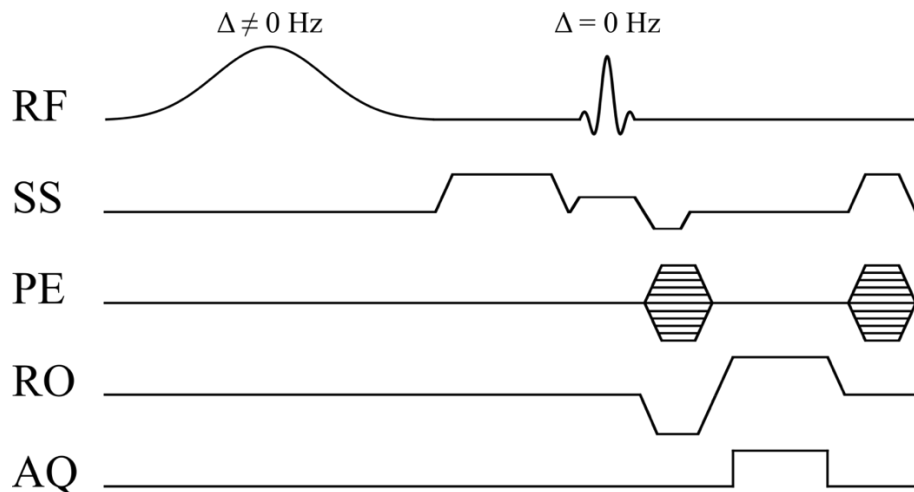


Figure 2-5. Pulse sequence diagram for a pulsed MT-weighted spoiled gradient echo (SPGR) pulse sequence with a Gaussian MT pulse shape. RF: radiofrequency pulse, SS: slice-selective gradient, PE: phase-encoding gradient, RO: readout gradient, AQ: data acquisition.

MTR pulse sequences are available on most clinical MRI scanners, making it an accessible imaging tool for researcher and clinicians. Due to its simplicity in implementation and computation, it is possible to produce a whole-brain high-resolution MTR maps in a clinically feasible time. However, MRI manufacturers often impose a fixed off-resonance frequency, effective MT pulse flip angle, and MT pulse shape envelope to their MT pulse sequences, all of which influence the MT effect and resulting MTR values. Because the values for these parameters

are not standardized between MRI manufacturers, the MTR values for tissues/lesions can differ substantially between imaging sites. One large multi-center study previously observed MTR values at 1.5T in WM ranging between 9% and 51% [109], and as a result standardized protocols have been proposed [110,111]. MTR is not solely sensitive to macromolecular density; it groups all the factors that impact the MT-prepared SPGR steady-state signal into a single value, such that MTR is also sensitive to effects such as B_1 inhomogeneity and local T_1 values. Thus, MTR is typically referred to as a semi-quantitative MRI measure. Researchers have proposed corrective factors for MTR maps, in particular for B_1 inhomogeneity [90,112]. However, requiring a B_1 map increases the acquisition time, and B_1 mapping pulse sequences are not always available on clinical scanners as a default setting, reducing the accessibility of B_1 -corrected MTR for researchers and clinicians. The impact of T_1 on MTR is also an important consideration, as it varies not only between tissues, but also due to other biological processes such as inflammation and edema that can occur in MS lesions [113]. Disassociating these effects with demyelination can be challenging (or impossible) for an MTR measurement. Despite some drawbacks, MTR has been shown to correlate significantly with myelin density and axonal count in post-mortem MS brains using immunohistopathology [41,114], and has been widely used for *in vivo* MS research studies to infer on de/re-myelination monitoring [22,115-117], diffuse NAWM/NAGM and GM pathology [48,118-124], and therapeutic clinical trials [125-128]. Beyond MS applications, several other diseases with neurological manifestations have been studied using MTR, such as schizophrenia [129,130], HIV [131], Alzheimer's disease [132], and major depressive disorder [133].

Magnetization Transfer Saturation (MTsat)

Another semi-quantitative measure of the MT effect is the magnetization transfer saturation (MTsat) value [134]. MTsat is an emerging MT technique with inherent compensation for B_1

profile effects and lower sensitivity to T_1 differences, and has the same potential applications for MS research as were listed above for MTR. Unlike MTR, which is the normalized difference of the steady-state signal with and without an MT-preparation RF pulse, MTsat is an estimate of the fractional longitudinal magnetization reduction caused by the MT pulse within a single TR (after a steady-state has been established). MTsat only requires one additional measurement to the two SPGR-MTR acquisitions; one T_1 -weighted SGPR scan with different TR/α values (\downarrow/\uparrow , respectively) with no MT pulse. From these three measurements (S_{PD} : MT-off SPGR, S_{MT} : MT-on SPGR, S_{T_1} : T_1 -weighted SPGR), MTsat can be calculated directly with the following equations [134,135]:

$$MTsat = \left(A_{app} \cdot \frac{\alpha_{MT}}{I_{MT}} - 1 \right) R_{1,app} TR_{MT} - \frac{\alpha_{MT}^2}{2} \quad (2-10)$$

$$A_{app} = I_{PD} I_{T_1} \frac{TR_{PD} \frac{\alpha_{T_1}}{\alpha_{PD}} - TR_{T_1} \frac{\alpha_{PD}}{\alpha_{T_1}}}{TR_{PD} I_{T_1} \alpha_{T_1} - TR_{T_1} I_{PD} \alpha_{PD}} \quad (2-11)$$

$$R_{1,app} = \frac{1}{2} \cdot \frac{\frac{I_{T_1} \alpha_{T_1}}{TR_{T_1}} - \frac{I_{PD} \alpha_{PD}}{TR_{PD}}}{\frac{I_{PD}}{\alpha_{PD}} - \frac{I_{T_1}}{\alpha_{T_1}}} \quad (2-12)$$

where α is the excitation flip angles in radians, and TR is the repetition times in seconds. MTsat calculated in Eq. (2-10) is a fractional value ($\sim 10^{-2}$), which is sometimes expressed in percentage units (as is done with MTR) by multiplying by 100. Because MTR and MTsat can both be expressed as percentage units, there is a risk of confusion when interpreting MTsat values relative to MTR. MTsat is substantially lower than MTR in tissues (by a factor of ~ 10), because it represents the fractional signal saturation from a single MT pulse and not the overall steady-state

signal differences like MTR. Another caveat of MTsat is that its interpretation is linked to the effective flip angle of the MT pulse, making it challenging to interpret MTsat values reliably between sites if they use different acquisition protocols. Nonetheless, MTsat is very simple to implement, only requires one additional measurement relative to MTR, and could be an accessible alternative to MTR for researchers in need of a semi-quantitative MT measure with more robustness against B_1 and T_1 . MTsat has been shown to correlate better with MS disability levels than MTR in NAWM and the spinal cord [136], and has a more linear correlation with the pool-size ratio (restricted/free) than MTR [137]. It has also been used for other applications, such as g-ratio measurement (ratio of the inner/outer diameter of the myelin sheath of an axon) [137,138], segmentation of deep grey matter structures [139], and hypomyelinating disorders [140].

2.3.3 Quantitative Magnetization Transfer Imaging

Quantitative measurement of the magnetization transfer effect requires a mathematical model describing the evolution of the magnetization/signal throughout an MT experiment. For a two-pool model of exchange (Figure 2-3 and Figure 2-4), the Bloch-McConnell differential equations describing the coupled cross-relaxation of the magnetization vectors of the free and restricted pools are [104,141-145]:

$$\frac{dM_{x,f}}{dt} = -\frac{M_{x,f}}{T_{2,f}} + \Delta M_{y,f} - \text{Im}(\omega_1)M_{z,f} \quad (2-13)$$

$$\frac{dM_{y,f}}{dt} = -\frac{M_{y,f}}{T_{2,f}} + \Delta M_{x,f} - \text{Re}(\omega_1)M_{z,f} \quad (2-14)$$

$$\frac{dM_{z,f}}{dt} = \frac{(M_{0,f} - M_{z,f})}{T_{1,f}} - k_f M_{z,f} + k_r M_{z,r} + \text{Im}(\omega_1)M_{x,f} - \text{Re}(\omega_1)M_{y,f} \quad (2-15)$$

$$\frac{dM_{z,r}}{dt} = \frac{(M_{0,r} - M_{z,r})}{T_{1,r}} + k_f M_{z,f} - k_r M_{z,r} + W M_{z,r} \quad (2-16)$$

$$W = \pi \omega_1^2 G(\Delta, T_{2,r}) \quad (2-17)$$

where Δ is the off-resonance frequency of the RF pulse, $\omega_1 = \gamma B_1$ is a complex and time-varying function of the RF pulse amplitude, k_f is the magnetization exchange rate from the free pool to the restricted pool, k_r is the magnetization exchange rate from the restricted pool to the free pool, $M_{0,f/r}$ is the equilibrium longitudinal magnetization of the free/restricted pool, and W is the transition rate of the restricted pool in the presence of an off-resonance RF pulse (see Figure 2-4a to b) and assumes a shaped RF pulse with a narrow bandwidth (a more general expression for W is presented in Ref. [144]). Note that the transverse components (x/y) of the restricted pool are omitted above, as $T_{2,r}$ is much shorter than the typical experimentation time, and studies have shown these terms can be safely neglected [144,146]. An important quantitative MT parameter that is implicitly included in the equations above is the pool-size ratio, $F = M_{0,r}/M_{0,f}$, where by definition $k_r = k_f/F$. In Eq (2-17), G is the spectral lineshape function of the restricted pool (e.g. Figure 2-3a). Common spectral lineshapes observed in restricted pools are Gaussian for solids and gels (e.g. imaging phantoms) and super-Lorentzian for biological tissues [146]. One important point to note is that the measured longitudinal relaxation rate ($R_1^{obs} = 1/T_1^{obs}$) in the presence of macromolecules differs from the free pool longitudinal relaxation rate $R_{1,f}$, and the relationship between the two is described by:

$$R_{1,f} = R_1^{obs} - \frac{k_f(R_{1,r} - R_1^{obs})}{(R_{1,r} - R_1^{obs}) + \frac{k_f}{F}} \quad (2-18)$$

Equations (2-13) to (2-16) cannot be solved analytically for most quantitative MT pulse sequence experiments. One exception is the case where Eqs. (2.15) and (2.16) are driven to a steady-state using a continuous-wave (“hard” pulse) MT-preparation RF pulse (1 to 5 seconds) prior to data acquisition [143]. However, this technique does not lend itself well to *in vivo* quantitative MT imaging experiments due to its long acquisition times and high SAR. Pulsed MT pulse sequences, initially proposed using binomial RF pulses with zero net flip angle on-resonance [147,148] followed by the more commonly used shaped off-resonance pulses [144,145,149] (e.g. Figure 2-5), were demonstrated to be a practical alternative to CW for *in vivo* quantitative MT imaging. One caveat of using a pulsed approach to qMT is that solving these equations for a pulsed-MT pulse sequence are numerically very difficult, and require exceedingly large computation times to process the several thousand (single-slice) up to several hundred thousand voxels (whole-brain). Several numerical approximations have been proposed to solve Eqs (2.13) to (2.16) [145,150,151] in order to fit qMT data for the unknown model parameters: F , k_f , $R_{1,f}$, $R_{1,r}$, $T_{2,f}$, and $T_{2,r}$. Most pulsed off-resonance qMT models share two features: (1) $R_{1,r}$ is fixed to 1 s^{-1} , as these types of qMT experiments are largely insensitive to $R_{1,r}$ [143], and (2) a T_1 map ($1/R_1^{obs}$) is required to constrain the fitting parameters $R_{1,f}$, F , and k_f using Eq. (2-18) [143,145]. Thus, only four free model fitting parameters remain to be solved in a qMT experiment (F , k_f , $T_{2,f}$, and $T_{2,r}$).

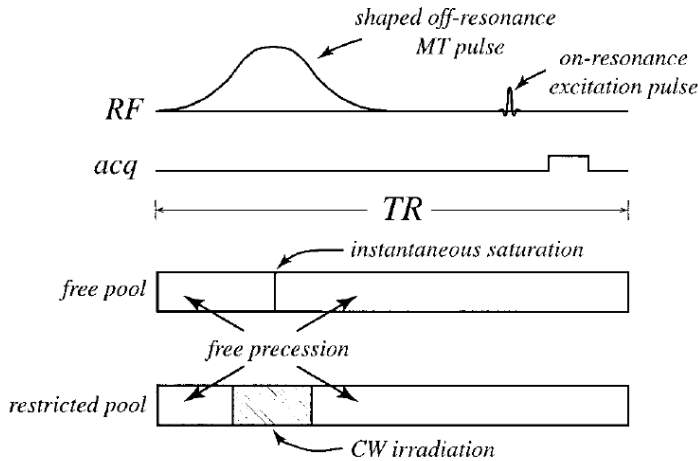


Figure 2-6. Sled and Pike qMT model for a pulsed MT-weighted spoiled gradient echo (SPGR) pulse sequence experiment. (Reproduced with permission from Mag. Res. Med. 46, 923-931 (2001) [145]. Copyright 2001 John Wiley and Sons)

The first qMT fitting model proposed for *in vivo* imaging of all quantitative parameters was introduced in 2001 for a pulsed-MT SPGR experiment [145], and is often referred to as the Sled and Pike model after its authors. The Sled and Pike model has been shown to produce more accurate estimations of qMT fitting parameters compared to other qMT models [152], and is the model used throughout this thesis. Figure 2-6 graphically present the approximations used in this model, which are for a pulsed-MT SPGR experiment (Figure 2-5). The effect of both the excitation and the MT pulse on the free pool is approximated as an instantaneous saturation, which is precomputed prior to fitting the imaging data by solving the equations in the absence of relaxation or exchange between pools for a wide range of effective MT flip angles, Δ , and $T_{2,f}$. The second approximations of the Sled and Pike model is neglecting the effect of the excitation pulse on the restricted pool, and to approximate the shaped MT pulse as a CW pulse of equivalent power and offset frequency. With these assumptions, the evolution of the magnetization can be broken down into event blocks of free precession, CW irradiation at an off-resonance frequency, and instantaneous saturations of the free pool, making it possible to solve the steady-state Bloch equations in a closed-form [144] instead of numerically, substantially improving the fitting time.

To fit the qMT parameters in the model, several MT-weighted SPGR image acquisitions are needed at several different off-resonance frequencies (Δ) and effective MT-pulse flip angles (FA_{MT} , the excitation flip angle that would occur if the RF pulse was applied on resonance, and related to ω_1), in addition to one image without an MT pulse (I_0) for data normalization. Plots of normalized MT-weighted data as a function of off-resonance frequencies for each FA_{MT} are typically referred to as a “Z-spectrum”. In addition to the MT data and T_1 map needed to constrain the model parameters, B_0 and B_1 maps are also typically acquired as corrective factors for Δ and ω_1 , respectively. Open-source software to simulate and fit qMT data using the Sled and Pike model (and several other models) was recently published and released online [153].

The qMT parameter that has demonstrated the most potential for inferring information about tissue abnormalities in MS is the pool-size ratio (F), which is a measure of the restricted pool size of macromolecular content relative to the local water content. In post-mortem MS brains, F has been shown to strongly correlate with myelin content [42], and significant differences in F were measured between WM lesions and NAWM, de- and remyelinated lesions, and between remyelinated lesions and NAWM. This study also suggested that F may be a more specific biomarker for myelin loss than MTR, particularly in NAWM. Several studies have reported significant difference in F *in vivo* between MS lesions and NAWM/controls [145,150], and in the longitudinal evolution of acute MS lesions [154]. In healthy brains, regional variations of F across different WM/GM regions of the brains have been reported [155], and excellent scan-rescan reproducibility has been demonstrated [156]. F has also been a good predictor of de/remyelination in animal models of MS [157,158]. Beyond MS, other potential applications of qMT have been explored, such as Alzheimer’s [159], breast imaging [160], cartilage imaging [161], g-ratio imaging [137,162], and the characterization of dry-cured hams [163].

Fitting qMT data for the four quantitative parameters requires several MT and calibration measurements. Initially, 60 MT-weighted images were acquired (with different TRs, FA_{MT} , Δ values) in addition to one normalization measurement with no MT pulse (for each TR). Subsequent studies demonstrated that the four qMT parameters could be fitted reliably using at least 10 MT-weighted measurements, by using protocol-design optimization [164,165]. These MT-weighted SPGR measurements, in addition to the three calibration measurements (B_0 , B_1 , T_1), mostly made qMT limited to a single-slice technique. However, with the development of parallel imaging and compressed sensing rapid acquisition techniques [166,167], high-resolution whole-brain is rapidly becoming accessible. This means that the calibration measurements (B_0 , B_1 , T_1) used for qMT must also change from single-slice to whole-brain techniques, which may have unintended consequences on qMT parameter estimates. For example, early qMT studies used single-slice T_1 mapping techniques such as Look-Locker (LL) or Inversion Recovery (IR), which are B_1 -independent T_1 mapping methods. For whole-brain qMT imaging, VFA is a more practical choice for T_1 mapping; however, it is a B_1 -dependent technique. Because qMT is also a B_1 -dependent technique, inaccuracies in the B_1 map may impact the qMT fitting estimates differently depending on if a B_1 -independent (e.g. IR) or B_1 -dependent (e.g. VFA) T_1 mapping technique is used. If IR/LL T_1 mapping is used, an error in B_1 will only propagate to qMT through the FA_{MT} and excitation flip angles of the model. Using VFA T_1 , an error in B_1 will propagate through this same pathway, but also through the F/k_f parameter constraint in Eq. (2-18) by an error in the $R_{1,obs}$ estimate. Sled and Pike [145] first reported that using LL at 1.5T, a 10% error in B_1 would result in a 20% error in the estimate for F. Levesque et al. [156] also reported very high coefficient of variations for most qMT parameters in the absence of B_1 and B_0 maps, but they also used the LL methods which is much less B_1 -sensitive than VFA. Underhill et al. [168] briefly mentioned that

B_1 mapping is particularly important for their whole-brain qMT implementation at 3.0T, in particular because they chose to use VFA T_1 mapping, noting that it also depends on B_1 . To the best of our knowledge, a comprehensive study aimed at characterizing the B_1 -sensitivity of qMT under these different circumstances has not been reported, which raises the following three questions: (1) what are some potential sources of B_1 -inaccuracies and how sensitive is VFA to them?, (2) are B_1 -dependent or B_1 -independent T_1 mapping methods better for robust qMT pool-size ratio estimate?, and (3) can qMT acquisition protocols be optimized for reduced sensitivity to B_1 -inaccuracies. These questions are the focus of the manuscripts that are explored in the following three chapters, and of this PhD thesis as a whole.

Chapter 3

B₁ Mapping for Bias-Correction in Quantitative T₁ Imaging of the Brain at 3T Using Standard Pulse Sequences

3.1 Preface

B₁ maps are an essential component of VFA T₁ mapping acquisition protocols. In this context, B₁ maps are used as a voxel-wise flip angle scaling factor for the nominal flip angles that are specified at the scanner for the VFA image acquisitions. Because VFA is 3D technique typically used to map T₁ throughout the brain, whole-brain B₁ mapping techniques that have a short acquisition time are also needed for this application. Several rapid whole-brain B₁ mapping techniques have been proposed, and the two most popular techniques developed over the last decade are AFI and Bloch-Siegert, both having additional advantageous properties (e.g. T₁-insensitivity). However, the major drawback of these techniques is that they are not widely available on most clinical scanners; these pulse sequences must be programmed manually on-site, a time-intensive procedure requiring expertise that may not be available for all users.

The following manuscript, published in the *Journal of Magnetic Resonance Imaging*, describes the comparison of a simple echo planar imaging (EPI)-based double angle (EPI-DA) whole-brain B₁ mapping technique, AFI, and Bloch-Siegert, along with the VFA T₁ maps produced using each B₁ mapping technique. EPI-DA has the advantage of requiring no pulse sequence programming; it can be implemented using standard MRI pulse sequences available on most clinical scanners. Unlike the two later manuscripts, the target audience of this manuscript are researchers who may not have quantitative MRI pulse sequence programming expertise, but require a B₁ map for another technique such as VFA T₁ mapping, which is also easily implementable using standard MRI pulse

sequences. To the best of our knowledge, this is the first paper to quantitatively compare these two advanced B_1 mapping techniques (ASI, BS) and their resulting VFA T_1 maps with a simple whole-brain B_1 mapping technique that can be implemented with a standard MRI pulse sequence. This work is important for researchers who need whole-brain T_1 maps (e.g. for dynamic contrast-enhanced (DCE) imaging), but omit B_1 maps from their acquisition protocols because of a belief that this technique is not easily accessible to them. In addition, this manuscript reports the B_1 maps both with and without B_1 filtering, a post-processing step that is typically done to remove noise and because the B_1 profile is expected to be a slowly varying function. Comparing the filtered/unfiltered B_1 maps of each method provided us with insights on the potential artifacts and noise that could be the source of B_1 -inaccuracies for the later qMT chapters.

B₁ Mapping for Bias-Correction in Quantitative T₁ Imaging of the Brain at 3T Using Standard Pulse Sequences

*Mathieu Boudreau, Christine L. Tardif, Nikola Stikov, John G. Sled,
Wayne Lee, G. Bruce Pike*

McConnell Brain Imaging Centre, Montreal Neurological Institute
3801 University Street, McGill University
Quebec, Canada, H3A 2B4

Journal of Magnetic Resonance Imaging, 46: 1673-1682 (2017)

3.2 Abstract

Purpose: B_1 mapping is important for many quantitative imaging protocols, particularly those that include whole-brain T_1 mapping using the variable flip angle (VFA) technique. However, B_1 mapping sequences are not typically available on many magnetic resonance imaging (MRI) scanners. The aim of this work was to demonstrate that B_1 mapping implemented using standard scanner product pulse sequences can produce B_1 (and VFA T_1) maps comparable in quality and acquisition time to advanced techniques.

Materials and Methods: Six healthy subjects were scanned at 3.0T. An interleaved multislice spin-echo echo planar imaging double-angle (EPI-DA) B_1 mapping protocol, using a standard product pulse sequence, was compared to two alternative methods (actual flip angle imaging, AFI, and Bloch-Siegert shift, BS). Single-slice spin-echo DA B_1 maps were used as a reference for comparison (Ref. DA). VFA flip angles were scaled using each B_1 map prior to fitting T_1 ; the nominal flip angle case was also compared.

Results: The pooled-subject voxelwise correlation (ρ) for B_1 maps (BS/AFI/EPI-DA) relative to the reference B_1 scan (Ref. DA) were $\rho = 0.92/0.95/0.98$. VFA T_1 correlations using these maps were $\rho = 0.86/0.88/0.96$, much better than without B_1 correction ($\rho = 0.53$). The relative error for each B_1 map (BS/AFI/EPI-DA/Nominal) had 95th percentiles of 5/4/3/13%.

Conclusion: Our findings show that B_1 mapping implemented using product pulse sequences can provide excellent quality B_1 (and VFA T_1) maps, comparable to other custom techniques. This fast whole-brain measurement (~2 min) can serve as an excellent alternative for researchers without access to advanced B_1 pulse sequences.

3.3 Introduction

Radiofrequency transmit field (B_1^+) maps, typically termed “ B_1 maps” for brevity, are necessary in several quantitative magnetic resonance imaging (MRI) applications, such as specific absorption rate (SAR) estimation, magnetization transfer (MT) imaging, and quantitative T_1 mapping. Electrical properties tomography (EPT) relies on quantitative B_1 maps to calculate the conductivity (σ) and permittivity (ϵ) of tissue *in vivo* [82], and is an essential step in the estimation of local SAR [83]. MT techniques probe the macromolecular content of tissue, and are often used as an index of myelination in diseases such as multiple sclerosis [42]. Unaccounted B_1 inhomogeneity in certain MT experiments can be an important source of error. For example, B_1 -correction has been shown to improve the quality of MT ratio (MTR) maps [112], due to the sensitivity of MTR to the MT preparation RF pulse power. The longitudinal relaxation time (T_1), one of the fundamental quantities in MRI, is an important input for several other data processing pipelines, such as dynamic contrast enhancement (DCE) imaging [52,66] and quantitative MT [145]. Although some whole-brain T_1 mapping methods boast first-order insensitivity to RF field inhomogeneities [59], others—notably the variable flip angle (VFA) method [169]—are inherently sensitive to inaccuracies in the excitation flip angles (FA). B_1 maps can greatly benefit the accuracy and precision of VFA T_1 maps at high clinical field strengths, (e.g. 3T), where large B_1 amplitude variations are typical in loaded coils [85] (e.g. $\pm 30\%$ for the human brain). The broad range of B_1 applications highlights the need for accurate B_1 mapping techniques, while also balancing other competing interests such as acquisition speed and ease of implementation, particularly in the context of multisite studies.

Substantial efforts have been made to develop rapid whole-brain B_1 mapping techniques in the last decade. Previously, conventional B_1 mapping was done using some variations of the double angle

(DA) method, which consists of two separate gradient-echo or spin-echo measurements with longitudinal magnetization recovery in which the second measurement is performed with double the excitation pulse flip angle [87]. However, conventional DA requires very long repetition times, and was mostly used for single-slice imaging. Advanced pulse sequences have been developed to accommodate whole-brain B_1 mapping. Two of the most popular techniques are actual flip angle imaging (AFI) [92] and Bloch-Siegert shift (BS) mapping [93]. AFI is a steady-state 3D spoiled gradient echo (SPGR) B_1 mapping method based on a dual-TR acquisition ($TR_2 = N * TR_1$, where N is typically an integer on the order of 5), and has been shown to be T_1 -insensitive for most tissues. BS is a phase-sensitive slice-selective B_1 mapping method using a modified SPGR sequence; a high amplitude off-resonance RF pulse between the excitation and readout events induces a phase-shift proportional to the B_1 amplitude. Currently, an important limitation of these methods is their lack of widespread availability as a standard product sequence on clinical scanners. These pulse sequences are typically implemented onsite, a time-consuming process that require pulse sequence programming expertise, and is susceptible to site-specific implementation issues.

The lack of a readily available whole-brain B_1 mapping pulse sequence is a challenge to many researchers, particularly in the context of multi-center studies, resulting in the omission of B_1 mapping in quantitative imaging protocols that would significantly benefit from its inclusion. One such quantitative MRI method is VFA T_1 mapping, which estimates T_1 by fitting the gradient echo images to a function of flip angles, making it inherently sensitive to B_1 -inaccuracies. For example, using a VFA sequence with a 15 msec TR and two flip angles (3° and 20°) [56], an underestimation of the nominal flip angles by 1/5/10/20% results in an overestimation of the fitted T_1 by 2/11/24/57%. Thus, errors in B_1 induce at least twice as large errors in T_1 , and the error increases

nonlinearly. Notably, DCE imaging protocols that use VFA T_1 mapping often omit B_1 correction [52,65], even though B_1 maps have been shown to substantially improve the accuracy of DCE [51,66]. Citing the unavailability of advanced B_1 mapping sequences at their site, other researchers have developed techniques to simulate B_1 maps by normalizing the VFA T_1 image [64] using postprocessing image analysis algorithms [170]. However, a systemic bias in B_1 values (of unknown size) could still be present using this type of image analysis approximation, so measuring B_1 directly should improve the accuracy of the T_1 maps.

The purpose of this work was to evaluate the quality of a fast and simple whole-brain B_1 mapping protocol implemented using a standard EPI pulse sequence. An interleaved multislice spin-echo EPI readout standard product pulse sequence was used to map B_1 with the DA method (EPI-DA) [62,89,171] in a group of healthy human subjects. EPI-DA has not gained as much attraction in comparison to AFI and BS, due to their demonstrated robustness against specific characteristics (e.g. large T_1 values, B_0 inhomogeneity) and their compatibility with higher fields systems that use parallel transmit coils. Yet the ease of implementation of EPI-DA or other similar techniques (e.g. fast spin-echo DA [90]) may make them a good alternative to advanced B_1 methods, which require custom implementations and pulse sequence programming expertise.

3.4 Materials and Methods

All measurements were performed on a 3.0T whole-body MRI scanner (Magnetom TIM TRIO, Siemens, Erlangen, Germany) using a 32-channel phased-array receive-only head coil and whole-body transmit coil.

3.4.1 Measurements

Healthy adult volunteers were scanned in compliance with the guidelines of the Institutional Ethics Committee, and gave written informed consent prior to being scanned for this study. Six healthy adult volunteers were scanned (three females, three males, 29 ± 3 years old). Axial slices were acquired (for 2D measurements) or extracted (from 3D/multislice measurements, with orientations matching the single-slice 2D measurements) parallel to the anterior and posterior commissure (AC-PC) plane, superior to the corpus callosum.

Quantitative analyses of the B_1 and T_1 maps were limited to voxels comprised of white matter (WM), consistent with previous work [90,162]. Two reasons factored into this decision. First, as B_1 maps are typically acquired at low resolution, partial volume effects occur near cortical gray matter (GM) regions and areas adjacent to ventricles. Therefore, there is an insufficient number of voxels that contain pure GM. Second, the partial volume effects in regions containing cerebrospinal fluid (CSF) result in substantially longer mean T_1 values (2–5 sec), so T_1 -sensitive artifacts will vary in severity between B_1 methods that have different intrinsic sensitivity to long T_1 and CSF flow. Adequately comparing B_1 methods in GM and CSF is a specialized topic that requires higher resolution and/or longer scan-times, which is beyond the scope of this work.

Whole-brain T_1 -weighted magnetization-prepared rapid gradient-echo (MP-RAGE) 3D volumes ($1 \times 1 \times 1\text{mm}^3$) were acquired: repetition time (TR) = 2300 msec, echo time (TE) = 3.32 msec, inversion time (TI) = 900 msec, iPAT factor = 2 (GRAPPA), bandwidth (BW) 5230 Hz/Px, 5 min 30 sec scan time. Tissue classification maps (WM, GM, CSF) were obtained via Intensity Normalized Stereotaxic Environment for the Classification of Tissue (INSECT)[172] using the MP-RAGE data with the ICBM-152 atlas. All necessary preprocessing steps (nonuniformity

correction, skull-stripping, etc.) were done using the standard pipeline of the MINC Tool Kit (v. 1.9.11, McConnell Brain Imaging Center, Montreal Neurological Institute, Montreal, Canada). Tissue percentage maps (WM, GM, CSF), at the low resolution ($2 \times 2 \times 5\text{mm}^3$) for which the quantitative maps (B_1, T_1) were acquired, were estimated by calculating the ratio of high-resolution INSECT tissue-classified voxels (1mm^3) that had the center of their voxels located within the corresponding $2 \times 2 \times 5\text{mm}^3$ voxels, using a majority voting analysis (75% threshold). Figure 3-1 shows a tissue classification maps of WM, GM, and CSF for a healthy subject. The classification maps show that for a $2 \times 2 \times 5\text{mm}^3$ resolution, very few voxels consisted of single-tissue GM or CSF, reaffirming our reasoning to exclude these areas in our study. To generate the WM masks for each subject, a >75% binary threshold was applied to the tissue percentage maps; since there can be 20 high-resolution voxels (1mm^3) that have their centers located in a low-resolution voxels ($2 \times 2 \times 5\text{mm}^3$), a >75% threshold represents the case that no more than four non-WM INSECT tissue classified voxels (out of 20) are located within a voxel of the WM mask. Lastly, note that the WM mask were only used to mask-out non-WM voxels after the B_1 maps were calculated, and are not required to calculate any of the B_1 maps described in the following section.

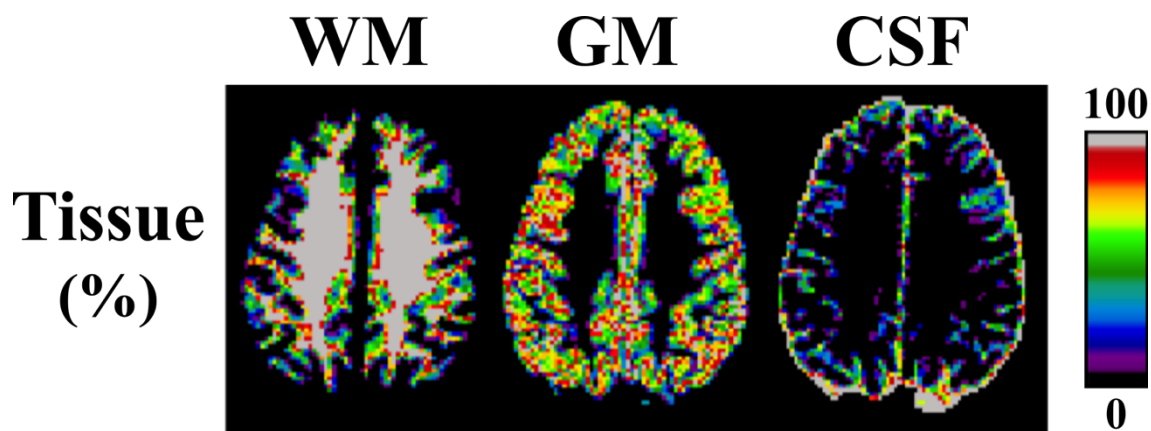


Figure 3-1.Tissue classification maps (black = 0%, gray = 100%) of a healthy subject calculated from INSECT [172] using MP-RAGE T_{1w} data ($1 \times 1 \times 1\text{mm}^3$) and resampled to $2 \times 2 \times 5\text{mm}^3$. Tissue percentages were estimated by calculating the ratio of INSECT tissue-classified voxels (1mm^3) for a given tissue type (WM, GM, CSF) that were located inside the corresponding low-resolution voxels ($2 \times 2 \times 5\text{mm}^3$), for which the quantitative maps (B_1, T_1) were acquired.

3.4.2 B_1 Mapping

Three rapid B_1 mapping techniques (Bloch-Siegert shift, BS; actual flip angle imaging, AFI; echo planar imaging double angle, EPI-DA) were acquired with acquisition protocols that matched their original publications values as closely as possible. A single-slice double angle B_1 map was acquired as a reference (Ref. DA), as is typical [93,173]. Lastly, a uniform B_1 map of value 1 normalized units (n.u.), noted in short-hand as “Nominal,” was generated to represent the case when VFA T_1 values are fitted using the nominal flip angles of its acquisition protocol.

BLOCH-SIEGERT (BS). Single-slice BS B_1 maps [93] were acquired using an in-house-developed pulse sequence: TE/TR = 15/100 msec, excitation flip angle (α) = 25°, field-of-view (FOV) = 25.6 × 17.6 cm², 2 × 2 mm² in-plane resolution, 128 × 88 matrix (readout/phase), 5 mm slice thickness, 1 slice, 8 msec Fermi Pulse of 500° at 64 kHz off-resonance and phase-shift constant $K_{BS} = 74.01$ rad/G², 19 sec scan time.

ACTUAL FLIP ANGLE IMAGING (AFI). AFI B_1 maps were acquired using an in-house-written slab-selective 3D AFI pulse sequence with optimal RF and gradient spoiling [92,95]: TE/TR1/TR2 3.53/20/100 msec, $\alpha = 60^\circ$, BW = 260 Hz/pixel, FOV = 25.6 × 17.6 × 16.0 cm³, 2 × 2 × 5 mm³ resolution, 128 × 88 × 32 matrix (readout/phase/3D), spoiling gradient moment (A_G) = 450 mT·ms/m and RF phase increment (ψ) = 39°, 5 min 38 sec scan time.

EPI DOUBLE ANGLE (EPI-DA). Interleaved multislice spin-echo EPI-DA B_1 maps with whole-brain coverage were acquired using a standard product EPI pulse sequence with a protocol similar to that of Wang et al [89], except with 180° refocusing pulses (the scanner default for this sequence). Since our sequence used (α , 180°) and (2 α , 180°) excitation-refocusing pulses, instead of (α , 2 α) and (2 α , 4 α) in the original article, the equation used to calculate EPI-DA B_1 was [87,90]:

$$B_1 \equiv \frac{\alpha_{corr}}{\alpha} = \frac{\cos^{-1}\left(\frac{I_2}{2I_1}\right)}{\alpha} \quad (3-1)$$

where α is the nominal flip angle (double for the second measurement), α_{corr} is the true flip angle experienced by the tissue at that voxel location, I_1 and I_2 are the image voxels magnitudes for α and 2α acquisition, respectively. The EPI-DA acquisition protocol was: TE/TR = 46/4000 msec, $\alpha/2\alpha = 60^\circ/120^\circ$, FOV = 25.6×25.6 cm 2 , 2×2 mm 2 in-plane resolution, 128×128 matrix (readout/phase), 5mm slice thickness, 27 slices, EPI factor = 9 (15 shots of 9 k-space readout line acquisitions), echo spacing = 4.18 msec, fat saturation on, BW = 250 Hz/px, 2 min 16 sec scan time. Standard automated shimming was performed as with all other sequences (shim currents adjusted using a 3D phase map); no additional adjustments of the static or gradient fields were necessary.

Fast EPI sequences, such as the widely used single-shot implementations, can be susceptible to a wide range of artifacts that lead to a degradation of image quality. Several strategies are incorporated in this protocol to mitigate these artifacts, while still using a readily available scanner sequence and maintaining rapid overall acquisition. A segmented multishot EPI approach increases the effective BW in the phase-encode direction, which reduces distortion artifacts that are typically prevalent in areas of high B_0 inhomogeneity such as near the sinuses. Blurring is also reduced, due to decreased T_2^* modulation in each acquired echo train. Acquiring the B_1 map at a low in-plane resolution (2×2 mm 2) also means smaller readout gradient amplitudes are used, reducing potential eddy current artifacts (e.g. ghosting). Other fast imaging techniques, such as fast spin-echo, have also been adapted for whole-brain double angle B_1 mapping [90]. These methods could offer different imaging benefits as alternatives to EPI; however, such a comparison is outside the scope of the present work.

REFERENCE DOUBLE ANGLE (REF. DA). Single-slice double angle B_1 maps were acquired using a spin-echo sequence as a reference measurement for the other B_1 mapping techniques: TE/TR 12/1550 msec, $\alpha = 60^\circ/120^\circ$, FOV = $25.6 \times 17.6 \text{ cm}^2$, $2 \times 2\text{mm}^2$ in-plane resolution, 128×88 matrix (readout/phase), 5mm slice thickness, 1 slice, slice-selective excitation and 180° refocusing pulses, and BW = 130 Hz/pixel, 4 min 28 sec scan time. The flip angles were chosen to match the EPI-DA sequence. As Ref. DA is the most time costly of all the compared methods (4 min 38 sec), a shorter TR was chosen to reduce the acquisition time of the entire protocol while maintaining sufficient accuracy in WM [56]. The TR is sufficiently long to allow almost complete relaxation of the WM signal, which we are evaluating.

Overall, each pulse sequence had the following effective acquisition time per slice: Ref. DA: 4 min 38 sec/slice, BS: 19 sec/ slice, AFI: 11 sec/slice (3D measurement), EPI-DA: 5 sec/slice (interleaved multislice sequence produced 27 slices in 68 sec per flip angle acquisition).

3.4.3 T_1 Mapping

VFA is a widely used T_1 mapping technique; spoiled gradient echo images are acquired using multiple (usually 2–5) excitation flip angles, each using the same TR. VFA T_1 maps were acquired using a standard product spoiled 3D gradient echo pulse sequence: $2 \times 2 \times 5\text{mm}^3$ resolution, $128 \times 88 \times 32$ matrix (readout/phase/3D), TE/TR 2.89/15 msec, $\alpha = 3^\circ/20^\circ$, BW = 390 Hz/pixel, default manufacturer slab-selection and RF spoiling modes, 1 min 28 sec scan time.

3.4.4 Data Analysis

B_1 and T_1 maps were processed from the MRI data using custom MATLAB code (MathWorks, Natick, MA). Each B_1 map was used to scale the VFA nominal flip angles voxelwise prior to fitting for T_1 . T_1 maps were estimated from linear least square fitting to the SPGR equation [56].

The B_1 amplitude is expected to be a smooth slowly varying function, particularly in the brain [170]. As such, B_1 maps are commonly filtered to reduce noise and minor artifacts [92,173]. Subjective assessment of the images was performed by two of the coauthors (coauthors #3 and #6) who were blinded to the acquisition method used for each dataset. They provided a brief subjective evaluation of any artifacts they observed. A consensus opinion was then formed via discussion between all coauthors. In addition to comparing unfiltered (raw) B_1 maps (as well as in the VFA T_1 analysis), we repeated the data analysis using filtered B_1 maps. Single-slice B_1 maps were filtered (prior to WM masking) using the MATLAB function *roifilt2* and skull-stripped brain masks (all tissues). A Gaussian kernel (*fspecial*) was used with a full-width-half-maximum of $10 \times 10\text{mm}^2$ (sigma = 4.2466) and a 7×7 voxel kernel matrix.

The voxelwise WM B_1 and T_1 data for each method (Ref. DA, BS, AFI, EPI-DA) and the nominal flip angle case (Nominal) were pooled together (all subjects) for data analysis. Histograms of the unfiltered B_1 maps and accompanying fitted T_1 values were calculated to investigate the presence of potential systemic biases or spreading between methods [56,90]. Linear regression analysis of B_1 and T_1 (Pearson correlation and linear fit values) was performed for each B_1 method relative to the Ref. DA B_1 values. The linear regression analysis was performed using both the unfiltered and the Gaussian filtered B_1 data.

3.5 Results

Pooled-subject histograms of unfiltered B_1 map values from WM regions are shown in Figure 3-2a. There is an overlap between the different B_1 histograms; the differences in statistical modes (ΔMode) for each method relative to Ref. DA were 3.6/1.5/3.8% (BS/AFI/EPI-DA). EPI-DA is the only method for which a small B_1 histogram shift is qualitatively observable, which suggests

the presence of a small systemic bias. The unfiltered B_1 maps for a single subject are shown in Figure 3-3b, along with their accompanying acquisition images in Figure 3-3a. The signal-to-noise ratio (SNR) in a region-of-interest of WM was estimated across all subjects to be 240 ± 45 for Ref. DA, 98 ± 11 for BS, 170 ± 35 for AFI, and 130 ± 30 for EPI-DA. Linear regression statistics computed using the pooled voxelwise data for each unfiltered B_1 map (BS, AFI, EPI-DA) relative to the Ref. DA measurement is presented in Table 3-1. EPI-DA had the highest Pearson correlation coefficient relative to Ref. DA ($\rho = 0.96$) and a near-unity slope ($\beta = 0.99$); the BS B_1 maps had the lowest correlation out of the three ($\rho = 0.88$). Table 3-2 lists the mean and SD of voxelwise differences (%) in WM for each B_1 method relative to Ref. DA. Overall, EPI-DA had a lower voxelwise percent differences SD than other methods for all subjects, except subject #6, where BS had a lower value.

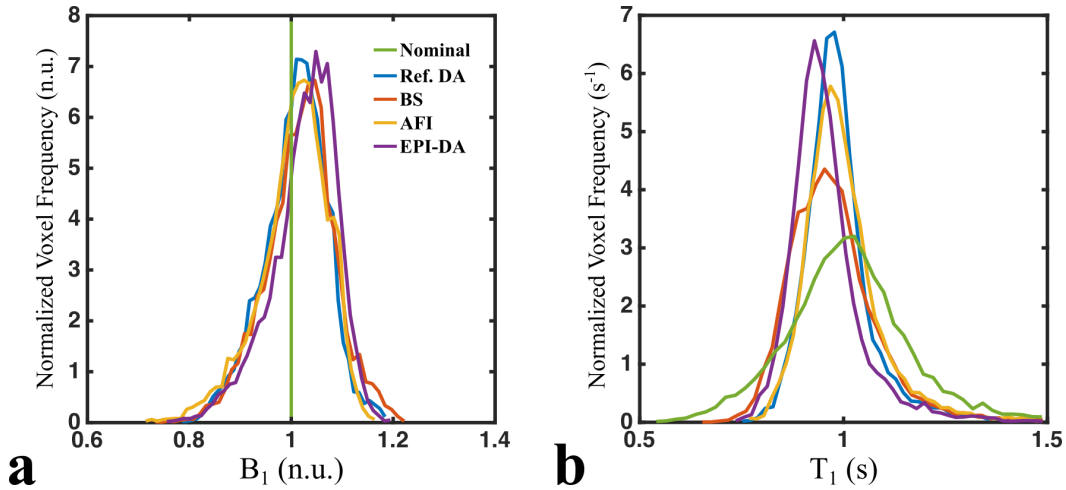


Figure 3-2. Normalized histograms of single-slice unfiltered B_1 (a) and T_1 (b) map values masked for WM in six healthy subjects. The abbreviation “n.u.” stands for normalized units.

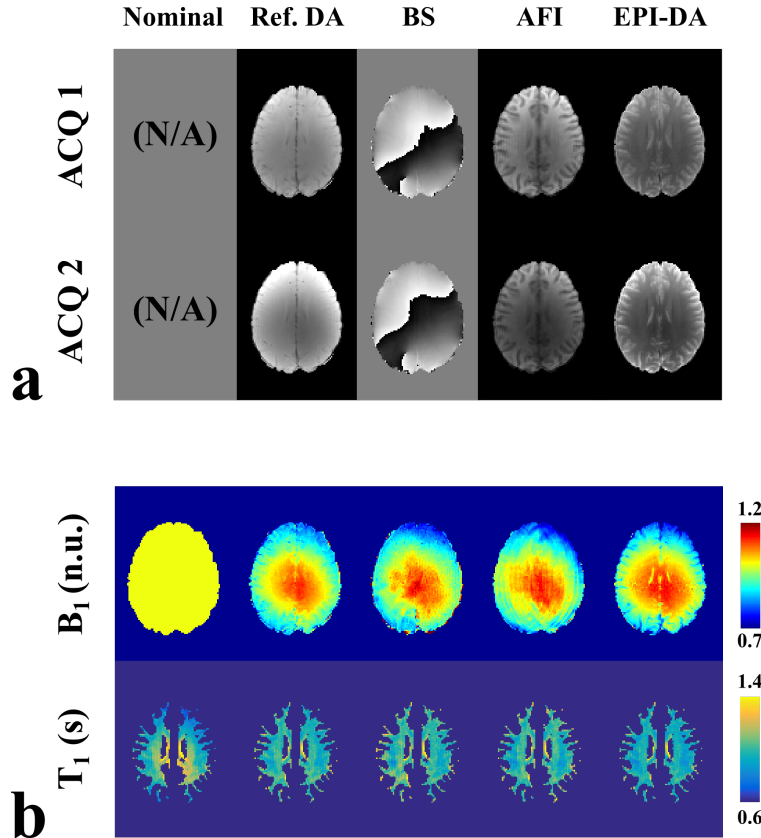


Figure 3-3. a: Acquisition images for each acquired B_1 method: Ref. DA (reference single-slice double angle), AFI (actual flip angle imaging), BS (Bloch-Siegert shift), and EPI-DA (double angle using an interleaved multislice EPI acquisition). b: Unfiltered single-slice B_1 maps, and corresponding WM-masked VFA T_1 maps fitted using flip-angles scaled voxelwise using each B_1 map. The “Nominal” column represents VFA T_1 fitting using no B_1 correction ($B_1 = 1$ n.u.).

The pooled-subject histogram analysis of WM T₁ values is shown in Figure 3-2b. Each measured B₁ map resulted in narrower WM T₁ histograms than for the Nominal case. The differences in statistical modes (ΔMode) for WM T₁ between Ref. DA and BS/AFI/EPI-DA/Nominal were 2.5/1.0/5.0/5.0%, respectively. The width of the WM T₁ distributions had more relative variation between methods than observed for the B₁ histograms. EPI-DA had the largest ΔMode value (5%), but did not experience noticeable broadening relative to Ref. DA. However, BS clearly did suffer from broadening, yet much less severe than the Nominal case. The small reduction in EPI-DA WM T₁ histogram statistical mode (Figure 3-2b) is attributed to the small increase in the corresponding B₁ histogram statistical mode (Figure 3-2a). T₁ correlations were lower relative to their respective B₁ correlations, which was to be expected due to the B₁-sensitivity of the VFA technique. Overall, EPI-DA T₁ maps had the highest correlation relative to Ref. DA ($\rho = 0.92$), which was substantially better than for the Nominal case ($\rho = 0.53$). WM-masked T₁ maps are shown for a single subject in Figure 3-3. Large overestimations of T₁ at the center of the slice are clearly seen for the Nominal case, unlike those using each measured B₁ map.

Table 3-1. Linear regression analysis of the pooled WM-masked B₁ and T₁ values (six subjects) for each rapid B₁ method relative to the Ref. DA method.

			Unfiltered B ₁ Maps			Gaussian Filtered B ₁ Maps			
		Ref. DA	Nominal	BS	AFI	EPI-DA	BS	AFI	EPI-DA
B₁	Pearson ρ	-----	N/A	0.88	0.92	0.96	0.92	0.95	0.98
	Slope β	-----	N/A	0.97	1.01	0.99	0.96	0.99	1.01
	Intercept y_0	-----	N/A	0.04	-0.01	0.03	0.05	0.00	0.01
T₁	Pearson ρ	-----	0.53	0.79	0.81	0.92	0.86	0.88	0.96
	Slope β	-----	0.95	0.99	0.89	0.94	0.97	0.92	0.98
	Intercept y_0	-----	0.07	0.00	0.12	0.02	0.00	0.09	-0.02

Table 3-2. Mean and standard deviations of voxelwise percent differences (%) of B_1 and T_1 values in WM relative to the Ref. DA method for all subjects.

Mean \pm SD Voxel-wise Percent Differences (%) in White Matter						
	Subject #	Ref. DA	Nominal	BS	AFI	EPI-DA
B_1	1	-----	N/A	0.31 ± 3.47	0.47 ± 1.83	1.67 ± 1.43
	2	-----	N/A	3.34 ± 2.46	-1.46 ± 2.40	2.41 ± 1.32
	3	-----	N/A	0.95 ± 2.24	-0.44 ± 2.22	1.87 ± 1.49
	4	-----	N/A	1.57 ± 2.43	-1.28 ± 3.12	0.15 ± 1.66
	5	-----	N/A	-0.01 ± 3.61	0.63 ± 2.09	2.37 ± 1.45
	6	-----	N/A	2.07 ± -0.69	-0.69 ± 3.07	1.76 ± 2.08
T_1	1	-----	-2.11 ± 12.12	-0.30 ± 6.83	-0.85 ± 3.78	-3.27 ± 2.70
	2	-----	2.86 ± 10.96	-6.25 ± 4.67	3.17 ± 5.07	-4.64 ± 2.50
	3	-----	0.46 ± 10.64	2.10 ± 4.69	1.03 ± 4.66	-3.72 ± 2.59
	4	-----	10.27 ± 14.19	-3.01 ± 4.84	2.69 ± 6.60	-0.54 ± 2.60
	5	-----	3.40 ± 11.01	0.32 ± 7.02	-1.09 ± 4.16	-4.53 ± 2.72
	6	-----	-2.70 ± 10.54	-3.86 ± 4.93	1.56 ± 6.70	-3.39 ± 4.36

Artifacts in the unfiltered B_1 maps differ between methods due to their differing acquisition pulse sequences (Figure 3-3b). The sulci are visible in the B_1 maps of both DA methods (Ref. DA and EPI-DA), unlike BS and AFI. In the ventricles, lower B_1 values are present for Ref. DA and EPI-DA relative to the other methods (Figure 3-3b, Figure 3-5). An open-ended fringe line (pole) was present in the Bloch-Siegert phase maps (Figure 3-3a), due to out-of-phase multichannel image recombination [174], and may have caused some inhomogeneity in the Bloch-Siegert B_1 maps in the posterior left hemisphere (Figure 3-3b). This phase image artifact was present in all subjects. For BS, the inhomogeneities near the phase pole along with noisier B_1 maps were likely contributing factors in the broadening of the WM T_1 distribution (Figure 3-2b). A ringing artifact affected the AFI B_1 maps (Figure 3-3b), although it is not easily seen in the raw AFI acquisition images themselves (Figure 3-3a). However, by carefully adjusting the window/level (not shown),

a small ringing artifact is present in both AFI MRI images. We observed this ringing in both the raw data and B_1 maps of all subjects. If the ringing between both images is out-of-phase, the resulting B_1 artifact may be amplified due to the nature of the AFI calculation, which requires a division of the two images. The original AFI work only presents their B_1 maps postfiltering ($8 \times 8 \times 16\text{mm}^3$ median filter); however, ringing can also be seen in their axial and coronal TR1 images (fig. 10a in Ref. [92]). Overall, these artifacts and noise in the unfiltered B_1 maps likely contributed to lower correlations of B_1 and T_1 relative to the reference maps.

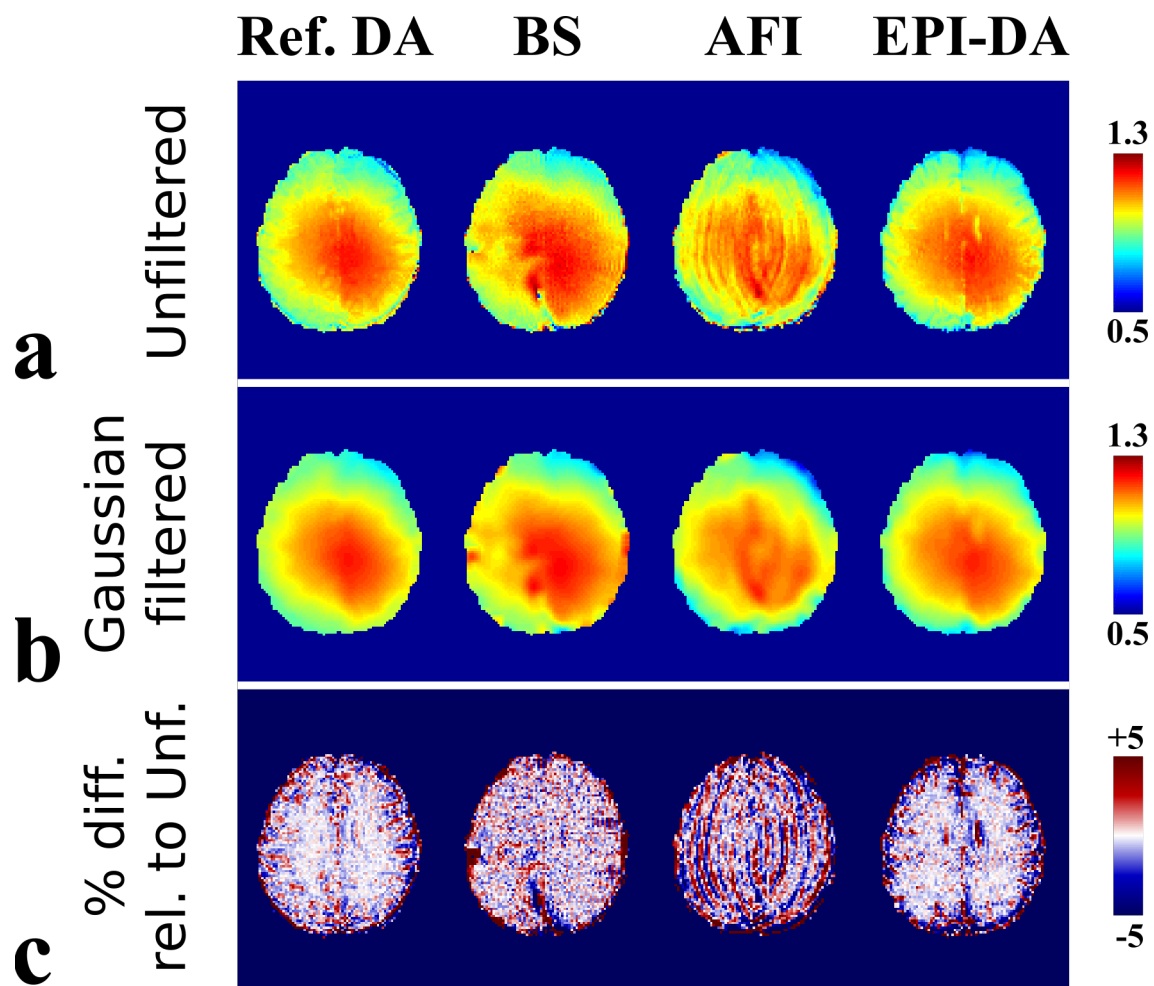


Figure 3-4. Unfiltered (a) and Gaussian filtered (b) B_1 maps of a single subject. (c) Relative differences between unfiltered and filtered maps shown as percent difference maps.

The unfiltered and Gaussian filtered B_1 maps are shown for a subject in Figure 3-4a,b, and the relative difference (%) between the two is shown in Figure 3-4c. The Gaussian filter was effective at reducing noise in the maps, as well as in attenuating minor artifacts (e.g. sulci in DA maps, “ringing” in AFI). The correlations and linear regression analysis of B_1 (and VFA T_1) relative to the reference (Ref. DA) were recalculated using the filtered B_1 maps (Table 3-1). The correlations improved postfiltering; for BS/AFI/EPI-DA, B_1 correlations (ρ) were 0.92/0.95/0.98, and for T_1 they were 0.86/0.88/0.96. The 95th percentiles of the absolute relative differences between the reference B_1 map and BS/AFI/EPI-DA (in WM) were equal or lower than 5% (5/4/3%, respectively), while the nominal flip-angle case had a relative difference (to Ref. DA) 95th percentile of 13%.

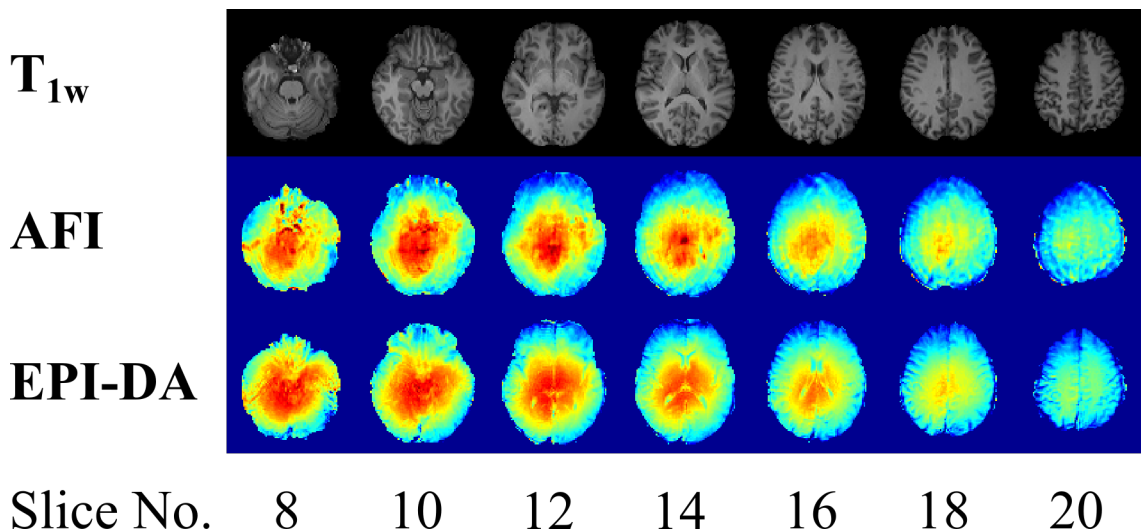


Figure 3-5. Whole-brain coverage of axial MP-RAGE T_{1w} slices, unfiltered AFI B_1 maps, and unfiltered EPI-DA B_1 maps in one subject.

The raw images used to calculate an EPI-DA B_1 map for a subject are shown in Figure 3-3a. The image quality of the EPI images is comparable to the Ref. DA method, and no observable distortions or ghosting were present in the brain for either the acquisition images or the B_1 map. This observation was consistent in all subjects for the slice used in the data analysis. In addition to

the single-slice measurements, two of the B_1 mapping protocols were acquired with whole-brain coverage (AFI and EPI-DA). Axial slices for both B_1 methods are shown in Figure 3-5. EPI-DA B_1 maps throughout the brain were free of severe susceptibility-induced distortions. However, the ventricles can be clearly identified in the EPI-DA maps (lower values) unlike for AFI, as AFI is well known to be very robust for a wide range of T_1 values [92].

3.6 Discussion

Our findings demonstrate that B_1 mapping implemented using a standard product EPI pulse sequence (EPI-DA) can provide quality whole-brain B_1 maps with a short acquisition time ($\sim 2\text{min}$). The B_1 maps were comparable or superior in WM to other well-regarded rapid acquisition B_1 methods (AFI and BS) at 3T. Unfiltered B_1 maps correlated with our reference single-slice measurement (Ref. DA), and we observed an improvement in those correlations after applying a Gaussian filter to the images to reduce noise and attenuate small artifacts. Pooled-subject voxelwise B_1 correlation values (relative to Ref. DA) ranged between $0.88 \leq \rho \leq 0.96$ for unfiltered maps, and $0.92 \leq \rho \leq 0.98$ for filtered maps. The 95th percentile of the relative errors of filtered B_1 maps (compared to Ref. DA) were $\leq 5\%$, nearly three times lower than for the nominal flip-angle case (13%). VFA T_1 maps using Gaussian filtered B_1 maps correlated with those using Ref. DA ($0.88 \leq \rho \leq 0.96$), unlike for the case using uncorrected (nominal) flip-angles ($\rho = 0.53$). The peak of the WM T_1 histograms varied slightly between methods (1 to 5%), much less than the differences reported between different T_1 [56] mapping techniques themselves (20–30%). Our results demonstrate that double angle B_1 mapping using a standard product EPI sequences can produce whole-brain B_1 maps comparable in quality to rapid techniques (e.g. AFI and BS) in a clinically acceptable scan time ($\sim 2\text{min}$). While our work was based on a multishot EPI protocol [89], double angle imaging using other fast k-space acquisition strategies could also be considered

(e.g. double angle using a fast spin-echo readout [90]). Implementing standard product pulse sequence protocols for B_1 mapping avoids time-consuming on-site pulse sequence programming (sequences similar to the one used in our study are commonly offered by other manufacturers [89]), improves accessibility of whole-brain B_1 mapping to researchers without access to custom pulse sequences, and could facilitate protocol standardization between sites.

Other groups have also presented comparison studies of existing B_1 methods. Lutti et al [173] optimized and compared the following methods at 3.0T: AFI, a 3D stimulated-echo B_1 mapping method with EPI readouts, a 2D stimulated echo acquisition mode (STEAM) B_1 mapping method, and single-slice DA as a reference. The two stimulated-echo-based methods required additional quantitative pulse sequences for calibration: the 3D stimulated-echo with single-shot EPI B_1 mapping technique used B_0 maps to correct for distortions, and the 2D STEAM method was calibrated against AFI using a separate measurement on a gel phantom to correct for nonlinearities of the slice-selective pulse. Each method demonstrated good reproducibility, and the largest deviation relative to the reference (DA) was observed with the stimulated-echo EPI method (4%), which is in the range of deviation we observed with our standard product EPI-DA pulse sequence (5% relative to Ref. DA for WM). Despite the benefits of these optimized rapid B_1 methods, wide-scale use is limited, as all methods require pulse sequence programming expertise and additional quantitative measurements. Another important source of B_1 inaccuracies, noise, has been characterized for different B_1 methods (Ref. DA, AFI, and BS) using Monte Carlo simulations and phantoms [175,176]. The authors demonstrated that SNRs as low as 50 can be sufficient for accurate flip angle estimation for the range observed in the brain at 3T, and all of the methods compared in our work had SNRs above this threshold in WM.

Optimal flip angles for VFA are in the low FA range (1–30°) due to short TRs required for whole-brain VFA T_1 mapping.²¹ All B_1 methods compared in this work used larger flip angles to map the B_1 intensity (Ref. DA and EPIDA: 60°/120°; AFI: 60°; BS: 25° and 500°), consistent with the published values in the original articles. Thus, RF amplifier nonlinearities could result in inaccurate low FA estimations. RF amplifier nonlinearity can vary substantially between scanner hardware manufacturers, which may lead to a bias of the corrected low flip angles used for VFA [177]. VFA pulse sequence optimization techniques have been proposed to minimize the impact of RF nonlinearity on T_1 mapping [178]. A modified DA B_1 method has also been proposed to map low flip angles accurately [177], which could possibly be adapted to use fast k-space readout acquisition pulse sequences, such as EPI or fast spin-echo.

For the purpose of our study, a simple single-slice DA method measurement was considered to be our “reference” method, as is often the case in B_1 mapping studies. The Ref. DA acquisition is itself sensitive to sources of inaccuracies, as the typical pulse sequence protocols for Ref. DA render the B_1 maps sensitive to long T_1 , particularly in voxels containing CSF. The TR used for this pulse sequence was shorter than conventional implementations; however, it was validated against another robust DA method [91] using a TR = 3000 msec and demonstrated very high voxelwise correlation in WM ($\rho = 0.98$, $y = 0.99x + 0.03$). Longer TRs could be used for improved accuracy; however, such a protocol requires 20+ min for a single slice scan [93], and motion would become an increasing concern with longer TRs. Slice-select RF pulse profiles may also impact B_1 map accuracy, as nonrectangular RF profiles result in a range of flip angles within a slice (and voxel), particularly for large flip angles. Some techniques have been developed to correct for slice profile effects [179]; however, they add additional complexity in postprocessing and require RF pulse waveform information, which may not always be accessible from the scanner. Single-slice

DA imaging can mitigate slice profile inaccuracies by using nonselective excitation pulses [91] or refocusing pulses, yet undesired signal from outside the slice can be a problem if incompletely crushed [180]. All B_1 methods compared in this work used pulse sequences that differ greatly in their mechanism and analysis (saturation recovery: DA; steady-state: AFI; phase: BS), yet still produced voxelwise B_1 values highly correlated with the reference measurement (Ref. DA). Each B_1 method, even considering their imperfections, produced much better T_1 maps than for the case of omitting B_1 correction altogether (Nominal).

Smoothing or blurring filters are typically applied to B_1 maps [92,173,181], as the B_1 variation in the brain is expected to be smooth and spatially slowly varying [170]. There is no well-established consensus on which filter is ideal for B_1 maps. The types of filters used in the literature are numerous: Gaussian convolution, median filters, spline interpolation, etc. In addition, the size of the blurring kernel used varies widely between studies; ranging from 3mm [92] to 10 mm [181]. Although filtering the B_1 map is often considered a good practice when used in subsequent B_1 -correction applications, unfiltered B_1 maps should also be reported when using, developing, or comparing new B_1 methods. B_1 methods are often only compared postblurring [92,173], thus not all artifacts (or noise level) may be clearly identifiable, only those not fully attenuated by the filters. Unfiltered B_1 maps display valuable information about scanner and pulse sequence artifacts, which is particularly useful when developing or evaluating new methods. For example, even though the ringing artifact in our AFI measurements can be attenuated in the B_1 maps using filtering methods, it may be preferable to use preprocessing techniques to eliminate the ringing in the acquisition images before the B_1 map is calculated [182]. Although blurring B_1 maps can attenuate local artifacts, it can also spread inaccuracies (e.g. ventricles in our EPI-DA maps). If tissue masks are available, specific tissues known to produce inaccurate B_1 values (e.g. for the multislice EPI-DA

case, cerebrospinal fluid) could be masked, and B_1 values could be interpolated in these regions to approximate the missing values.

The specific scope of this work is limited to applications at clinical field strengths. B_1 mapping at ultrahigh field strengths must be robust against more B_0 inhomogeneity, longer T_1 values, and faces additional hardware challenges, such as parallel transmit [183]. Accelerating B_1 mapping methods using an EPI-based acquisition scheme can be prone to significant susceptibility distortions and signal dropouts at ultrahigh fields [96]. However, Bloch-Siegert at 7T requires additional acceleration techniques like EPI due to its high SAR RF pulses [184]. Supplementary scans (e.g. B_0 map) can be used in EPI-based B_1 mapping to correct the distortions [185], but at the cost of a longer total scan time. Investigating structural characteristics of the cortex is also a topic of great interest in high-field MRI, due to its capability to image at very high resolutions ($\leq 1\text{mm}^3$). High-resolution VFA T_1 mapping of the cortex must use B_1 maps acquired using a method that has a good robustness against the long T_1 of CSF that neighbors the cortical regions [186], such as AFI, BS, or other advanced B_1 mapping techniques.

This study had some limitations. The decision to use single-slice B_1 for a reference limited the quantitative comparison between methods to a single slice of the brain. Although using a single-slice DA B_1 map as a reference is common for validating whole-brain methods [93,173], one solution could be to acquire two more slices in perpendicular planes. Another limitation was that the low resolution of the reference scan restricted the quantitative assessment of B_1 and T_1 values to WM. To quantitatively compare B_1 maps in the cortex, a faster reference acquisition allowing for higher resolution ($\sim 1\text{mm}^3$) is needed.

In conclusion, we report that B_1 mapping at 3T implemented using standard product pulse sequences (e.g. interleaved multislice EPI double angle) can serve as a sufficient alternative to advanced B_1 methods (e.g. actual flip angle imaging, Bloch-Siegert), which are not readily available on most MRI systems. The EPI double angle protocol produced whole-brain B_1 maps in a clinically acceptable scan time (~2min), shorter than the AFI and BS's protocols that were compared (although these methods can be further accelerated by implementing fast acquisition strategies, e.g. EPI, fast spin-echo, or spiral). All investigated B_1 mapping methods correlated well with a reference measurement, and produced substantially better VFA T_1 maps than in the absence of B_1 correction. The agreement between B_1 maps and resulting T_1 maps were improved by filtering the B_1 maps to reduce noise and minor artifacts. B_1 mapping implemented with standard product pulse sequences can provide an excellent alternative for researchers without custom rapid whole-brain B_1 methods and is much preferred to omitting B_1 correction altogether.

3.7 Acknowledgments

Contract grant sponsor: National Sciences and Engineering Research Council of Canada with the Alexander Graham Bell Canada Graduate Scholarships-Doctoral program (to M.B.); Contract grant sponsor: CIHR and Campus Alberta Innovates grants (to G.B.P.)

Chapter 4

B₁-Sensitivity Analysis of Quantitative Magnetization Transfer Imaging

4.1 Preface

Chapter 3 demonstrated that acquiring good quality whole-brain B₁ maps is feasible using a standard MRI pulse sequence, which is valuable to researchers unable to implement advanced pulse sequences such as AFI and Bloch-Siegert. In addition, that chapter presented several potential sources of inaccuracies in B₁ maps (e.g. noise, artifacts, filtering) and compared VFA T₁ maps in the presence of all of these imperfections, as well as for the complete omission of a B₁ map. Because conventional qMT using an SPGR pulse sequence requires both a B₁ and a T₁ map, inaccuracies in B₁ values will propagate to the qMT fitting parameters differently depending on if the T₁ mapping method used is B₁-independent (e.g. Inversion Recovery) or B₁-dependent (e.g. VFA). For the B₁-independent T₁ case (e.g. IR), errors in B₁ value will propagate to qMT fitting parameters through the calibration of the nominal MT pulse and excitation flip angles; for the B₁-dependent T₁ case (e.g. VFA), errors in B₁ value will propagate to qMT through this same pathway, but also through errors in T_{1,obs} (used as a constraint for qMT parameters). The purpose of this chapter is to examine the B₁-sensitivity of qMT for these two categories of T₁ mapping techniques, and to determine which T₁ mapping method results in the least B₁-sensitivity of the qMT parameters, particularly for the pool-size ratio (F).

The following manuscript, published in the journal *Magnetic Resonance in Medicine*, describes a B₁-sensitivity analysis of qMT, considering IR and VFA T₁ mapping. The impact on fitted qMT parameters (F, k_f, T_{2,f}, T_{2,r}) due to errors in B₁ were first explored using simulations. A sensitivity

analysis of the qMT Z-spectrums using simulated values was performed to investigate the origin of the differences in sensitivity characteristics between T_1 mapping methods. *In vivo* measurements on healthy adult subjects were performed to study the sensitivity of the pool-size ratio for a wide-range of B_1 errors by analyzing the values in the absence of any B_1 correction; qMT values were also compared using B_1 maps originating from three different B_1 mapping techniques (DA, BS, AFI). Overall, this manuscript establishes the characteristics of the B_1 -sensitivity for a qMT acquisition protocol, informs qMT researchers of the substantial differences in B_1 -sensitivity of the fitted parameters that occurs depending on which T_1 mapping technique is used, and discovers that under the right circumstances (e.g. VFA) it may be possible for the pool-size ratio to be robustly estimated using qMT even if a B_1 map is completely omitted.

B₁-Sensitivity Analysis of Quantitative Magnetization Transfer Imaging

Mathieu Boudreau, Nikola Stikov, G. Bruce Pike

McConnell Brain Imaging Centre, Montreal Neurological Institute
3801 University Street, McGill University
Quebec, Canada, H3A 2B4

Magnetic Resonance in Medicine, 79: 276-285 (2018)

4.2 Abstract

Purpose: To evaluate the sensitivity of quantitative magnetization transfer (qMT) fitted parameters to B_1 inaccuracies, focusing on the difference between two categories of T_1 mapping techniques: B_1 -independent and B_1 -dependent.

Methods: The B_1 -sensitivity of qMT was investigated and compared using two T_1 measurement methods: inversion recovery (IR) (B_1 -independent) and variable flip angle (VFA), B_1 -dependent). The study was separated into four stages: 1) numerical simulations, 2) sensitivity analysis of the Z-spectra, 3) healthy subjects at 3T, and 4) comparison using three different B_1 imaging techniques.

Results: For typical B_1 variations in the brain at 3T ($\pm 30\%$), the simulations resulted in errors of the pool-size ratio (F) ranging from -3% to 7% for VFA, and -40% to >100% for IR, agreeing with the Z-spectra sensitivity analysis. In healthy subjects, pooled whole-brain Pearson correlation coefficients for F (comparing measured double angle and nominal flip angle B_1 maps) were $\rho = 0.97/0.81$ for VFA/IR.

Conclusion: This work describes the B_1 -sensitivity characteristics of qMT, demonstrating that it varies substantially on the B_1 -dependency of the T_1 mapping method. Particularly, the pool-size ratio is more robust against B_1 inaccuracies if VFA T_1 mapping is used, so much so that B_1 mapping could be omitted without substantially biasing F .

4.3 Introduction

Quantitative magnetization transfer (qMT) imaging is a powerful MRI technique used to investigate macromolecular content not typically detectable with conventional MRI. MR

properties of macromolecular hydrogen are measured with qMT by indirect means: the magnetization of the macromolecular pool is saturated, and energy is exchanged with nearby water molecules via cross-relaxation processes and chemical exchange [105,143]. In imaging brain white matter (WM), the pool-size ratio (F), the ratio between the equilibrium magnetization of hydrogen in macromolecules versus hydrogen in water, has been shown to be a good marker of myelin density [42,187]. In particular, the pool-size ratio has been used to study multiple sclerosis lesions [154,188,189]. Several methods have been developed to estimate qMT parameters from the mathematical model that describes the exchange processes [144,150,151,190,191].

Commonly, off-resonance qMT imaging uses a magnetization transfer (MT)-prepared spoiled gradient (SPGR) echo pulse sequence [192]. It is a standard SPGR sequence preceded by an off-resonance radiofrequency (RF) pulse that varies in amplitude and frequency offset between measurements; 10 measurements or more are generally required to fit this Z-spectrum (normalized MT signal vs. off-resonance frequencies) [165], and one additional measurement without the MT-preparation for signal normalization. These qMT techniques also require three additional measurements: B_0 , B_1 , and T_1 . In postprocessing, B_0 maps calibrate the off-resonance frequency of the MT pulse in each voxel. B_1 maps are used to scale the SPGR excitation flip angle and MT-pulse saturation power. A T_1 map is necessary to constrain certain fitting parameters of the two-pool MT fitting model [143]. For a given voxel, the measured T_1 ($T_{1,\text{meas}}$) is a function of the T_1 of the water molecules ($T_{1,f}$, “f” is for “free pool”) and of the T_1 of the macromolecules ($T_{1,r}$, “r” is for “restricted pool”), and two other parameters (F , ratio of the two pool sizes in the voxel, and k_f , the exchange rate constant). The large number of measurements required to sample the Z-spectrum and additional quantitative maps make qMT a time-costly technique.

Increasingly, whole-brain qMT imaging has been achieved via a reduction in qMT measurements [168,193] and new rapid techniques to measure the required quantitative calibration maps [92,93,95]. However, integrating new methods into quantitative imaging studies can introduce unintended effects. For example, transitioning from single-slice T_1 mapping techniques (i.e., inversion recovery [IR]) to three-dimensional [3D] techniques, variable flip angle [VFA]) also results in transitioning from B_1 -insensitive [55,56] to B_1 -sensitive [64] T_1 mapping. If VFA is used in the qMT imaging protocol, inaccuracies in B_1 will propagate into fitted qMT parameters through two pathways instead of just one (Figure 4-1): from errors induced in T_1 , used to restrict the fitting parameters, and from errors in scaling the MT saturation powers with the B_1 maps. The potential effect of B_1 -uncorrected qMT on the fitted parameters has been noted in previous work [145,194]; however, these were limited in scope to B_1 -insensitive T_1 techniques. To our knowledge, no comprehensive characterization of the B_1 - sensitivity of qMT (and notably, comparing different T_1 mapping methods) has previously been performed.

This work focuses on answering the following three questions: 1) How sensitive is each qMT parameter to B_1 -inaccuracies?; 2) How does the B_1 -sensitivity of qMT parameters differ between protocols using B_1 -independent (IR) and B_1 -dependent (VFA) T_1 mapping methods?; and 3) Which T_1 mapping method results in the most robust measure of the pool-size ratio in the presence of B_1 -inaccuracies? To explore these questions, we first focused on simulations under ideal measurement conditions for a single tissue type, and then used this framework to perform a sensitivity analysis of the signal curves. We then measured qMT maps in healthy human volunteers using both T_1 mapping methods (IR and VFA), and compared measured B_1 maps with fictitious maps generated to have a large range of potential inaccuracies. Finally, we compared the relative

agreement of qMT fits between three different B_1 mapping methods (double angle, actual flip angle imaging, Bloch-Siegert) using both T_1 mapping methods (IR and VFA).

4.4 Methods

All measurements were performed with a 3.0T whole-body MRI scanner (Magnetom TIM TRIO; Siemens, Erlangen, Germany) using a 32-channel phased-array receive-only head coil and whole-body transmit coil. Healthy volunteers were scanned after providing informed consent, in compliance with and approved by the institutional ethics committee. The total scan time for the entire acquisition protocol described in the B_1 -Sensitivity of qMT in Healthy Subjects and B_1 Method Comparison sections was 28 minutes and 58 seconds.

4.4.1 Simulations

The coupled Bloch-McConnell differential equations describing two-pool magnetization exchange were solved numerically (MATLAB 2011a; MathWorks Inc., Natick, MA) for a pulsed MT-prepared SPGR pulse sequence using the Sled and Pike model [145,152]. The pulse sequence was decomposed into event blocks of instantaneous saturation of the free pool, constant irradiation of the restricted pool, and free precession. Prior to simulating exchange, the fractional saturation of the longitudinal magnetization induced by direct saturation was computed numerically in the absence of exchange and T_1 recovery. The steady-state solution was approximated analytically using the assumption that the magnetization at an arbitrary time t should be equal to that of time $t+repetition\ time\ (TR)$, as described in detail in the appendix of Sled and Pike [144]. The signal was simulated with the following pulse sequence parameters [165,193]: $TR = 25\ ms$, excitation flip angle (FA) = 7° , MT pulse flip angle = 142° and 426° , MT pulse duration = $10\ ms$, 10 offresonance frequencies ranging between $423.9\ Hz$ and $17.2354\ kHz$ in logarithmic steps. The

envelope of the MT-preparation RF pulse was a Gaussian-Hanning function, and a super-Lorentzian lineshape function was used for the transition rate of the restricted pool to approximate the behavior observed in tissues [152]. qMT tissue parameters for all simulations were set to healthy white matter values measured in a previous scan: $F = 0.122$ n.u. (normalized units), magnetization exchange rate ($k_f = 3.97 \text{ s}^{-1}$), free-pool longitudinal relaxation rate ($R_{1,f} = 1/T_{1,f} = 1.12 \text{ s}^{-1}$), restricted-pool longitudinal relaxation rate ($R_{1,r} = 1/T_{1,r} = 1.00 \text{ s}^{-1}$), free-pool transverse relaxation time ($T_{2,f} = 27.2 \text{ ms}$), restricted-pool transverse relaxation time ($T_{2,r} = 10.96 \text{ ms}$).

SPGR qMT experiments require three additional quantitative measures: B_0 , B_1 , and T_1 . B_0 measurement methods typically do not require B_1 or T_1 calibration; thus, ideal B_0 homogeneity was used in the simulations. MT signal values were simulated using B_1 (to scale the MT saturation powers and excitation flip angles) and $T_{1,\text{meas}}$ (to constrain the fitting parameters) that were fixed to their ideal values (1 n.u. and 0.9 s respectively). The MT signal was subsequently fitted using the Sled and Pike method [145]. As per convention, $R_{1,r}$ was fixed to 1 s^{-1} . $R_{1,f}$ was calculated during the fitting algorithm from an analytical expression of F , k_f , $R_{1,r}$, and $T_{1,\text{meas}}$. To investigate the effect of inaccuracies in B_1 and $T_{1,\text{meas}}$ on the fitted qMT parameters, the simulated MT signal values were fitted using a large range of B_1 and $T_{1,\text{meas}}$ values. Four qMT parameters (F , k_f , $T_{2,f}$, $T_{2,r}$) were explicitly fitted for each pair of 100 B_1 and 100 $T_{1,\text{meas}}$ values (10,000 combinations). The set of B_1 values varied linearly from 0.5 to 2 n.u., and $T_{1,\text{meas}}$ varied from 0.1 s to 4 s. For this stage, B_1 and $T_{1,\text{meas}}$ varied independently of each other. We investigated the qMT parameter sensitivities due to B_1 inaccuracies for two T_1 mapping techniques: IR, approximately B_1 independent [56], and VFA, inherently B_1 -dependent [64]. The IR case was interpreted to be a linear subset of the B_1 - T_1 combination discussed above by a fixed T_1 ($T_{1,IR} = 0.9 \text{ s}$, constant). The VFA signals from a two flip angle experiment were calculated for $T_1 = T_{1,true} = 0.9 \text{ s}$ from the

analytical steady-state SPGR equation ($\text{TR} = 25$ ms, $\text{FA} = 3^\circ$ and 20°). $T_{1,\text{VFA}}$ values were subsequently estimated by linear least-square fitting of the VFA data with flip angle calibration [61] using the set of 100 B_1 values (0.5 to 2 n.u.). The fitted VFA $T_{1,\text{meas}}$ values were then used in conjunction with their respective B_1 values to fit the qMT parameters to the simulated MT signal.

4.4.2 Sensitivity Analysis

To provide further insight into the behavior of fitted parameters in the presence of B_1 inaccuracy, a sensitivity analysis of the qMT signal was performed [195]. For each qMT parameter, the following definition of sensitivity was used (cf. Section 4.8 – Appendix A):

$$S_{p,i} \equiv \frac{\Delta M_i}{\Delta p}, \quad p = F, k_f, T_{2,f}, T_{2,r}, B_1 \quad (4-1)$$

where the index i describes a specific qMT acquisition point, M_i is the normalized signal of the i th qMT measurement, and $S_{p,i}$ is the sensitivity of the MT signal with respect to p for the i^{th} qMT acquisition. The sensitivity $S_{p,i}$ represents the change in normalized MT signal induced by a slight change in fitting parameter value or model input value (e.g., B_1). A large absolute $S_{p,i}$ value signifies that, to a linear approximation, a large change in MT signal will occur (at that Z-spectrum value) for a small variation of p . In the context of fitting data to measurements using an inaccurate B_1 value, the following relationship can be shown (cf. Section 4.8 – Appendix A):

$$\sum_{p \neq B_1} S_{p,i} \Delta p \cong -S_{B_1,i} \Delta B_1 \quad (4-2)$$

Thus, the sensitivity values can provide an insight as to why certain fitting parameters are more likely to have large errors due to inaccurate B_1 values. When comparing two measurement

protocols, the following metrics can be expected to provide insight into which fitting parameters p are more/less sensitive to B_1 inaccuracies (cf. Section 4.8 – Appendix A):

$$|\hat{S}_p \cdot \hat{S}_{B_1}| \quad (4-3)$$

$$\frac{B_1}{p} \frac{\|\mathbf{S}_{B_1}\|}{\|\mathbf{S}_p\|} \quad (4-4)$$

where \mathbf{S} is the vector of sensitivity values for a set of N measurements, $\|\mathbf{S}\|$ is its norm, and \hat{S} is its unit vector. If the sensitivity values of a parameter p and B_1 have very similar curves (Eq. (4-3) ≈ 1), then p is likely to be most sensitive to B_1 inaccuracies compared to other parameters. The relative error of p will then be proportional to the ratio in Eq. (4-4).

The qMT measurement protocol and tissue parameters from the Simulations section were used to simulate normalized MT signal values. Partial derivatives with respect to qMT parameters (and B_1) of the MT signal were evaluated at each point of the Z-spectrum [196]. B_1 sensitivity values were calculated for two cases: $T_{1,\text{meas}}$ independent of B_1 (which for consistency with the other sections we designate as IR), and $T_{1,\text{meas}}$ with VFA B_1 -dependency. As $T_{1,\text{meas}}$ is primarily used to constrain $R_{1,f}$, $R_{1,f}$ was modified in addition to B_1 accordingly for the VFA case. The derivative steps were fixed to a $10^{-5}\%$ relative increase of the parameter denominator value, sufficient for the convergence of the partial derivative at each Z-spectrum point of our qMT protocol.

4.4.3 B_1 -Sensitivity of qMT in Healthy Subjects

Three healthy adult volunteers were scanned (two males, one female, 30 ± 4 years old). All quantitative imaging sequences were acquired at a resolution of $2 \times 2\text{mm}^2$ in-plane $\times 5\text{mm}$ slice

thickness. Single slices were acquired parallel to the anterior commissure–posterior commissure (AC-PC) line, superior to the corpus callosum.

T₁ Maps: VFA T₁ maps were acquired using a spoiled 3D gradient echo sequence [95]: echo time (TE) = 2.89 ms, TR = 15 ms, FA = 3° and 20 °, spoiler gradient moment (AG) = 280 mT · ms/m, RF phase increment (φ) = 169°, 1 m 28 s scan time. Prior to fitting the data for T₁, the nominal flip angles were scaled voxel-wise with each B₁ map. The VFA T₁ values were then estimated from linear least-square fitting. Inversion recovery T₁ data were collected from a four-inversion-time (TI) spin-echo sequence [56]: TE/TR = 11/1550 ms, TI = 30, 530, 1030, 1530 ms, 9 m 16 s scan time. An open-source software package for robust inversion recovery fitting was used to fit the IR T₁ maps [55].

qMT Maps: qMT data were acquired according to the 10-point MT-prepared SPGR acquisition protocol described in the Simulations methods section, which for our single slice has a 2 m 38 s scan time. B₀ maps were acquired for off-resonance frequency correction using a two-point phase-difference gradient measurement [197]: TE1/TE2/TR = 4/8.48/25 ms, FA = 7°, 30 s scan time. qMT parameter maps were produced by fitting the normalized qMT data voxel-wise using the Sled and Pike fitting model [153].

B₁ Maps: Two categories of B₁ maps were compared: 1) *in vivo* measured B₁ maps and 2) B₁ maps that had a single value assigned to all voxels (B_{1,Flat}). B_{1,Flat} maps were used to investigate the sensitivity of qMT to B₁ inaccuracies for *in vivo* conditions (e.g., noise, tissue partial volume, a broad range of qMT tissue parameter values). Single-slice double angle (DA) B₁ maps (B_{1,DA}) were acquired using a spin-echo readout: TE/TR = 12/1550 ms, FA = 60°/120°, with slice-selective excitation and 180° refocusing pulses, 4 m 28 s scan time. A set of B_{1,Flat} maps were generated for

a range of values ($B_{1,\text{Flat}} = 0.5, 0.75, 0.9, 1, 1.1, 1.25, 1.5, 2$ n.u.), where $B_{1,\text{Flat}} = 1$ n.u. represents the nominal flip angle case. Prior to fitting the qMT data, each B_1 map ($B_{1,\text{DA}}$ and the set of $B_{1,\text{Flat}}$) was used as a corrective factor for the VFA nominal flip angles, MT excitation flip angles, and MT saturation powers.

Data Analysis: qMT parameter maps ($F, k_f, T_{2,f}, T_{2,r}$) were fitted voxelwise using four sets of B_1 and T_1 combinations: $B_{1,\text{DA}}$ and $B_{1,\text{Flat}}$ used with IR and VFA T_1 maps (Figure 4-1). Voxel data of each qMT parameter map were pooled (across all subjects) for each B_1 and T_1 set, and linear regression analysis was performed (comparing $B_{1,\text{DA}}$ and each $B_{1,\text{Flat}}$).

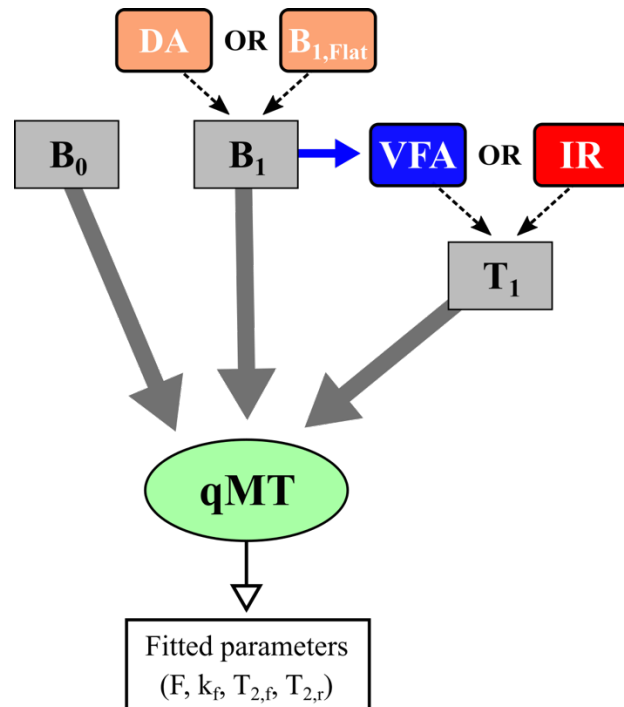


Figure 4-1. Quantitative measurements used in our magnetization transfer (MT)-prepared spoiled gradient quantitative MT study. Solid arrows are used for required measurements; dotted arrows are used for specific methods of a particular measurement. The double angle (DA) method is an explicitly measured B_1 map. $B_{1,\text{Flat}}$ maps are generated using a single value in all voxels. Variable flip angle (VFA) is a T_1 mapping methods that also requires B_1 as a support measurement, unlike inversion recovery (IR).

4.4.4 B_1 Method Comparison

Several techniques exist to measure B_1 maps, and each method can be prone to unique sources of systemic biases or local artifacts [185]. To probe the robustness of the B_1 -sensitivity of qMT between different B_1 measurement techniques, two additional B_1 maps were acquired and compared against the DA B_1 maps in all three subjects from the B_1 -Sensitivity of qMT in Healthy Subjects section. Actual flip angle imaging (AFI) [92], a two-TR steady-state SPGR-based pulse sequence, was applied to produce B_1 maps with a $2 \times 2 \times 5\text{mm}^3$ whole-brain 3D spoiled acquisition (19): $\text{TE/TR1/TR2} = 3.53/20/100\text{ ms}$, $\text{FA} = 60^\circ$, $A_G = 450\text{ mT} \cdot \text{ms/m}$, $\varphi = 39^\circ$, $5\text{ m }38\text{ s scan time}$. Bloch-Siegert shift (BS) B_1 mapping [93], an SPGR-based method with an off-resonance RF preparation pulse, produced B_1 maps using a single-slice $2 \times 2 \times 5\text{mm}^3$ acquisition: $\text{TE/TR} = 15/100\text{ ms}$, $\alpha = 25^\circ$, 8 ms Fermi Pulse of 500° at 64 kHz off-resonance, phase-shift constant (K_{BS}) = 74.01 rad/G^2 , 19 s scan time.

At the resolution of our data ($2 \times 2 \times 5\text{mm}^3$), partial volume effects near cortical grey matter (GM) and adjacent to ventricles can be significant. The partial volume effects can make the analysis of in GM challenging. Preliminary data (not shown) suggested that an insufficient number of voxels exist containing only GM, for a reliable analysis to be performed, and including all voxels containing at least some GM would include a significant bias in the qMT parameters from cerebrospinal fluid (CSF). As such, the images were masked solely for WM. Whole-brain T_1 -weighted magnetization-prepared rapid gradient-echo (MP-RAGE) 3D volumes ($1 \times 1 \times 1\text{mm}^3$) were acquired: $\text{TE/TR/TI} = 3.32/2300/900\text{ ms}$, parallel imaging acceleration factor = 2, bandwidth (BW) = 230 Hz/Px, $5\text{ m }30\text{ s scan time}$. Tissue classification maps (WM, GM, CSF) were estimated via Intensity Normalized Stereotaxic Environment for the Classification of Tissue [172] using the MPRAGE data with the International Consortium for Brain Mapping-152 atlas. WM tissue masks

were resampled to match the AC-PC $2 \times 2 \times 5\text{mm}^3$ single slices using a majority voting analysis (75% threshold). The histograms of WM qMT parameters were calculated for all three B_1 maps, using both VFA and IR T_1 maps in the processing pipeline. Chi-square (χ^2) of the histogram differences was calculated to quantify how well the histograms matched between the DA case versus AFI and BS.

4.5 Results

4.5.1 Simulations

The error (%) in F calculated after fitting the simulated qMT signal using each B_1 and T_1 value-pair is displayed in Figure 4-2. T_1 curves as a function of B_1 inaccuracies are superimposed with solid (IR) and dotted (VFA) lines. The error in F (%) is a smooth nonlinear function of B_1 and T_1 , with some speckling in values occurring far from the true B_1 and T_1 intersection (where they are both grossly inaccurate). IR T_1 is set to be constant, resulting in a wide range of errors in F (<-100% to 50%) for the B_1 -inaccuracy range evaluated. B_1 underestimation resulted in an overestimation of VFA T_1 , and the error in F for this case overlaps near the 0% error contour line (green).

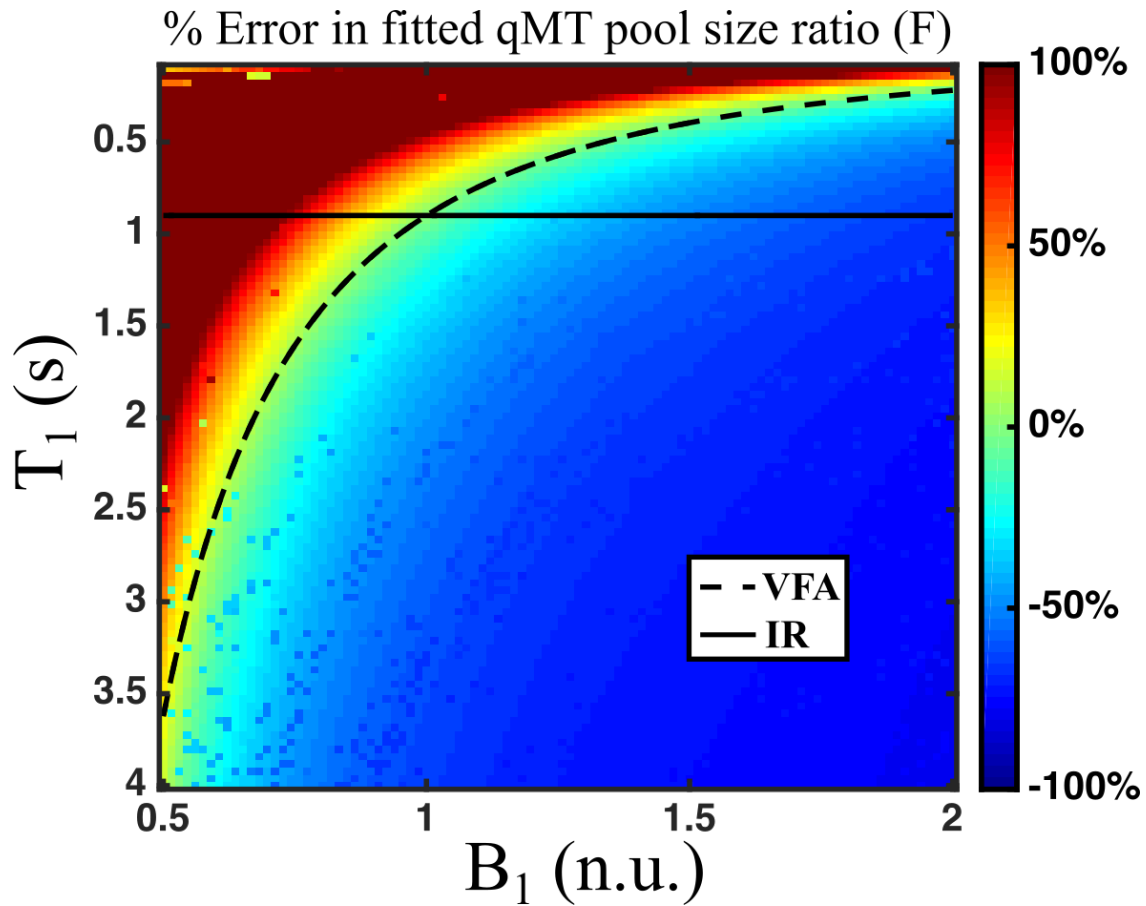


Figure 4-2. Simulated differences (%) in fitted quantitative magnetization transfer (qMT) F values in the presence of a wide range of B_1 and T_1 errors ($B_{1,\text{true}} = 1 \text{ n.u.}$, $T_{1,\text{true}} = 0.9 \text{ s}$). The superimposed lines plot the T_1 distribution for a B_1 -independent T_1 mapping method (inversion recovery [IR], solid line, and variable flip angle [VFA], dashed line). n.u. = normalized units.

At 3T, the B_1 amplitude varies approximately $\pm 30\%$ in the brain. The errors in the four qMT fitted parameters are shown for this range of B_1 inaccuracy in Figure 4-3, for both the IR and VFA T_1 cases. Note that Figure 4-3a corresponds to the values superimposed by the IR and VFA T_1 lines in Figure 4-2. Relative to IR, errors in F due to B_1 inaccuracies are substantially reduced using VFA. For VFA, the errors in F ranged between -3% and 7% (blue line) for $\pm 30\%$ B_1 inaccuracy; for IR, the errors ranged between -40% and >100% (red line). k_f exhibits the inverse trend; errors in k_f are larger for VFA relative to IR (Figure 4-3b) for all B_1 values. No advantage in either T_1 method is identified for $T_{2,f}$; the slopes of the curves flip between both T_1 methods with

approximately the same magnitude. $T_{2,r}$ is insensitive to B_1 inaccuracies for both T_1 mapping method (Figure 4-3d).

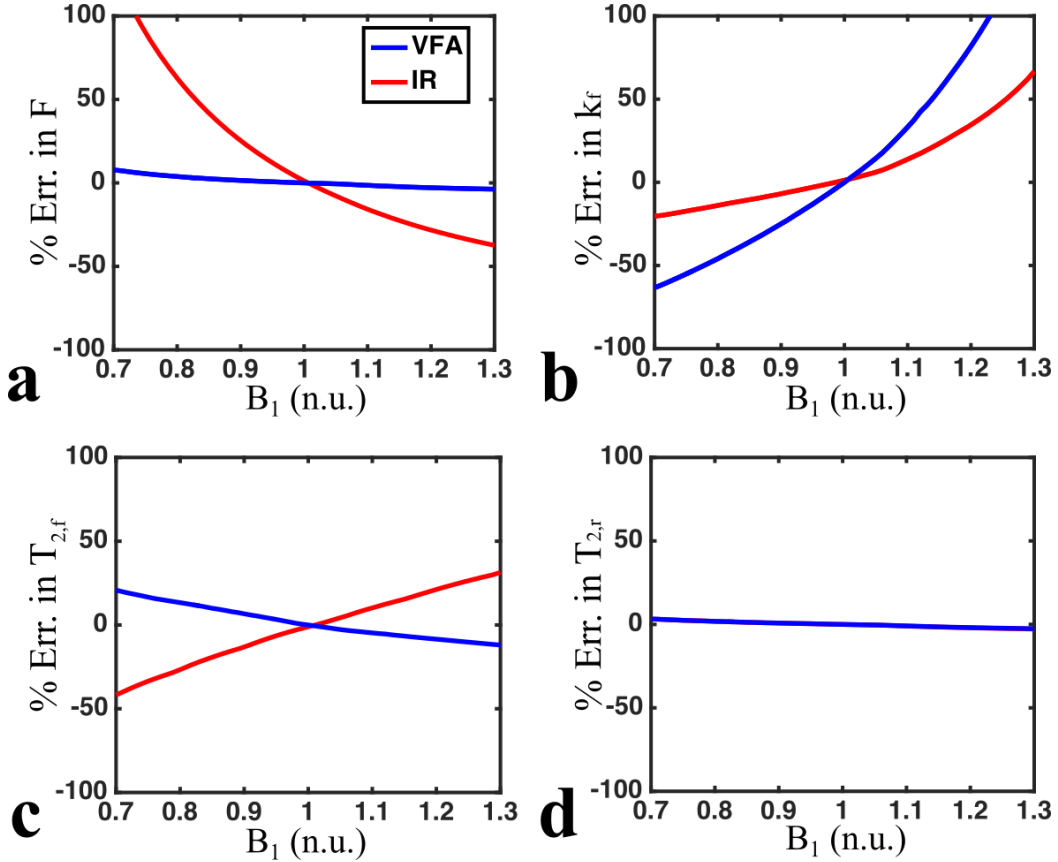


Figure 4-3. Simulated errors (%) in fitted quantitative magnetization transfer (qMT) parameters for $\pm 30\%$ B_1 errors (a: pool size ratio [F], b: magnetization exchange rate [k_f], c: free pool T_2 [$T_{2,f}$], d: restricted pool T_2 [$T_{2,r}$]). Fits using a B_1 -independent T_1 measure (inversion recovery [IR]) are shown in red, and those using variable flip angle (VFA) T_1 mapping are shown in blue. The IR curve in d) is underneath the VFA line. Note: The solid and dashed lines in Figure 4-3 to show the dependence of IR and VFA T_1 on B_1 . n.u. = normalized units.

For IR, a 10% underestimation in B_1 produced a 23% error in F , 6% error in k_f , 12% error in $T_{2,f}$, and 0.78% error in $T_{2,r}$. For VFA, a 10% underestimation in B_1 produced a 1.5% error in F , 25% error in k_f , 6.7% error in $T_{2,f}$, and 0.78% error in $T_{2,r}$. Thus, switching from IR to VFA reduces B_1 -sensitivity of F by a factor of 15 for a 10% error in B_1 . The error in F for the IR case (23%) produced from a 10% error in B_1 is consistent with the value calculated by Sled and Pike using a 60-point protocol (20%) [145].

4.5.2 Sensitivity Analysis

The plots of the sensitivity values for our qMT protocol are shown in Figure 4-4, and the sensitivity metrics (from Eqs. (4-3) and (4-4)) are calculated in Table 4-1. The curve similarity metric $|\hat{S}_p \cdot \hat{S}_{B_1}|$ informs us of how well changing a particular fitting parameter p (F , k_f , $T_{2,f}$, and $T_{2,r}$) can correct the expected signal change due to an error in B_1 . For a B_1 -independent T_1 measurement (e.g., IR), we see from Table 4-1 that the $|\hat{S}_p \cdot \hat{S}_{B_1}|$ values have the following trend: $(F \approx 1) > k_f > T_{2,f} \gg T_{2,r}$, for VFA: $(k_f \approx 1) > F \approx T_{2,f} \gg T_{2,r}$. This suggests that F has a higher sensitivity to B_1 inaccuracies for IR than VFA, with a reverse relationship expected for k_f , both in agreement with the simulations results from the Simulations section. Figure 4-4 illustrates these relationships; the sensitivity curves for B_1^{IR} (Figure 4-4a) have a similar pattern to those for F (Figure 4-4c), whereas the sensitivity curves for B_1^{VFA} (Figure 4-4b) have a similar pattern to those for k_f (Figure 4-4d).

For these respective cases, $\frac{B_1}{p} \frac{\|S_{B_1}\|}{\|S_p\|}$ is greater for k_f than F (Table 4-1), suggesting that larger relative errors in k_f are required to compensate B_1^{VFA} inaccuracies than F for B_1^{IR} , consistent with our simulation observations. Lastly, note that the minima observed in $|S_{B_1}|$ is due to a zero-crossing of $S_{T_{2,r}}$, a characteristic that was also reported in a previous study [198].

Table 4-1. qMT Z-spectra sensitivity comparison metrics for B_1 (accounting for the B_1 -sensitivity of each T_1 method, IR and VFA) and each fitted qMT parameter.

	$ \hat{S}_p \cdot \hat{S}_{B_1} $		$\frac{B_1}{p} \frac{\ S_{B_1}\ }{\ S_p\ }$	
	$S_{B_1}^{IR}$	$S_{B_1}^{VFA}$	$S_{B_1}^{IR}$	$S_{B_1}^{VFA}$
S_F	0.975	0.754	2.05	1.07
S_{k_f}	0.815	0.951	6.02	3.12
$S_{T_{2,f}}$	0.704	0.776	4.67	2.43
$S_{T_{2,r}}$	0.482	0.552	3.08	1.61

Note: $S_{B_1}^{IR}$ corresponds to the qMT sensitivity values relative to B_1 assuming a B_1 -independent measure of T_1 , whereas $S_{B_1}^{VFA}$ considers a qMT protocol using a VFA T_1 measurement, which inherently is B_1 -dependent. IR = inversion recovery; qMT = quantitative magnetization transfer; VFA = variable flip angle.

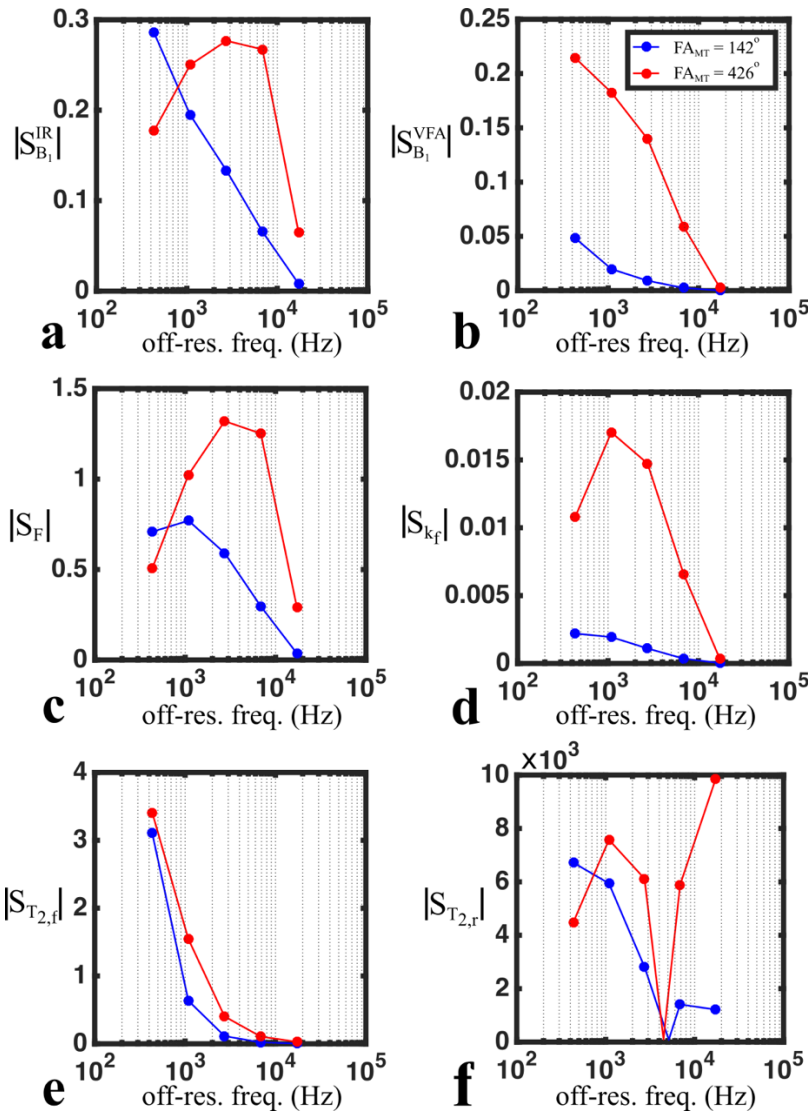


Figure 4-4. Sensitivity analysis of the magnetization transfer signal relative to B_1 (a, b) and fitting variables (c–f). The plots (note scale changes) show the magnitudes of the sensitivity values (Eq. (4-2)).

4.5.3 B_1 -Sensitivity of qMT in Healthy Subjects

Noise, partial volume effects of tissue, and a wide range of different qMT tissue parameters were not considered in the previous sections, all of which could potentially impact the B_1 -sensitivity of the qMT fits. *In vivo* data were acquired to investigate whether the B_1 -sensitivity features identified in our simulations hold under real-world conditions. Single-slice qMT parameter maps are shown in Figure 4-5, fitted using VFA (a) and IR (b), for either DA B_1 maps or the nominal flip angle

assumption ($B_{1,\text{Flat}} = 1$). For VFA and $B_{1,\text{Flat}}$, the elevated T_1 at the center of the brain counteracts the underestimated B_1 values, resulting in minimal errors in the qMT F maps relative to the IR F maps. At the perimeter of the brain where $B_{1,\text{Flat}}$ overestimates the measured values, the VFA case results in nearly no qMT F bias. Regions of very high T_1 , suggesting presence of CSF, do exhibit speckling of large errors in F. qMT F fitted with the combination of IR and $B_{1,\text{Flat}}$ resulted in large errors, where the B_1 profile is clearly distinguishable in map of errors in F.

Table 4-2 lists the correlation and linear regression slope ($B_{1,\text{DA}}$ vs. $B_{1,\text{Flat}} = 1$) for all fitted qMT parameters, using both T_1 methods. qMT F using VFA had the best correlation ($\rho = 0.97$, slope = 0.97), as opposed to IR ($\rho = 0.81$, slope = 0.57). $T_{2,f}$ also demonstrated good correlations ($\rho = 0.97$), but with an underestimation of the slope (slope = 0.86). Based on our simulations, the low correlation of k_f for the IR case ($\rho = 0.26$) was unexpected. Upon further investigation of the raw k_f scatter plots (not shown), the linear assumption for fitting the k_f scatter plot was violated. Thus, for conditions exhibited *in vivo* (i.e., noise, multi-tissue voxels), the k_f parameter fits were not stable in the presence of large B_1 errors, resulting in k_f voxel values diverging substantially in the scatter plot data.

Table 4-2. Pooled (all subjects) Pearson correlation coefficients and linear regression slopes for qMT values comparing measured DA B_1 maps and fictitious $B_{1,\text{Flat}} = 1$ maps^a.

($B_{1,\text{DA}}$) vs. ($B_{1,\text{Flat}} = 1$)

qMT	$T_{1,\text{VFA}}$		$T_{1,\text{IR}}$	
	Pearson ρ	Slope	Pearson ρ	Slope
F	0.97	0.97	0.81	0.57
k_f	0.27	0.24	0.26	0.25
$T_{2,f}$	0.97	0.86	0.93	0.90
$T_{2,r}$	0.81	0.78	0.89	0.82

^a $B_{1,\text{Flat}} = 1$ is equivalent to the nominal flip angle assumption DA = double angle; qMT = quantitative magnetization transfer.

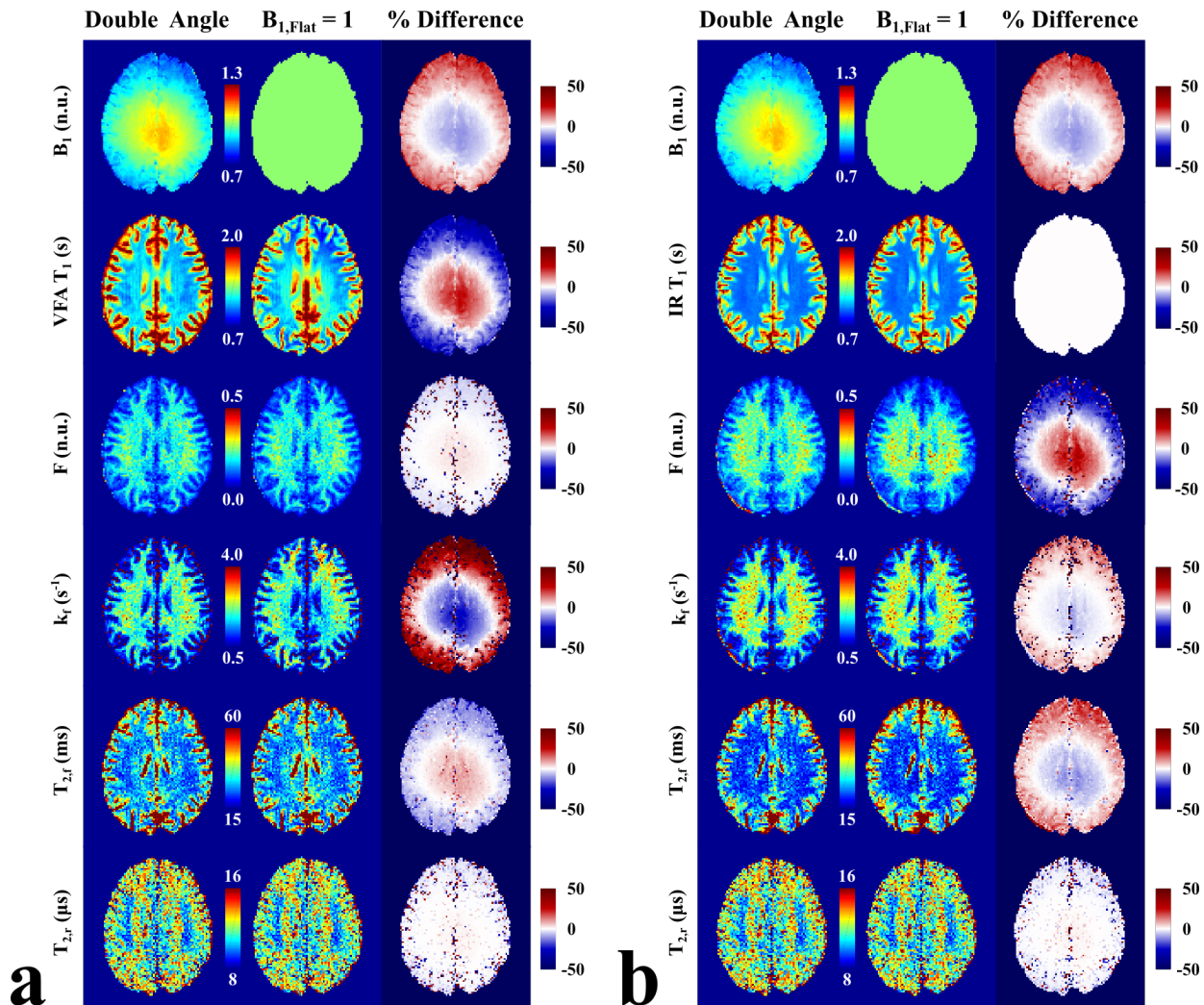


Figure 4-5. Single-subject comparison of quantitative magnetization transfer parameter maps fitted using double angle and $B_{1,\text{Flat}} = 1$ maps using (a) variable flip angle (VFA) T_1 maps corrected using the corresponding B_1 map, and (b) inversion recovery (IR) T_1 maps independent of B_1 .

Expanding the correlation analysis of F to a larger $B_{1,\text{Flat}}$ set of values (ranging from 0.5 to 2 n.u.), F was more robust against B_1 overestimations than underestimations (Figure 4-6a). The correlations break down rapidly for $B_{1,\text{Flat}}$ values below 0.75, yet are near unity for most values ranging between 1 and 2. The same trend is true for the fit slope for F; it is near unity for slight B_1 underestimations and for large B_1 overestimations (Figure 4-6b).

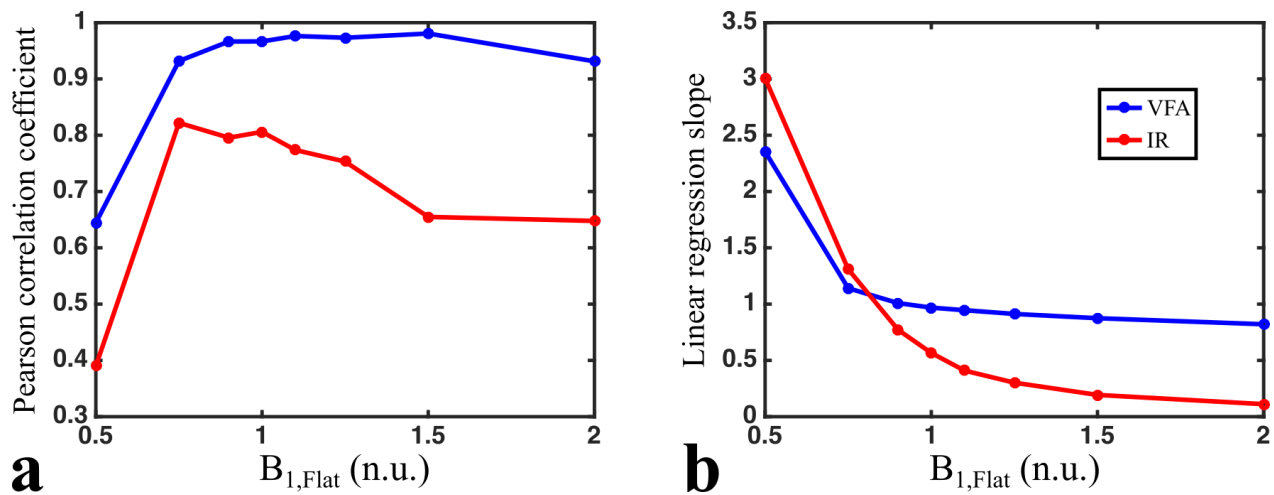


Figure 4-6. Pooled (all subjects, voxel-wise) whole brain Pearson correlation coefficients (a) and linear regression slopes (b) for qMT F values between the measured double angle B_1 maps and generated $B_{1,\text{Flat}}$ maps. IR = inversion recovery; n.u. = normalized units; VFA = variable flip angle.

4.5.4 B_1 Mapping Method Comparison

Three B_1 maps (DA, AFI, BS) are shown for one subject in Figure 4-7. The DA B_1 map, which was used in the previous section, was set as the reference measurement that the two other methods are compared against. AFI and BS displayed heterogeneous inaccuracy patterns relative to DA; voxel-wise relative errors were $\pm 10\%$. In this subject, B_1 in the frontal lobe was overestimated by both methods, whereas the left and right posterior regions showed different bias patterns for both techniques. Relative to DA, the voxelwise Pearson correlation and linear regression coefficients for all three subjects were $\rho = 0.904$ ($y = 1.035 x - 0.034$) for BS and $\rho = 0.912$ ($y = 0.960 x + 0.038$) for AFI. Despite variations in voxelwise accuracy between B_1 methods, the histograms of

WM qMT F matched very well for the VFA case (Figure 4-8b, same subject as Figure 4-7). The excellent overlap of histogram curves for this case resulted in low χ^2 values for this subject ($\chi^2_{AFI} = 1.24$, $\chi^2_{BS} = 1.41$), unlike to the IR case for F ($\chi^2_{AFI} = 5.45$, $\chi^2_{BS} = 6.40$). Consistent with our simulations, the inverse relationship was true for k_f in WM (Figure 4-8c,d). The mean χ^2 values of F for all subjects also had low standard deviations for VFA ($\chi^2_{AFI} = 1.24 \pm 0.33$, $\chi^2_{BS} = 1.41 \pm 0.12$) relative to IR ($\chi^2_{AFI} = 9.25 \pm 5.81$, $\chi^2_{BS} = 9.17 \pm 3.94$; Figure 4-8a). For k_f , the means for all subject for VFA were $\chi^2_{AFI} = 6.10 \pm 1.81$, $\chi^2_{BS} = 9.00 \pm 3.45$, and for IR were $\chi^2_{AFI} = 1.44 \pm 0.42$, $\chi^2_{BS} = 2.44 \pm 1.21$. These results demonstrate the robustness of VFA for qMT F, even in the presence of local inaccuracies acquired in similar B_1 maps, and that B_1 maps containing minor artifacts can be used without degradation in quantitative F value precision.

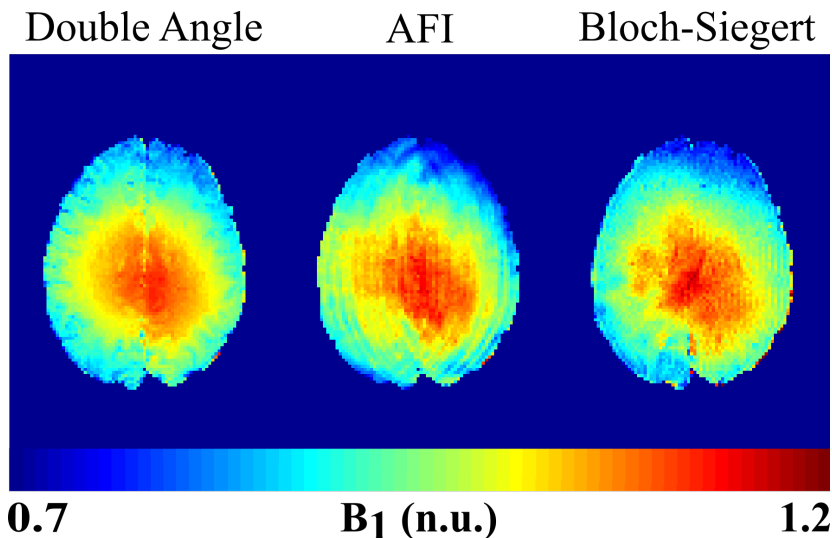


Figure 4-7. B_1 map comparison in a single subject using three different acquisition techniques: double angle method, actual flip angle imaging (AFI), and Bloch-Siegert shift. n.u. = normalized units.

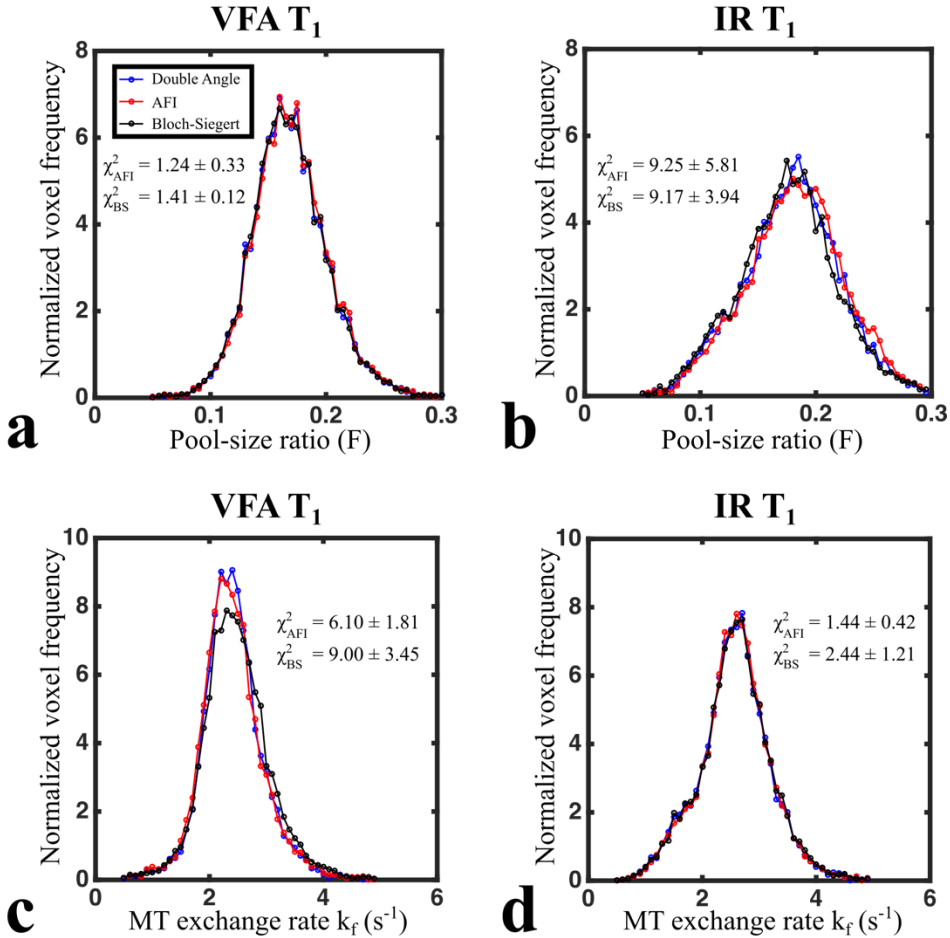


Figure 4-8. Single-subject white matter pool-size ratio (F) (a, b) and magnetization transfer (MT) exchange coefficient (k_f) (c, d) distributions for three B_1 mapping methods, using inversion recovery (IR) T_1 mapping (a, c) or variable flip angle (VFA) T_1 mapping (b, d). χ^2 values of the actual flip angle (AFI) and Bloch-Siegert shift (BS) histograms were calculated relative to double angle.

4.6 Discussion

Our findings demonstrate that the B_1 -sensitivity of off-resonance MT-prepared SPGR qMT parameters is strongly influenced by the T_1 mapping method used. We showed that the robustness of the fitted qMT parameters is impacted by the choice between a B_1 -independent and a B_1 -dependent T_1 mapping method impacts. Overall, the pool-size ratio F was shown to be most robust against B_1 errors when VFA T_1 mapping is used. Using simulations, we found that a 10% overestimation in B_1 results in a 1.5% error in F if VFA is used for T_1 mapping. This B_1 -induced error in F was 15 times less than for B_1 -independent methods such as IR (23% error in F). Although

possibly a counter-intuitive prediction, the increased robustness in F against errors in B_1 for a B_1 -dependent T_1 method is made possible due to other fitting parameters (particularly k_f) being more compatible to compensate the expected signal errors for this case. *In vivo* measurements were in agreement with our simulations; the F maps fitted using the nominal flip angle assumption (B_1 inaccuracy ranging between -10% and 25%) and VFA T_1 -mapping correlated strongly with the case using a measured B_1 map ($\rho = 0.97$). Histogram comparisons of WM qMT F between three different B_1 mapping methods showed that VFA could result in four to five times better histogram matching (χ^2 values) in the presence of B_1 inaccuracies compared to IR.

Although most B_1 mapping methods are designed to be robust to common sources of potential artifacts (i.e., tissues with long T_1), there is no well-accepted gold standard method for accurately imaging B_1 . Our comparison between three well-accepted B_1 imaging methods showed that $\pm 10\%$ in voxel-wise differences between B_1 maps can be reasonably expected, resulting in inevitable B_1 inaccuracies regardless of which technique is chosen. In addition, B_1 maps are typically filtered with large blurring kernels (10mm^3) [92,173,181], because B_1 maps are expected to have a smoothly varying profile [170]. In the presence of local highly inaccurate voxels, blurring filters can have the unintended effect of biasing nearby voxels. Blurring filters can also be less effective in cortical grey matter due to edge effects, an area that is already sensitive to inaccuracies due to partial volume effects with CSF. Resampling low-resolution B_1 maps for higher resolution qMT applications means that some inaccurate B_1 information will inevitably be used in qMT postprocessing. Overall, some inaccuracies in B_1 maps must be considered when planning the qMT acquisition protocol to minimize the sensitivity of the qMT parameter(s) of interest to this source of error.

The B_1 -sensitivity characteristics reported here are limited to the qMT imaging method and model that were used. Several other qMT techniques could benefit from a similar analysis; well-established pulsed SPGR qMT alternatives include the Ramani [150] and the Yarnykh [92] models. A key difference between these three MT models is in how they approximate the MT pulse power [152]. As B_1 is primarily used as a corrective factor for the MT pulse power, B_1 -sensitivity will likely vary between these methods and could be explored in future work. Our sensitivity analysis results may also suggest that the B_1 -sensitivity will vary depending on certain key Z-spectrum acquisition choices, particularly dependent on how many MT powers are used. The number of MT powers is conventionally limited to two; however, optimized acquisition schemes have used anywhere between one [75,198] and eight MT pulse powers [165].

Despite the fact that VFA T_1 mapping benefits qMT by improving the robustness of F , even for the extreme case of no B_1 correction at all, certain limitations must be carefully taken into consideration prior to integration into a protocol. As shown with simulations and *in vivo*, the increase in robustness of one qMT parameter for a certain choice of T_1 method (e.g., IR or VFA) results in a reduction in robustness of the other fitted parameters. For instance, a study whose aim is to compare all the qMT parameters should refrain from omitting B_1 mapping, even if VFA is used, as k_f will be inaccurate in several regions. Accurate T_1 maps, which are valuable to many studies because they correlate with disease characteristics, would also be compromised if measuring B_1 is omitted in a qMT protocol that uses VFA. However, for circumstances where the certain qMT parameters have been well-characterized for the disease of interest (e.g., multiple sclerosis), choosing to improve the accuracy and robustness of one parameter (e.g., F) at the expense of others may be justified. Reducing the number of measurements to benefit one qMT parameter at the expense of others has been reported previously; for example, constraining

multiple fitting parameters was used to achieve a single off-resonance qMT measurement technique of the pool-size ratio [75,198].

4.7 Conclusion

In summary, our work revealed the strong dependency of qMT B_1 -sensitivity on the choice of T_1 mapping. Choosing carefully between a B_1 -independent and B_1 -dependent T_1 mapping method can greatly improve the precision of certain qMT parameters. Our results showed that, for a pulsed SPGR qMT sequence with uniform Z-spectrum sampling, using VFA T_1 mapping is preferable if the parameter of interest is the pool-size ratio F parameter. The robustness against B_1 inaccuracy is so strong for this case, that B_1 mapping could be omitted altogether without resulting in large differences in fitted qMT F maps. Omitting this measurement could help accelerate lengthy qMT acquisition protocols, at the expense of losing quantitative T_1 information. B_1 -sensitivity of qMT could be further improved by optimizing the Z-spectrum sampling scheme, similar to how qMT acquisition schemes have been optimized for noise performance [165].

4.8 Appendix A

Let us assume an experiment consisting of N measurements $M_{i,\text{meas}}$ ($i = 1, 2 \dots, N$). Fitting the data to a mathematical model, the algorithm is expected converge to a state where $|M_{i,\text{meas}} - M_{i,\text{fit}}|$ is minimized at each point, such that ideally:

$$\begin{pmatrix} M_{1,\text{fit}}(p_1, \dots, p_L) \\ \vdots \\ M_{N,\text{fit}}(p_1, \dots, p_L) \end{pmatrix} \cong \begin{pmatrix} M_{1,\text{meas}} \\ \vdots \\ M_{N,\text{meas}} \end{pmatrix} \quad (4\text{-A1})$$

$M_{i,fit}$ depends on a set model parameters p_k ($k = 1, 2, \dots, L$). For a small error in an measured model parameter $\Delta p_{j,meas}$ (i.e., a calibration measurement, such as B_1 in qMT), the change in each $M_{i,fit}$ is approximated by a Taylor expansion:

$$M_{i,fit}(p_{j,meas} + \Delta p_{j,meas}) = M_{i,fit}(p_{j,meas}) + \sum_{k=1}^L \frac{\partial M_{i,fit}}{\partial p_k} \Delta p_k + \dots \quad (4\text{-A2})$$

The fitting algorithm will nonetheless aim at producing a good fit (Eq. (4-A1)); thus, the following approximations are expected:

$$M_{i,fit}(p_{j,meas} + \Delta p_{j,meas}) \cong M_{i,meas} \equiv M_i \quad (4\text{-A3})$$

$$M_{i,fit}(p_{j,meas}) \cong M_{i,meas} \equiv M_i \quad (4\text{-A4})$$

A first order approximation of the Taylor series for small $\Delta p_{j,meas}$ and substituting for M_i condenses Eq. (4-A2) to:

$$M_i \cong M_i + \sum_{k=1}^L \frac{\partial M_i}{\partial p_k} \Delta p_k \quad (4\text{-A5})$$

The M_i terms cancel, thus any error caused by $\Delta p_{j,meas}$ must be compensated by errors propagated to the remaining fitting parameters Δp for $k \neq j$:

$$\sum_{\substack{k=1 \\ k \neq j}}^L \frac{\partial M_i}{\partial p_k} \Delta p_k = -\frac{\partial M_i}{\partial p_{j,meas}} \Delta p_{j,meas} \quad (4\text{-A6})$$

For the Sled and Pike model of qMT, the calibration measurement we are interested in as a possible source of error in this work is B_1 , and the explicitly fitted parameters are F , k_f , T_{2f} and T_{2r} :

$$\frac{\partial M_i}{\partial F} \Delta F + \frac{\partial M_i}{\partial k_f} \Delta k_f + \frac{\partial M_i}{\partial T_{2f}} \Delta T_{2f} + \frac{\partial M_i}{\partial T_{2r}} \Delta T_{2r} = -\frac{\partial M_i}{\partial B_1} \Delta B_1 \quad (4-A7)$$

The sensitivity of a measurement M_i relative to a model parameter p_k is defined as [195]:

$$S_{p_k,i} \equiv \frac{\partial M_i}{\partial p_k} \quad (4-A8)$$

For a set of N measurements, Eqs. (4-A7) and (4-A8) simplify to matrix form:

$$\begin{pmatrix} S_{F,1} & S_{k_f,1} & S_{T_{2,f},1} & S_{T_{2,r},1} \\ S_{F,2} & S_{k_f,2} & S_{T_{2,f},2} & S_{T_{2,r},2} \\ \vdots & \vdots & \vdots & \vdots \\ S_{F,N} & S_{k_f,N} & S_{T_{2,f},N} & S_{T_{2,r},N} \end{pmatrix} \begin{pmatrix} \Delta F \\ \Delta k_f \\ \Delta T_{2f} \\ \Delta T_{2r} \end{pmatrix} = - \begin{pmatrix} S_{B_1,1} \\ S_{B_1,2} \\ \vdots \\ S_{B_1,N} \end{pmatrix} \Delta B_1 \quad (4-A9)$$

For a given error in B_1 (ΔB_1), Eq. (4-A10) could be minimized to estimate the errors in each fitting parameter (ΔF , Δk_f , ΔT_{2f} , ΔT_{2r}) having known sensitivity values, which can be calculated analytically or through numerical simulations. However, to simplify the analysis, we chose to compare each fitting parameter p_k independently to find possible easy-to-understand metrics to compare fitting parameter sensitivity to B_1 inaccuracies. For each fitting parameter of interest (Δp), we set all other Δp_k values to 0. Equation (4-A9) now simplifies to a vector equation:

$$\mathbf{S}_p \Delta p = -\mathbf{S}_{B_1} \Delta B_1 \quad (4-A10)$$

where \mathbf{S}_p is the column vector for the parameter of interest p in Equation (4-A9), similar to \mathbf{S}_{B_1} .

This equation is solved for Δp by doing the scalar product of \mathbf{S}_p on both sides of the equation, and

separating the norm of the vectors ($\|\mathbf{S}\|$) and their unit vectors ($\hat{\mathbf{S}}$). Also, because Δp and ΔB_1 are absolute errors, they are scaled by the parameter values ($\Delta p = \delta p \cdot p$, where δp is the relative error). To better compare each parameter, the relative error is preferred:

$$\delta p = -\frac{B_1}{p} \frac{\|\mathbf{S}_{B_1}\|}{\|\mathbf{S}_p\|} (\hat{\mathbf{S}}_p \cdot \hat{\mathbf{S}}_{B_1}) \delta B_1 \quad (4\text{-A11})$$

Thus, for a given relative error in B_1 (δB_1), the parameter p , which maximizes $|\hat{\mathbf{S}}_p \cdot \hat{\mathbf{S}}_{B_1}|$ for a given measurement protocol, will likely have larger inaccuracies $|\delta p|$ than the other fitting parameters. This can be visualized easily, because $|\hat{\mathbf{S}}_p \cdot \hat{\mathbf{S}}_{B_1}| \approx 1$ means that the sensitivity curves for B_1 and p nearly match, and any change in the Z-spectrum expected by an inaccurate B_1 can be nearly completely compensated solely by adjusting that fitting parameter. The error induced (δp) will then proportional to the ratio of overall sensitivities $\frac{B_1}{p} \frac{\|\mathbf{S}_{B_1}\|}{\|\mathbf{S}_p\|}$.

4.9 Acknowledgements

Funding for M.B. was provided by the National Sciences and Engineering Research Council of Canada with the Alexander Graham Bell Canada Graduate Scholarships – Doctoral program. Funding to G.B.P. was provided by the Canadian Institutes of Health Research, and Campus Alberta Innovates Program also supported this research.

Chapter 5

Sensitivity-Regularization of the Cramér-Rao Lower Bound to Minimize B_1 Nonuniformity Effects in Quantitative Magnetization Transfer Imaging

5.1 Preface

In the previous chapter, we reported differences in the sensitivity of qMT fitting parameters in the presence of B_1 inaccuracies between different T_1 mapping methods, and investigated these differences for a fixed qMT measurement protocol (“uniform”: logarithmically uniform off-resonance frequencies). We concluded that VFA T_1 mapping is the most robust approach for estimating the qMT pool-size ratio in the presence of B_1 -inaccuracies. The next logical step is to investigate how the B_1 -sensitivity of qMT will change for a fixed T_1 mapping method, but between different qMT measurement protocols. Or more generally, can the qMT acquisition protocol itself be optimized for reduced B_1 -sensitivity?

The following manuscript, submitted to the journal *Magnetic Resonance in Medicine*, describes a new approach to optimizing qMT acquisition protocols for B_1 -insensitivity, by sensitivity-regularizing the Cramér-Rao lower bound (CRLB) with an iterative optimization algorithm. A short theoretical derivation of the regularization condition is presented, as the fundamentals of it is described in detail in Section 4.8 (Appendix A of the previous manuscript). The regularization term was optimized using simulations to minimize the error in the pool-size ratio, while reducing the impact on the CRLB (a marker for the sensitivity to noise). Using Monte Carlo Simulations, three protocols were compared (Uniform , CRLB, and CRLB with B_1 -sensitivity regularization) for a wide range of conditions (SNRs, B_1 -inaccuracies, different tissues). All the code developed

for this project wraps around an open-source quantitative MRI Matlab package currently available online (a project I was also involved with a resulting publication – Cabana et al. 2015 (not included in this thesis)), and the optimization code developed for this current work has also been released as an open-source package (<http://github.com/mathieuboudreau/qmt-optimization>).

Sensitivity-Regularization of the Cramér-Rao Lower Bound to Minimize B_1 Nonuniformity Effects in Quantitative Magnetization Transfer Imaging

Mathieu Boudreau and G. Bruce Pike

McConnell Brain Imaging Centre, Montreal Neurological Institute
3801 University Street, McGill University
Quebec, Canada, H3A 2B4

Submitted to Magnetic Resonance in Medicine (2017)

5.2 Abstract

Purpose: To develop and validate a regularization approach of optimizing B_1 -insensitivity of the quantitative magnetization transfer (qMT) pool-size ratio (F).

Theory and Methods: An expression describing the impact of B_1 -inaccuracies on qMT fitting parameters was derived using a sensitivity analysis. To simultaneously optimize for robustness against noise and B_1 -inaccuracies, the optimization condition was defined as the Cramér-Rao lower bound (CRLB) regularized by the B_1 -sensitivity expression for the parameter-of-interest (F). qMT protocols were iteratively optimized from an initial search space, with and without B_1 -regularization. Three 10-point qMT protocols (Uniform, CRLB, CRLB+ B_1 -regularization) were compared using Monte Carlo simulations for a wide range of conditions (SNR, B_1 -inaccuracies, tissues).

Results: The B_1 -regularized CRLB optimization protocol resulted in the best robustness of F against B_1 -errors, for a wide range of SNR and for both white and grey matter tissues. For SNR = 100, this protocol resulted in errors of less than 1% in mean F values for B_1 -errors ranging between -10 to 20%, the range of B_1 values typically observed *in vivo* in the human head at field strengths of 3 T and less. Both CRLB-optimized protocols resulted in the lowest σ_F values for all SNRs, and did not increase in the presence of B_1 -inaccuracies.

Conclusion: This work demonstrates a regularized optimization approach for improving the robustness of auxiliary measurements (e.g. B_1) sensitivity of qMT parameters, particularly the pool-size ratio (F). Predicting substantially less B_1 -sensitivity using protocols optimized with this method, B_1 mapping could even be omitted for qMT studies primarily interested in F .

5.3 Introduction

Quantitative magnetization transfer (qMT) imaging is a class of techniques that indirectly probe tissue macromolecular content, which is not directly observable using conventional MRI due to their inherently short T_2^* . Most qMT techniques quantify properties of macromolecular hydrogen (“restricted pool”) relative to nearby liquid water molecules (“free pool”) by solving the Bloch-McConnell equations, which describes the magnetization exchange between these two interacting pools [144]. Particularly, the pool-size ratio F (ratio of equilibrium magnetization between both pools) is a qMT parameter that correlates strongly with myelin content [42,187]. As such, the pool-size ratio has been proposed as a potential biomarker for lesion monitoring in multiple sclerosis (MS) patients [154,189], and has been shown to correlate with de- and remyelination in a mouse model of MS [158].

Several techniques have been developed to acquire and model qMT data. Most commonly, qMT data are acquired using pulsed off-resonance MT-prepared spoiled gradient echo (SPGR) pulse sequences [145], however techniques using inversion recovery [191] and balanced steady-state free precession have also been proposed [190]. Analytically solving the Bloch-McConnell equations is challenging unless a long continuous-wave MT pulse is used [143], which is impractical for *in vivo* measurements. Several fitting models have been developed to estimate quantitative parameters from pulsed SPGR qMT data [145,150,151], each with unique sets of experimental assumptions and approximations. In addition, SPGR qMT techniques require several additional quantitative measurements, such as main field (B_0) mapping, transmit radiofrequency (RF) field (B_1) mapping, and longitudinal relaxation time (T_1) mapping. In this context, B_0 mapping is used to calibrate the off-resonance frequency values in the presence of main field inhomogeneity [197], B_1 mapping to correct the RF field amplitude variations [84,199], and T_1

mapping to constrain the magnetization transfer fitting parameters [143,145,200]. These three measurements, in addition to the 10+ qMT measurements typically required to fit the full set of model parameters [165], makes it a challenge to acquire qMT data in a clinically feasible acquisition time.

Several strategies have been developed to shorten the SPGR qMT acquisition time, which originally consisted of over 60 qMT measurements [145] and limited the technique to single slice acquisitions. The first three-dimensional qMT brain scan was achieved using a “uniform” acquisition protocol by reducing the number of off-resonance frequencies (Δ) to 5 (uniformly ranging between 400 Hz and 20 kHz) and MT flip angles (FA_{MT}) to 2 (high and low values), for a total of MT-weighted 10 measurements [193]. Other studies went further, optimizing the protocol Δ and FA_{MT} values using the Cramér-Rao lower bound (CRLB) as an optimization condition to minimize estimated parameter variances, using simulated annealing [164] or an iterative protocol reduction algorithm from an initial search space [165]. Rapid k-space readout techniques such as echo planar imaging have also been proposed to improve acquisition times [201]. The choice of $B_0/B_1/T_1$ mapping techniques have evolved over time, with researchers typically choosing the most rapid and reliable technique available at their disposal. For example, the evolution from single-slice qMT imaging to whole-brain imaging required a switch from single-slice T_1 mapping techniques (e.g. inversion recovery – IR, Look-Locker – LL) to 3D techniques (e.g. Variable Flip Angle – VFA). However, recent work has shown that this transition may impact the robustness of the fitting parameters, since IR is a B_1 -insensitive technique [55], whereas VFA is a B_1 -sensitive technique [64]. For a uniform 10-pt SPGR qMT protocol, it has been demonstrated that the pool-size ratio F is much less sensitive to B_1 -inaccuracies if the qMT protocol uses VFA T_1 mapping, relative to B_1 -insensitive T_1 mapping techniques [202]. Since that work used a fixed “uniform”

qMT sampling protocol to demonstrate the benefit of using VFA T_1 mapping for F, it raises an interesting question: is it possible to further improve the robustness of F against B_1 inaccuracies by optimizing the qMT acquisition protocol itself for B_1 -insensitivity?

The aim of this work is to develop a method to incorporate B_1 -sensitivity considerations into the optimization of qMT data acquisition, by regularizing the CRLB optimization condition with a B_1 -sensitivity term. We first derived a B_1 -sensitivity expression that was used to regularize the CRLB condition. Using simulations, we then explored the B_1 -sensitivity of qMT for several different uniform sampling protocol configurations. The optimal regularization term for the pool-size ratio was determined, and a sample qMT protocol was iteratively optimized using the CRLB condition both with and without the regularization term. The robustness of three protocols (uniform, CRLB, CRLB + B_1 regularization) were then investigated using Monte Carlo simulations for a range of signal-to-noise ratios (SNR), B_1 -inaccuracies, and tissue values. Lastly, the qMT optimization framework developed and presented here is released as an open-source package.

5.4 Theory

In the presence of a small inaccuracy of a measurement parameter, such as B_1 in qMT, this error will propagate to the fitting parameters of the model. The behavior of how this propagated error will impact each fitting parameter can be explored through a sensitivity analysis, by expanding the fitted signal in the presence of a ΔB_1 with a Taylor expansion [195]. Assuming a small ΔB_1 and a good fit ($M(B_1 + \Delta B_1) \approx M(B_1) \approx M_{\text{meas}}$, where M is the signal generated by the fit), a first-order approximation of the Taylor expansion of the fitted signal results in the following matrix equation [202]:

$$\mathbf{S}_p \Delta \mathbf{p} \cong -\mathbf{S}_{B_1} \Delta B_1 \quad (5-1)$$

where p are the model fitting parameters (e.g. for the Sled and Pike[144] model of qMT: F , k_f , $T_{2,f}$, $T_{2,r}$), $\Delta \mathbf{p}$ is the column vector of errors in fitted parameters $[\Delta F, \Delta k_f, \Delta T_{2,f}, \Delta T_{2,r}]'$, and \mathbf{S} are matrices with sensitivities values elements $(S_{ni} = \frac{\partial M_n}{\partial p_i}, \text{ where } n = 1, 2, \dots N \text{ and } i = 1, 2, \dots Q)$ relative to p_i or B_1 (columns) for each measurement n (rows). \mathbf{S}_p can also be interpreted as being the Jacobian of the measurement for the fitting parameters, which we'll call the Jacobian sensitivity matrix.

Given a known ΔB_1 value and Jacobian sensitivity matrices for p and B_1 , Eq. (5-1) can be solved for $\Delta \mathbf{p}$. However, since Eq. (5-1) is typically an overdetermined system of linear equations ($N \gg Q$), the optimal solution is found by minimizing the following ℓ^2 -norm for $\Delta \mathbf{p}$:

$$\min_{\Delta \mathbf{p}} \|\mathbf{S}_p \Delta \mathbf{p} + \mathbf{S}_{B_1} \Delta B_1\|_2 \quad (5-2)$$

Although Eq. (5-2) provides an estimate of the error propagated to the fitting parameters by an error in B_1 , it alone is insufficient to be used for optimal protocol design. qMT protocols must also be designed for robustness against noise that naturally occurs in measured signals. For this purpose, the Cramér-Rao lower bound (CRLB) has been shown to be an adequate and sufficient estimate to minimize the variance in fitted qMT parameters due to experimental noise [164]. Consider the Fisher information matrix (FIM) \mathbf{J} , which has elements:

$$J_{ij} = \frac{1}{\sigma^2} \sum_{n=1}^N \frac{\partial M(p_1, \dots, p_Q; \mathbf{x}_n)}{\partial p_i} \frac{\partial M(p_1, \dots, p_Q; \mathbf{x}_n)}{\partial p_j} \quad (5-3)$$

where σ is the standard deviation of the noise, and \mathbf{x}_n is the acquisition protocol for the n^{th} measurement out of N unique measurements. The CRLB is defined as the diagonal elements of \mathbf{J}^{-1} , and the trace of this matrix provides an overall estimate of the minimum variance of a model. However, because the qMT fitting parameters differ largely in their order of magnitudes, the parameter-normalized CRLB (V) is defined instead [164]:

$$V = \sum_i p_i^{-2} [\mathbf{J}^{-1}]_{ii} \quad (5-4)$$

In this work, we propose a regularization approach to simultaneously optimize against both noise (Eq. (5-4)) and B_1 -error propagation (Eq. (5-2)), using an iterative optimization approach for the acquisition protocol design [165]. Particularly, we are interested in minimizing the propagation of B_1 -error to the pool-size ratio F (ΔF) because of its demonstrated potential as a biomarker for myelin content. Thus, to optimally reduce an acquisition protocol of N unique measurements to $N-1$ measurements, each iteration evaluates:

$$\min_{\mathbf{x}^{N-1}} \left(\frac{V_{N-1}}{V_N} + \lambda \operatorname{argmin}_{\Delta F} \|\mathbf{S}_p^{N-1} \Delta \mathbf{p} + \mathbf{S}_{B_1}^{N-1} \Delta B_1\|_2 \right) \quad (5-5)$$

where λ is the regularization parameter constant, and \mathbf{x}^{N-1} is the $N-1$ optimal qMT subset protocol of \mathbf{x}^N for a given iteration. The regularization parameter λ value controls the tradeoff between CRLB (noise) and F sensitivity to B_1 -inaccuracies during the optimization.

5.5 Methods

The core qMT functions and routines used in the simulations and fitting of this work are from qMRLab (<http://github.com/neuropoly/qmt-optimization>), an open-sourced quantitative MRI software packaged that evolved from qMTLab [153] and is written in MATLAB (MATLAB

2017a; MathWorks Inc., Natick, MA). The additional source code developed in this work, particularly for numerically estimating the Jacobians matrices of the system, the protocol optimization algorithms, and the Monte Carlo simulations, is released as its own open-source package (http://github.com/mathieuboudreau/qMTLab_Tabs). The code was developed to wrap around the qMRLab code, so that it may also be easily adaptable with other qMT software packages or in-house code.

5.5.1 Uniform Protocols

The regularization term in Eq. (5-5) proposed for optimizing qMT parameters against B_1 -inaccuracies was derived using a first-order approximation of a Taylor series. To test this approximation, Δp values (ΔF , Δk_f , $\Delta T_{2,f}$, $\Delta T_{2,r}$) were calculated by solving Eq. (5-2) for a range of ΔB_1 typically observed *in vivo* ($\pm 30\%$, with an actual $B_1 = 1.0$ n.u.), and were compared to values estimated by fitting the signal to the Bloch-McConnell equations [145]. A “uniform” qMT measurement protocol was used, meaning a protocol with logarithmically uniform off-resonance frequencies for each MT flip-angle (α_{MT}) preparation pulse. Jacobian sensitivity matrices calculations for Eq. (5-2) (S_p and S_{B_1}) were estimated from numerical partial derivatives ($10^{-2}\%$ relative increase in parameter values). Two different qMT cases were considered for S_{B_1} : B_1 -independent T_1 measurements (IR) and B_1 -dependent T_1 measurements (VFA). Signal simulation details (protocol and tissue parameters) matched those described in full detail in a recent study [165].

Prior to protocol optimization, we were also interested in investigating Δp values (from Eq. (5-2)) for other uniform qMT protocols with different numbers of MT flip angles and off-resonance values. MT-prepared SPGR (TR = 25 ms, $\alpha = 7^\circ$) pulse sequence protocols using every

combination of three α_{MT} values (150° , 400° , 650°) were used (each unique α_{MT} , each combination of two α_{MT} values, and all three). Logarithmically-uniform offset frequencies for each α_{MT} values ranged between 300 Hz and 20 kHz. To fairly assess all uniform protocols, the total number of acquisitions were limited between 8 and 30 by varying the number of offset values per α_{MT} sets. For example, a single- α_{MT} 10-point protocol would have 10 off-resonance frequencies, and a two- α_{MT} 10-point protocol would have the same 5 off-resonance frequencies for both α_{MT} . qMT signals were simulated for tissue values within the typical white matter range (Table 5-1). A 5% overestimation in B_1 value ($\Delta B_1 = +0.05$ n.u.) relative to the expected value ($B_1 = 1$ n.u.) was used for all protocols to solve Eq. (5-2) for Δp , and a VFA T_1 mapping method was assumed (TR = 15 ms, $\alpha = 3^\circ$ and 20°).

5.5.2 Protocol Optimization

qMT protocols were iteratively optimized [165] from a large initial search-space set of potential α_{MT} and Δ protocol values, for fixed TR and α (25 ms and 7°). The most time-intensive component of the optimization algorithm is computing the Jacobian sensitivities (\mathbf{S}_p and \mathbf{S}_{B_1}). The Jacobian sensitivities were precomputed using parallel processing and cached for rapid access during the optimization algorithm execution. Note that both terms in Eq. (5-5) require element values from the Jacobian sensitivity matrices (through Eqs. (5-4) and (5-3)). The optimization search-space consisted of 312 points; each combination of 12 α_{MT} values (ranging between 150° to 700° , in 50° increments) and 26 Δ values (ranging between 300 Hz and 20 kHz, with logarithmically uniform steps). A few (<5%) protocol points resulted in outlier numerical partial derivative values (non-smooth Jacobian sensitivity curve at those points), which may be due to signal simulation rounding errors or imprecise free-pool saturation fraction interpolations in the open-source software used. Those protocol points were replaced with the nearest-neighbor points calculated from a higher-

resolution search-space (101 Δ values). The Jacobian sensitivity matrices were calculated for white matter tissue values (Table 5-1).

Prior to protocol optimization, an optimal value for the regularization parameter λ was determined. The iterative optimization algorithm using Eq. (5-5) was executed for a range of λ values ($\lambda = 0, 0.01, 0.1, 0.5, 1, 2, 5$), assuming $\Delta B_1 = 0.05$ and VFA T_1 mapping ($TR = 15ms, \alpha = 3^\circ$ and 15°). Since TR , TE , and α were fixed for all protocol points, the standard deviation of the noise in Eq. (5-3) (σ) was arbitrarily set to 1 during the optimization calculations. The ΔF values and variance-efficiency curves ($[\text{variance} \times \# \text{ acq. points}]^{-1/2}$, where the variance is interpreted to be the parameter-normalized CRLB V) were compared for each N during the iterative optimization procedure. Two sets of 10-point protocols were optimized by iteratively finding the $N-1$ protocol subset that minimized Eq. (5-5) for $\Delta B_1 = 0.05$ (assuming VFA for T_1 mapping, as above) with and without regularization (CRLB and $CRLB_\lambda$).

5.5.3 Monte Carlo Simulations

Ideal (noiseless) MT-prepared SPGR signals were simulated for three 10-point protocols (Table 5-2: Uniform, CRLB, and $CRLB_\lambda$) and two tissue types (Table 5-1: white matter, grey matter). Rician noise was added to each simulated MT signal and an MT-off signal, for normalization ($M_{MT}/M_{MT\text{-off}}$). Six different SNR levels were considered ($SNR = 25, 50, 75, 100, 150, 200$). Sets of 10,000 noisy MT signals were independently generated and compared for each combination of qMT protocols, tissues, and SNR. Each dataset was subsequently fitted for qMT parameters ($F, k_f, T_{2,f},$ and $T_{2,r}$) considering a range of B_1 errors ($\pm 30\%$ in increments of 5%) and a two-FA VFA T_1 mapping method ($TR = 15ms, \alpha = 3^\circ$ and 15°).

Table 5-1. qMT tissue parameters used to simulate white matter and grey matter tissue values in the Monte Carlo simulations. The parameter definitions are: F – pool-size ratio, k_f – exchange rate constant, $T_{1,f}$ – longitudinal relaxation time of the free pool, $T_{1,r}$ – longitudinal relaxation time of the restricted pool, $T_{2,f}$ – transverse relaxation time of the free pool, $T_{2,r}$ – transverse relaxation time of the restricted pool. The fitting parameters for qMT are F, k_f , $T_{2,f}$, and $T_{2,r}$; $T_{1,f}$ is calculated from the observed T_1 and the fitting parameters, and $T_{1,r}$ is conventionally fixed to 1 s.

Parameter	White Matter	Grey Matter
F	0.15 n.u.	0.075 n.u.
k_f	4.0 s^{-1}	2.5 s^{-1}
$T_{1,f}$	0.9 s	1.3 s
$T_{1,r}$	1.0 s	1.0 s
$T_{2,f}$	30 ms	55 ms
$T_{2,r}$	12 μs	11 μs

Table 5-2. qMT protocols used in the Monte Carlo simulations. The repetition times, excitation flip angles, and number of acquisitions were matched for all protocols. The Uniform protocol is a two MT flip-angle with logarithmically uniform off-resonance frequencies. The CRLB protocol was optimized using Eq. (5-5) with the regularization parameter set to 0, and $\text{CRLB}_{\lambda=0.5}$ was optimized using a regularization parameter of 0.5.

Acq. #	Uniform			CRLB			$\text{CRLB}_{\lambda=0.5}$		
	TR/ α	α_{MT}	Δ (Hz)	TR/ α	α_{MT}	Δ (Hz)	TR/ α	α_{MT}	Δ (Hz)
1			432.9		200.0	300.0		200.0	300.0
2			1 087.5		250.0	1 903.9		200.0	1 609.5
3		142°	2 731.6		700.0	1 609.5		700.0	1 609.5
4			6 861.6		700.0	12 083.6		700.0	12 083.6
5			17 235.5		700.0	1 903.9		700.0	2 252.2
6	25ms/7°		432.9	25ms/7°	250.0	2 252.2	25ms/7°	200.0	1 903.9
7			1 087.5		150.0	300.0		650.0	300.0
8		426°	2 731.6		700.0	1 360.6		200.0	1 360.6
9			6 861.6		200.0	1 609.5		700.0	1 903.9
10			17 235.5		700.0	2 252.2		150.0	300.0

5.6 Results

5.6.1 Uniform Protocols

Figure 5-1 shows the simulated errors in each fitting parameter (ΔF , Δk_f , $\Delta T_{2,f}$, $\Delta T_{2,r}$) estimated from the first-order approximation of the Taylor expansion in Eq. (5-2) (solid lines) and from the relative error in fit using the Sled and Pike model (dash line) in the presence of B_1 errors ($\pm 30\%$). Data was simulated for a B_1 -independent T_1 measure (IR, red) and a B_1 -dependent T_1 measure (VFA, blue) separately. The overall trends in the error curves produced by model fits reproduced well similar simulations that were reported recently [202] (Boudreau et al 2017, Figure 3) even though they don't share the same core qMT simulation and fitting software, establishing confidence in the use of this open-source qMTLab software [153] for this work.

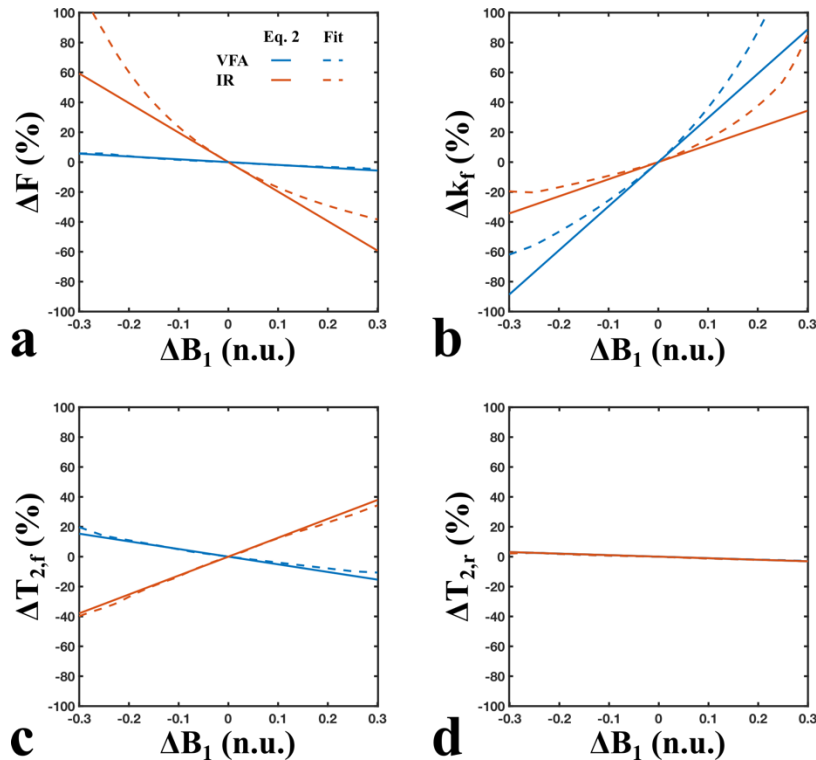


Figure 5-1. Simulated qMT parameter errors due to B_1 -inaccuracies ($-30\% < \Delta B_1 < 30\%$) considering a B_1 -independent T_1 measurement (red: IR – inversion recovery) and a B_1 -dependent T_1 -measurement (blue: VFA – variable flip angle). Solid lines are parameter errors calculated from minimizing Eq. (5-2) (first-order approximation of the Taylor expansion), and dashed lines are parameter errors calculated from fitting the qMT signal according to the Sled & Pike model. The tissue parameters (white matter) and qMT protocol (uniform) were matched to those presented in Boudreau et al. 2017 (see Fig. 3 of the paper).

For B_1 errors within $\pm 5\%$, the errors in all parameters calculated from Eq. (5-2) approximated well the fitted estimates. For VFA T_1 mapping and $\Delta B_1 = 0.05$ n.u. ($+5\%$), the Δp values (Eq. (5-2), Fit) were: $\Delta F = (-0.94\%, -1.06\%)$, $\Delta k_f = (14.77\%, 16.88\%)$, $\Delta T_{2,f} = (-2.56\%, -1.97\%)$, and $\Delta T_{2,r} = (-0.51\%, -0.65\%)$. Both ΔF (for VFA) and $\Delta T_{2,r}$ showed linear trends for the “Fit” case, which resulted in an overall better agreement with Eq. (5-2). Resulting from these analyses, a ΔB_1 of 0.05 n.u. was selected for the iterative optimization calculation (Eq. (5-5)) later in this work.

Figure 5-2 shows the simulated errors of fitting parameters for a 5% ΔB_1 (assuming VFA T_1), using a wide range of uniform qMT acquisition protocols varying in number of FA_{MT} , number of off-resonance frequencies per FA_{MT} , and total number of acquisitions points. While most curves (sets of FA_{MT} combinations) trended asymptotically with increasing number of acquisition points, they did not trend towards 0% parameter error values (except for a few $\Delta T_{2,r}$ cases, $\# FA > 1$ protocols that contain 650°). For ΔF , the three $\# FA = 1$ curves (dark blue, orange, yellow) resulted in the largest ΔF values overall, demonstrating the benefit of including at least two flip angles in your qMT protocol in the context of lower B_1 -sensitivity. The three $\# FA > 1$ protocols that included $FA=650^\circ$ (green, light blue, red) resulted in ΔF curves that overlapped and intercepted $\Delta F = 0\%$ values near 10 and 15 acquisition points, but increased in error for larger $\#$ of acquisition points.

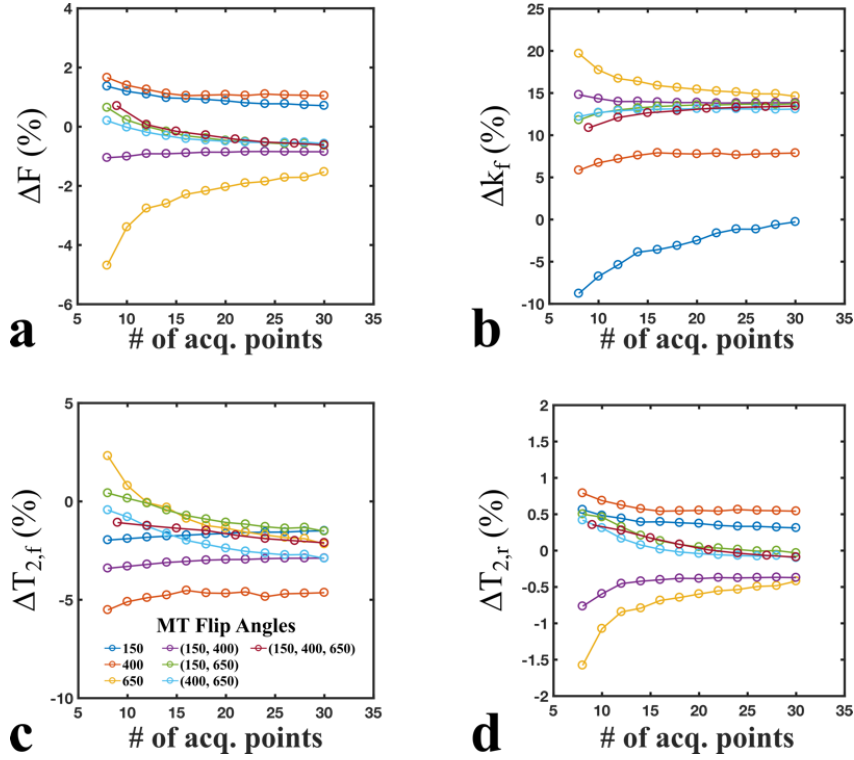


Figure 5-2. Simulated qMT parameter errors estimated from Eq. (5-2) for $\Delta B_1=0.05$ for a wide range of logarithmically-uniform (offsets) qMT protocols. Single (blue, orange, yellow), dual (purple, green, light blue), and triple (red) flip angle combinations of 150° , 400° , and 600° were compared. The number of offset frequencies were uniformly distributed between 300 Hz and 20 kHz, and matched for the total number of acquisition points ($\# \text{ offsets} \times \# \text{ flip angles}$).

5.6.2 Protocol Optimization

Figure 5-3 displays the values of the Jacobian sensitivity matrices (**a-d** are the columns of \mathbf{S}_p , **e** is $\mathbf{S}_{B_1}^{IR}$, and **f** is $\mathbf{S}_{B_1}^{VFA}$). Each plot represents the sensitivity of the Z-spectrum relative to each parameter-of-interest (i.e. the change in Z-spectrum signal value due to a small increase in each parameter). The magnitude of the sensitivity values is shown to simplify interpretations; the sign of the sensitivity curves represents the direction (increase/decrease) that the Z-spectrum changes for small variations of each parameters, while we are mainly concerned in how large of an overall change occurs. A peak of the sensitivity curve for F occurs at off-resonance frequencies an order of magnitude higher for high FA_{MT} ($>500^\circ$) than for low FA_{MT} values ($\sim 150\text{-}300^\circ$). For all FA_{MT} values, the peak sensitivity for k_f remained near $\Delta = 1\text{-}2$ kHz. The peak sensitivity of $\mathbf{S}_{B_1}^{VFA}$ also

remained constant near $\Delta = 1\text{-}2$ kHz, which may explain why k_f has the largest errors due to ΔB_1 (Eq. (5-1)) for the VFA case in Figure 5-1. The higher sensitivity of F at high off-resonance (>10 kHz) values (Figure 5-3a), relative to $S_{B_1}^{VFA}$ (Figure 5-3f), likely contributes to the greater robustness against B_1 observed in the previous section.

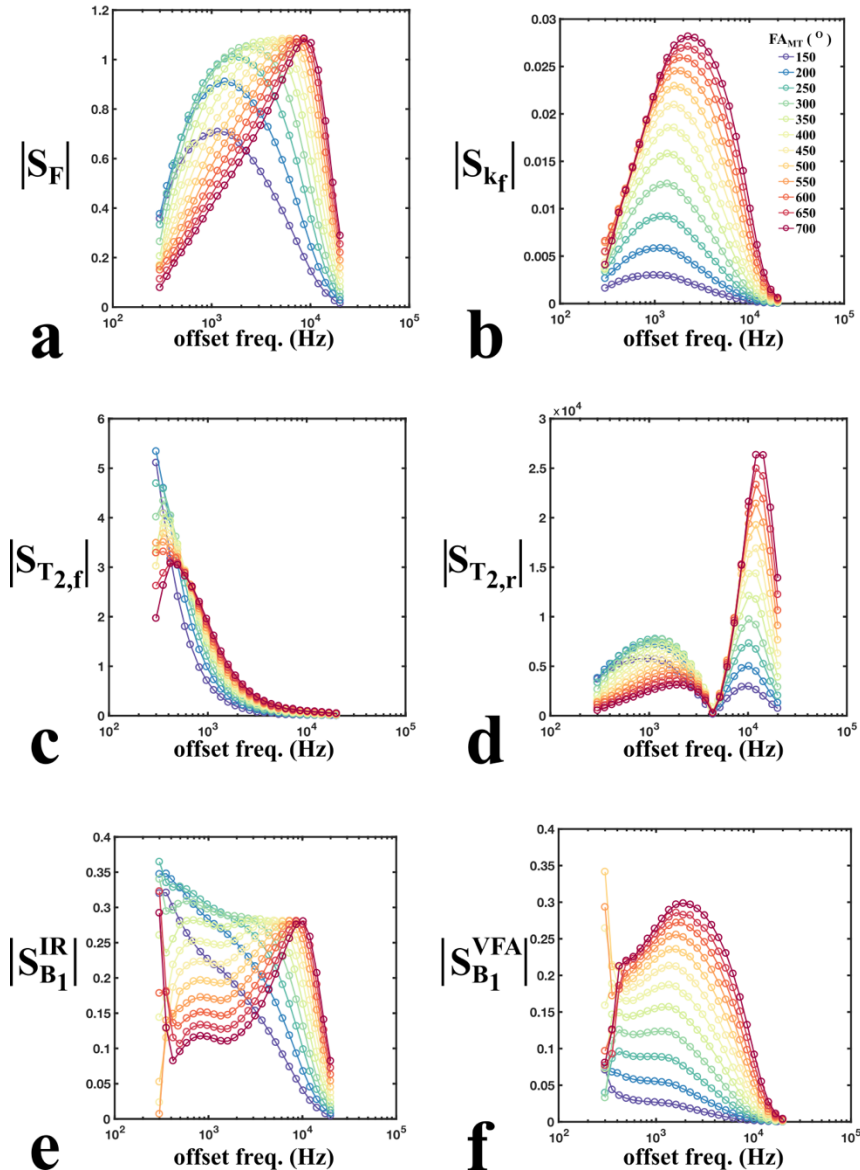


Figure 5-3. Sensitivity values (magnitudes) for each qMT fitting parameters (F , k_f , $T_{2,f}$, $T_{2,r}$) and B_1 measurement values considering a B_1 -independent T_1 measure (IR – inversion recovery) and a B_1 -dependent T_1 measure (VFA – variable flip angle). The 312-point protocol shown (12 flip angles \times 26 offset frequencies) represents the initial search-space used for protocol optimization. The sets of sensitivity values for each fitting parameter (a-d) consists of the matrix columns of the Jacobian sensitivity matrix (S_p in Eqs. (5-2) and (5-5)).

The optimal variance-efficiency and ΔF values (for $\Delta B_1 = 5\%$) calculated at each iteration of the optimization algorithm using the 312-point initial search-space are shown in Figure 5-4 for a wide range of regularization parameter (λ) values. The highest-valued variance-efficiency curve occurs for $\lambda=0$ (i.e. unregularized parameter-normalized CRLB) and $\lambda = 0.01$. For these values, the magnitude of ΔF steadily increased to 1% as the protocol was iteratively reduced to ~ 150 acquisition points, and then proceeded to decrease to $\sim 0.5\%$ for $N < 25$. Increasing the regularization parameter by an order of magnitude ($\lambda = 0.1$) substantially reduced ΔF values for $N > 25$ by up to a factor of two, while keeping the variance-efficiency relatively unaffected. However, for this case, ΔF returned to $\sim -0.5\%$ abruptly for $N < 25$. A regularization parameter of 0.5 was the lowest value tested which succeeded in ΔF achieving values near 0% for small protocols; for $N = 10$, $\lambda = 0.5$ resulted in $\Delta F = -0.04\%$ compared to -0.53% for $\lambda = 0$, a factor of 13 in relative improvement of the B_1 -insensitivity of F . A small reduction in variance-efficiency accompanied the improvement of ΔF for $\lambda = 0.5$; for $N=10$, the variance-efficiency decreased by 6.3% for $\lambda = 0.5$ relative to $\lambda = 0$. For higher λ values, the regularization term in Eq. (5-5) dominated early in the iterative optimization at the cost of lower variance-efficiencies, which never recover to their unregularized values. For intermediately-high λ values ($\lambda = 1, 2$), a second region where the regularization term in Eq. (5-5) dominates the iterative optimization can be seen near $N = 60$ and 120 respectively, substantially reducing the variance-efficiency. Overall, a λ value of 0.5 showed the best compromise between decreasing ΔF (insensitivity of F against B_1 errors) and maximizing variance-efficiency.

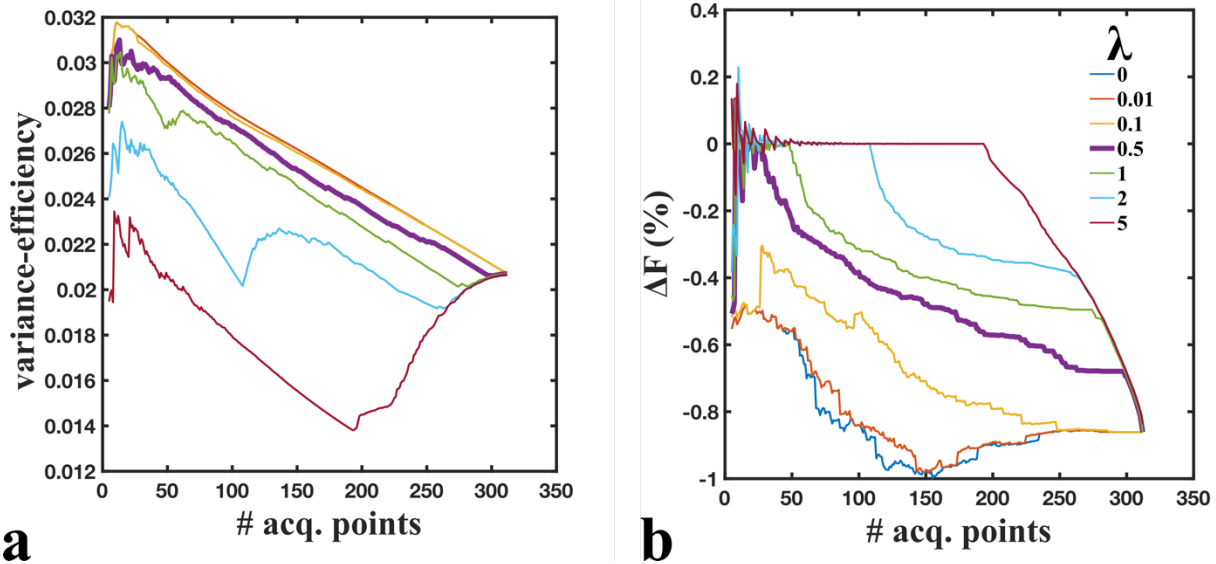


Figure 5-4. Variance-efficiency (a) and ΔF (b) (Eq. (5-2), $\Delta B_1 = 5\%$) values during the iterative optimization of the sensitivity-regularized Cramér-Rao lower bound equation (Eq. (5-5)). Variance-efficiency is defined here as $(\text{variance} \times \# \text{ acq. points})^{-1/2}$, where the variance is interpreted to be the parameter-normalized Cramér-Rao lower bound (V , Eq. (5-3)).

The 10-point protocols optimized using $\lambda = 0$ (CRLB) and $\lambda = 0.5$ (CRLB $_{\lambda=0.5}$) are shown in Figure 5-5, overlaid on the 312-point protocol search-space (displayed as line plots for better visibility of the optimized protocols). The details of these protocols are listed in Table 5-2. Overall, both optimized protocols share 7 out of 10 (Δ , FA_{MT}) pairs, with only three acquisition points changing if the regularization term is included in Eq. (5-5) ($\lambda = 0.5$). Both protocols have coverage of low, medium, and high off-resonance values, as well as low and high FA_{MT} values.

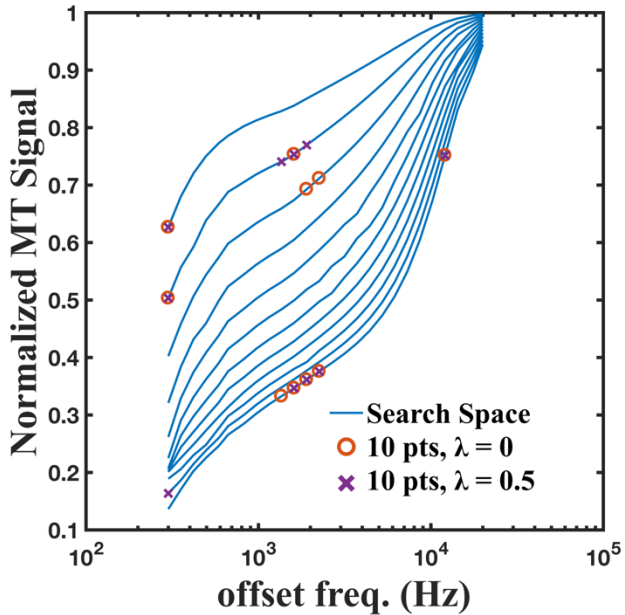
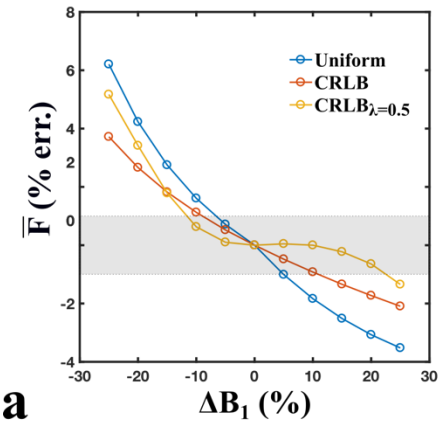


Figure 5-5. Comparison between the 10-point protocols iteratively optimized from a 312-point search space using solely the parameter-normalized CRLB ($\lambda = 0$) and regularized CRLB $_{\lambda=0.5}$. The different flip angle Z-spectrums of the initial optimization search-space are displayed in blue to emphasize the 10-point protocols. The flip angle Z-spectrums (150° to 700°, in 50° increments) range from the highest MT-signal values curve (150°) to lowest (700°).

5.6.3 Monte Carlo Simulations

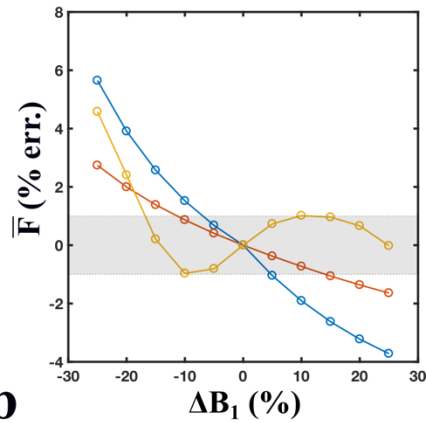
Distributions statistics (mean, σ) of the Monte Carlo simulations of the fitted parameter-of-interest F are shown for a range of ΔB_1 values (SNR = 100) in Figure 5-6 and a range of SNR values ($\Delta B_1 = 0$ and 15 %) in Figure 5-7, for the three protocols listed in Table 5-2. Figure 5-6a and b displays the difference (%) in mean F relative to the mean F value for the $\Delta B_1 = 0$ case, whereas Figure 5-7a and b displays the difference (%) in mean F relative to the ideal (noiseless) fitted F value.

White Matter

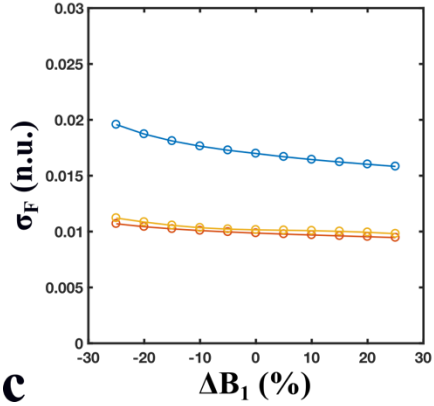


a

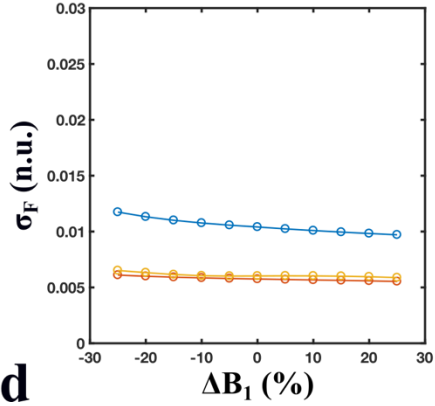
Grey Matter



b



c



d

Figure 5-6. Means (a, b) and standard deviations (c, d) of the distribution of pool-size ratios (F) for sets of Monte Carlo simulations (10,000 runs, SNR = 100) fitted using a range of B_1 errors ($\Delta B_1 = \pm 30\%$, $B_1 = 1$ n.u.) and for two sets of qMT parameters (white matter – a,c; grey matter – b, d). Mean F values (% error) shown here were compared relative to the accurate B_1 value case ($\Delta B_1 = 0$), and the grey region represents the region of $\pm 1\%$ relative error. Simulated signal values were generated and fitted for three different 10-point qMT protocols: Uniform (blue) – two-FA protocol with logarithmically-uniform off-resonance frequency values, CRLB (red) – protocol optimized by iteratively minimizing the increase in the parameter-normalized Cramér-Rao lower bound of the system, and $CRLB_{\lambda=0.5}$ (yellow) – protocol optimized similar to CRLB, regularized by the estimated error of F (ΔF) in the presence of a B_1 error (Eq. (5-5)).

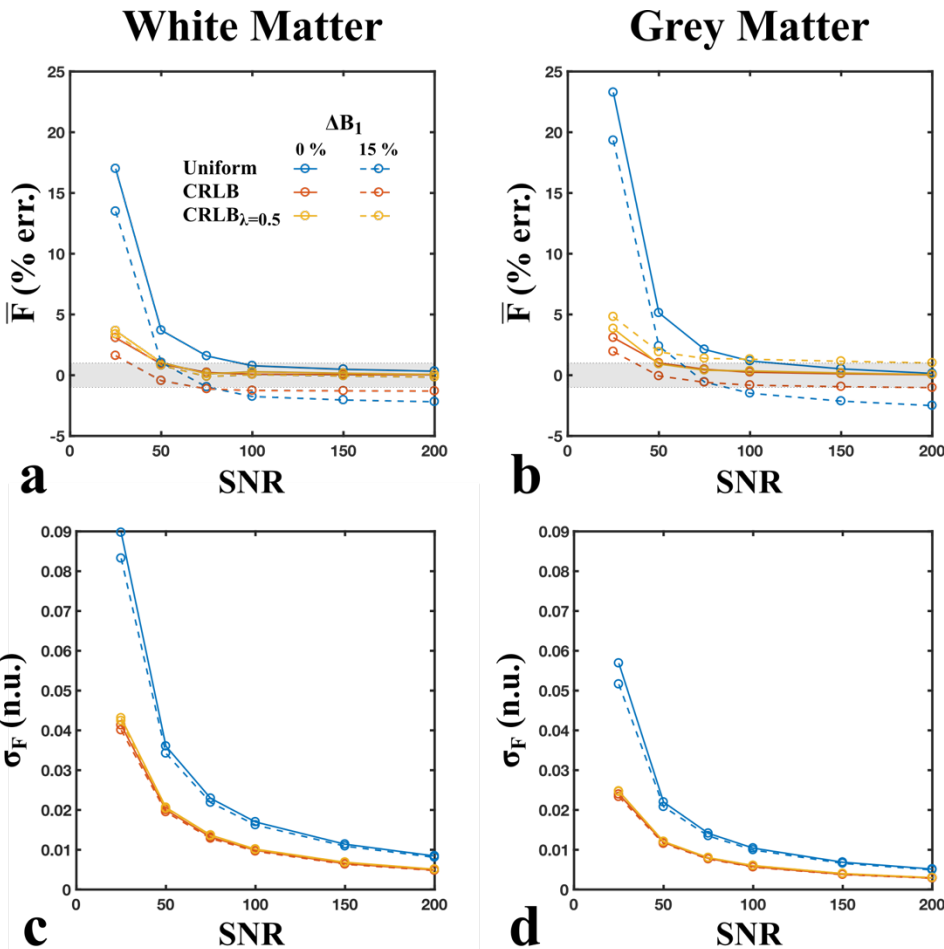


Figure 5-7. Means (a, b) and standard deviations (c, d) of the distribution of pool-size ratio values (F) for sets of Monte Carlo simulations (10,000 runs) fitted using a range of SNR values (25, 50, 75, 100, 150, and 200) and for two sets of qMT parameters (white matter – a,c; grey matter – b, d). Mean F values (% error) shown here were compared relative to data fitted for an ideal SNR case (noiseless), and the grey region represents the region of $\pm 1\%$ relative error. Data was fitted assuming ideal B_1 values ($B_1 = 1$ n.u., solid lines) and a 15% overestimation in B_1 ($B_1 = 1.15$ n.u., dotted lines). Simulated signal values were generated and fitted for three different 10-point qMT protocols: Uniform (blue) – two-FA protocol with logarithmically-uniform off-resonance frequency values, CRLB (red) – protocol optimized by iteratively minimizing the increase in the parameter-normalized Cramér-Rao lower bound of the system, CRLB $_{\lambda=0.5}$ (yellow) – protocol optimized similar to CRLB, regularized by the estimated error of F (ΔF) in the presence of a B_1 error (Eq. (5-5)).

For the CRLB $_{\lambda=0.5}$ protocol, $|\Delta \bar{F}|$ values were less than 1% (grey area) for ΔB_1 between -10% and 20% (Figure 5-6, for both WM and GM). The same was true for ΔB_1 between -5% and 10% for the CRLB protocol, and between -5% and 5% for the Uniform protocol. CRLB and CRLB $_{\lambda=0.5}$ protocols resulted in standard deviations of fitted F substantially lower (by a factor of ~ 1.75) than

the Uniform protocol. Although $\text{CRLB}_{\lambda=0.5} \sigma_F$ values were slightly different than the CRLB values (6.7% higher), both curves nearly overlapped for all ΔB_1 values.

In the absence of B_1 errors ($\Delta B_1 = 0$), $|\Delta \bar{F}|$ values for both optimized protocols (CRLB and $\text{CRLB}_{\lambda=0.5}$) were below 1% for datasets with SNR values greater than 75 (Figure 5-7, WM and GM). The Uniform protocol needed a minimum SNR of 100 to result in $|\Delta \bar{F}|$ values below 1%. In the presence of a 15% overestimation of B_1 , the $|\Delta \bar{F}|$ vs. SNR curve for $\text{CRLB}_{\lambda=0.5}$ remained largely unchanged for WM. For GM, the $|\Delta \bar{F}|$ values for $\text{CRLB}_{\lambda=0.5}$ resulted in slight increase, although remained within 1% for $\text{SNR} > 100$. In contrast, even at high SNR values (>100), $|\Delta \bar{F}|$ values for the CRLB and Uniform protocols resulted in greater bias ($>1\%$) for the $\Delta B_1 = 15\%$ case. The σ_F curves increased rapidly for SNR values lower than 75 for all protocols. For all cases, σ_F did not vary substantially between both ΔB_1 values evaluated (0% and 15%). For CRLB and $\text{CRLB}_{\lambda=0.5}$, no substantial differences in their σ_F vs. SNR curves were observed, and both had lower standard deviations relative to the Uniform protocol.

5.7 Discussion

This work describes a qMT protocol optimization methodology for reduced B_1 -sensitivity of the pool-size ratio F by regularizing the CRLB with a first-order sensitivity analysis. Using Monte Carlo simulations we found that, for a protocol optimized using regularized $\text{CRLB}_{\lambda=0.5}$, errors propagated to fitted F were below 1% for B_1 -errors ranging between -10 and 20%, consistent with the B_1 values typically observed in the human brain at 3T [203]. Both regularized and conventional CRLB optimization resulted in an improvement of pool-size ratio B_1 -insensitivity relative to a two-FA_{MT} uniform protocol. Sensitivity analyses of uniform protocols suggested that, if using VFA T_1 mapping, acquiring data at both small and large MT flip angle acquisitions (at mid and

high off-resonance frequencies) may be an important contributing factor in designing a B_1 -insensitive acquisition protocol, where F likely has a higher robustness against B_1 errors. These simulations demonstrate for a range of SNRs, B_1 -inaccuracies, and brain tissues, the effectiveness of a regularized approach of designing qMT for B_1 -insensitivity. This work suggests that if the pool-size ratio is the primary parameter-of-interest, it may be possible to design a qMT protocol robust enough to omit B_1 map acquisition altogether, without substantially biasing estimates of F .

Our study considered a specific qMT fitting model (Sled and Pike[145]) that fitted quantitative MT data for four parameters of the Bloch-McConnell equations ($F, k_f, T_{2,f}, T_{2,r}$). Several other qMT fitting models for MT-prepared SPGR data exist, such as Yarnykh's model [151], which neglects direct saturation effects, and Ramani's continuous wave power equivalent model [150]. Each qMT fitting model makes different approximations or assumptions, and differ in fitting parameters. For example, Yarnykh's model suggests acquiring data only at off-resonance frequencies greater than 1 kHz, and has a different set of fitting parameters (e.g. $T_{2,f}$ is neglected and their pool-size ratio parameter is defined as $f = M_{0,r} / (1 + M_{0,r})$, instead of Sled and Pike's $F = M_{0,r} / M_{0,f}$ parameter). The different range in off-resonance frequencies will reduce the available Jacobian sensitivity values during optimization, which may impact the optimization against auxiliary measurements (e.g. B_1) errors. Different sets of fitting parameters between models could also change the fitting behavior in the presence of B_1 -error propagation, even if the same SPGR qMT acquisition protocols are used. The single-point qMT fitting model [75,198] may provide additional challenges for optimizing against auxiliary measurement error-sensitivity. This fitting model imposes several fitting parameter restraints, which would provide additional limitations when solving Eq. (5-2). The analysis of uniform protocols and Jacobian sensitivity matrices also suggests that B_1 -insensitivity of F may be a result of including both small and large MT flip angle acquisitions in a

protocol at mid and high off-resonance frequencies, a configuration that cannot be done using single-point measurement protocol.

We proposed a regularization approach to add an auxiliary measurement (e.g. B_1) error-sensitivity component to the CRLB in our optimization algorithm. An alternative approach could have been to do a formal statistical analysis of the error propagation using the CRLB instead as the optimization algorithm condition. Lankford and Does [204] recently presented such a treatment and applied it to study T_2 mapping. Their statistical analysis of the error propagation from parameter constraints demonstrated that, under certain practical circumstances, it can be beneficial (in terms of variance and full mean-squared error of fitted T_2) to include a B_1 measurement for multi-echo T_2 mapping. Their framework was presented to be generalizable to other quantitative techniques that require auxiliary measurements such as qMT; however, their analysis was only developed for a single-level of parameter constraints. Although this may be applicable for a B_1 -error propagation analysis of qMT when using a B_1 -independent T_1 mapping method (e.g. IR), a B_1 -dependent T_1 mapping method (e.g. VFA) complicates the error propagation analysis beyond what is presented in Lankford and Does, as there are two interacting constraints within the qMT model (e.g. $qMT(B_1, T_1(B_1))$). In contrast, one benefit of the sensitivity-regularization approach we presented here is its conceptual simplicity and ease of implementation for optimization applications, particularly for this case. Nonetheless, a formal propagation of error analysis would likely be a good choice moving forward to compare the sensitivity to errors in constraints between different qMT fitting models, as discussed above.

Several limitations should be considered when interpreting this work. An iterative optimization approach was chosen to estimate optimal acquisition protocols from a larger initial search space, however this approach is not guaranteed to result in the global minima of the optimization

condition. Global optimization using simulated annealing [164] could have been another valid approach to optimize our qMT protocol using Eq. (5-5). However, iterative optimization approaches benefit from an ease of implementation, rapid computation, and the flexibility to choose the number of measurements in the protocol after the optimization is complete. In contrast, simulated annealing approaches optimize for a fixed pre-determined number of protocol points. We also opted for Monte Carlo simulations instead of an *in vivo* study to validate the regularized approach to B_1 -sensitivity protocol optimization. This gave us the flexibility to accurately know and control the system conditions (e.g. tissue values, B_1 error values, and noise level). *In vivo* evidence of the benefits of qMT protocol optimization using CRLB has already been reported in several studies [164,165,201]. In addition, Eqs. (5-1) and (5-2) (used to establish the regularization term) were developed from a recent comprehensive B_1 -sensitivity analysis of qMT study [202] that compared and validated simulations with *in vivo* measurements of F in the absence of B_1 maps (for a uniform protocol). Lastly, the optimization algorithm investigated here only considered a single tissue type (WM) during the protocol optimization procedure. Although the resulting protocol was also evaluated for another tissue type in the Monte Carlo simulations (GM) and both were restricted to errors below 1%, even though the B_1 -sensitivity of F in GM varied more than for WM. If desired, the optimization condition (Eq. (5-5)) could be adapted to consider multiple tissue types in a similar manner as proposed by Cercignani et al [164], by instead minimizing for the tissue which results in the maximum value of Eq. (5-5) at each iteration.

Overall, this work presents a framework for designing qMT acquisition protocols optimized for robustness against inaccuracies of auxiliary measurements (e.g. B_1) by regularizing the Cramér-Rao lower bound with fitting parameter-sensitivity information. We demonstrated this methodology by optimizing a qMT protocol for robustness of the pool-size ratio (F) against B_1 -

inaccuracies, and studied simulations using this protocol for a wide range of signal-to-noise ratios, B_1 -inaccuracies, and tissue types. These findings imply that B_1 mapping possibly be omitted from such a qMT optimized acquisition protocol with minimal impact to the fitted pool-size ratio ($< 1\%$ error). Potential future work may include optimizing protocols for reduced sensitivity of other or multiple auxiliary measurements, and compare this optimization between other qMT fitting models. Another interesting approach could be to combine Z-spectrum compressed sensing [205] with this optimization technique, to maximize the auxiliary measurement insensitivity by increasing the number of measurements while reducing the total acquisition time.

Chapter 6

Conclusion

6.1 Summary

Quantitative magnetization transfer imaging is an important quantitative MRI technique to investigate de- and remyelination in multiple sclerosis, and is a promising technique for studying remyelination during the development of therapeutics that promote remyelination. However, qMT is dependent on a number of other quantitative MRI techniques, and imperfections in these measurements can affect the estimates of fitted qMT parameters, potentially biasing the myelin density estimates in the brain. This situation is further complicated if the calibration measurements required for qMT also depend on each other, as can be the case for some T_1 mapping techniques that also require B_1 calibration. This thesis investigated how to achieve robust qMT imaging estimation of the pool-size ratio (a myelin biomarker) in the presence of transmit radiofrequency field (B_1) inhomogeneities and/or inaccuracies. In Chapter 3, several whole-brain B_1 mapping techniques were compared in addition to VFA T_1 maps calibrated with them, and several potential sources of B_1 inaccuracies were identified. In Chapter 4, the B_1 -sensitivity of the qMT pool-size ratio was investigated for different T_1 mapping methods (B_1 -dependent and B_1 -independent) with a fixed qMT acquisition protocol (“uniform”), and VFA T_1 mapping was discovered to result in a substantially lower sensitivity of the pool-size ratio to B_1 -inaccuracies. In Chapter 5, a regularized-optimization approach for the qMT acquisition protocol to reduce the sensitivity of the pool-size ratio to B_1 -inaccuracies was presented, and Monte Carlo simulations demonstrated robustness of the pool-size ratio estimation for a wide range of conditions (SNR, B_1 -inaccuracies, tissues) relative to two other qMT acquisition protocols (“Uniform” and non-regularized optimization).

B₁ Maps for Quantitative T₁

Chapter 3 compared B₁ maps measured using the double angle method with a standard MRI pulse sequence (EPI) with two other widely-established whole-brain B₁ mapping techniques (AFI, BS), in addition to their resulting T₁ maps, using the VFA technique. The results from this work demonstrate that, for researchers without access to advanced B₁ mapping techniques on their scanners or without the ability to implement them using pulse sequence programming, B₁ mapping using double angle EPI with standard pulse sequences may be a sufficient alternative to rapidly measure good quality whole-brain B₁ maps, particularly for VFA T₁ mapping applications. In addition, this chapter reported local variabilities in B₁ values between different mapping techniques, and established that B₁-inaccuracies is likely unavoidable and should be expected in the current state of quantitative MRI. Sources of B₁-measurement inaccuracies range from noise to large-scale artifacts.

B₁-Sensitivity Analysis of qMT

Having established several probable sources of B₁ measurement inaccuracies and investigated the relationship between VFA T₁ and B₁, Chapter 4 sought to explore the sensitivity of qMT to B₁-inaccuracies for two categories of T₁ mapping techniques: B₁-independent techniques (e.g. inversion recovery) and B₁-dependent techniques (e.g. variable flip angle). Using simulations, and then validating these results with *in vivo* measurements, this work demonstrated a substantial reduction in B₁-sensitivity of the pool-size ratio if VFA (a B₁-dependent T₁ mapping technique) is used instead of a B₁-independent technique, like IR. The robustness we observed is so strong for this case, the results suggest it may be possible to acquire qMT without a B₁ map at all, without substantially biasing the pool-size ratio estimates in white matter. Driven by the desire for whole brain qMT, there has been a transition within the qMT field during the past decade from using

single-slice B_1 -independent T_1 techniques, such as IR, to whole-brain VFA T_1 mapping. However, with the advent of new whole-brain T_1 mapping sequences that are becoming widely available on clinical scanners (e.g. MP2RAGE, a B_1 -independent technique) some researchers may make the seemingly logical switch back to B_1 -independent T_1 mapping techniques in their qMT protocols. While the results from this work should not automatically discourage researchers to use such techniques in their protocols, they should be mindful of the consequences that this choice can have on their pool-size ratio estimates if their B_1 map contains potential inaccuracies, such as artifacts.

B_1 -Sensitivity Regularization of the CRLB for qMT Optimization

Building on the promising results of the previous chapter, the aim of Chapter 5 was to minimize the B_1 -sensitivity of qMT even further by optimizing the qMT acquisition protocol simultaneously for noise and B_1 -insensitivity. A regularization term for B_1 -sensitivity of qMT parameters was developed, and the regularization coefficient was optimized for the pool-size ratio parameter. Using Monte Carlo simulations, the sensitivity-regularized Cramér-Rao lower bound demonstrated better B_1 -insensitivity of the pool-size ratio (relative to two other optimized protocols: “Uniform” and unregularized Cramér-Rao lower bound) for a wide range of signal-to-noise values, B_1 -inaccuracies (typical range observed *in vivo* if a B_1 map is omitted) and tissue types (white matter and grey matter). This work describes a detailed methodology and framework for optimizing qMT protocols to be B_1 -insensitive, and the algorithms and code that were developed in this project have been released as an open-source package for other researchers to use.

6.2 Future Work

The work presented in this thesis investigated and optimized the B_1 -insensitivity of qMT model parameters for a subset of qMT acquisition pulse techniques (SPGR) and fitting models (Sled and Pike). There exist several other qMT fitting models for the SPGR qMT pulse sequence, such as Yarnykh's model [151], Ramani's model [150], and Yarnykh's single-point constrained qMT model [75,198]. It may be interesting to do a comparative B_1 -sensitivity study of these SPGR qMT fitting models. Such a study could follow the same sensitivity analysis and optimization framework presented in chapters 4 and 5, or use other statistical analysis approaches to study error-propagation, for example by adapting the theory recently proposed by Lankford et al. [204]. The benefit of the latter approach would be that, instead of investigating the B_1 -sensitivity for a single source of inaccuracy, the impact of the SNRs of the B_1 , T_1 , and individual MT-weighted measurements on the qMT fitting parameters' statistics could be explored in addition to local or systemic biases in B_1 . Alternative qMT pulse sequences also exist, such as Gloor's steady-state free precession approach, which requires both B_1 and T_1 maps, that could also be of interest to do a B_1 -sensitivity study for [190]. Comparison of our optimized approach with Dortch's selective inversion recovery method of acquiring qMT data, which has been shown to be B_1 (and B_0)-insensitive [191], would also be of interest.

Out of the three typical qMT calibration measurements (B_0 , B_1 , T_1), the qMT model parameters were only investigated for sensitivity due to B_1 -inaccuracies in this work. Performing sensitivity analyses for B_0 and T_1 would certainly also be of interest, although none of the other measurements are typically dependent on these, besides qMT (unlike for B_1 , which T_1 can often depends on). Although not thoroughly investigated, the impact of inaccurate T_1 on the pool-size ratio can be inferred via the simulations in Figure 4-2, which suggest that overestimations in T_1 values will

lower the estimated pool-size ratio values. We reported preliminary results demonstrating this relationship *in vivo* at a previous conference (Boudreau et al. 2013, endMS Conference, see Other Publications section). In humans, there can be a large variation in T_1 values estimated by different T_1 mapping methods (e.g. ± 100 ms) relative to inversion recovery (gold standard). We have previously reported this range of systemic bias in T_1 mapping pulse sequences (Stikov et al. 2015 [56], see Other Publications section). Using simulations, we proposed that the ~ 100 ms overestimation in VFA T_1 (relative to IR) observed by some groups may be due to only partial spoiling of the transverse magnetization in the steady-state pulse sequence. A recent paper proposes a correction to account for the unspoiled magnetization effect in VFA [206], which results in a reduction in T_1 estimation relative to the uncorrected values. Another potential avenue of investigation could be simultaneously optimizing for reduced sensitivity of all three calibration measurements by adding B_0 and T_1 terms in Eq. (5-5), each with unique regularization parameters. For this, it may be needed include additional pulse sequence optimization parameters, such as the repetition time, the excitation flip angle, and the echo time.

One of the major challenges of qMT is its conventionally long acquisition times, largely limiting it to research applications and rarely included in clinical studies. Although omitting the B_1 map from the qMT acquisition protocol would reduce the acquisition time of the overall protocol, that alone will not reduce it enough to acquire high-resolution (1 mm^3) whole-brain qMT data in a clinically feasible time (5-10 minutes). Other groups have proposed different approaches to measuring qMT parameters maps rapidly, such as constraining the relationships between fitting parameters and reducing the number of qMT measurements [75,198] in addition to using fast k-space readout techniques, such as EPI [201,207]. Another potential largely unexplored technique for accelerating qMT is compressed sensing [166,167], a nonlinear image reconstruction technique

for sparse datasets by randomly acquiring a subset of k-space data. In recent years, there's been a rapid growth in the use of compressed sensing by the MRI community, having applications in quantitative MRI techniques such as diffusion spectrum imaging [208], quantitative T₁ and T₂ mapping [209-211], and chemical exchange saturation transfer (CEST) imaging [212,213] (an MT-based spectroscopy technique). Several of these compressed sensing approaches could also be well-suited for qMT, such as low-rank constraints and orthogonal matching pursuit, which takes advantage of data information redundancy in the parameter domain to further accelerate the acquisition measurements. Our group has recently reported a preliminary study at an international conference, which I co-authored (McLean et al. 2017, see Other Publications section), that explored the compressed sensing acceleration potential of the Z-spectrum [205]. The accelerated acquisition time could be used either for shorter scan times, or to measure an increased number of qMT protocol points. An example application of the latter case would be to acquire an increased number of points for better B₁-insensitivity of qMT or lower Cramér-Rao lower bound (e.g. see Figure 5-4). Lastly, MR Fingerprinting is an emerging MRI technique that has shown promise in simultaneously acquiring several quantitative MRI parameters (e.g. T₁, T₂, B₀) using pseudo-random pulse sequence parameters during the k-space acquisitions, and models the images using a pre-computed dictionary of signal values for a large range of qMRI parameters [214]. A recent paper proposed a quantitative CEST MRI Fingerprinting acquisition [215], suggesting it may be possible to also explore implementations of quantitative MT using this technique.

Bibliography

1. Nishimura DG. Principles of Magnetic Resonance Imaging: Lulu.com; 2010.
2. Haacke EM. Magnetic resonance imaging : physical principles and sequence design. New York: Wiley-Liss; 1999.
3. Bernstein MA, King KF, Zhou XJ. Handbook of MRI Pulse Sequences. Burlington: Academic Press; 2004.
4. Browne P, Chandraratna D, Angood C, Tremlett H, Baker C, Taylor BV, Thompson AJ. Atlas of Multiple Sclerosis 2013: A growing global problem with widespread inequity. *Neurology* 2014;83(11):1022-1024.
5. StatisticsCanada. Table 105-1300 - Neurological conditions, by age group and sex, household population aged 0 and over, 2010/2011, occasional (number unless otherwise noted). CANSIM (database) (accessed: 2017/11/01)
6. Orton SM, Herrera BM, Yee IM, Valdar W, Ramagopalan SV, Sadovnick AD, Ebers GC, Canadian Collaborative Study G. Sex ratio of multiple sclerosis in Canada: a longitudinal study. *Lancet Neurol* 2006;5(11):932-936.
7. Belbasis L, Bellou V, Evangelou E, Ioannidis JP, Tzoulaki I. Environmental risk factors and multiple sclerosis: an umbrella review of systematic reviews and meta-analyses. *Lancet Neurol* 2015;14(3):263-273.
8. Leray E, Moreau T, Fromont A, Edan G. Epidemiology of multiple sclerosis. *Rev Neurol (Paris)* 2016;172(1):3-13.
9. Ebers GC. Environmental factors and multiple sclerosis. *Lancet Neurol* 2008;7(3):268-277.
10. Acheson ED, Bachrach CA, Wright FM. Some Comments on the Relationship of the Distribution of Multiple Sclerosis to Latitude, Solar Radiation, and Other Variables. *Acta Psychiatrica Scandinavica* 1960;35(S147):132-147.
11. Willer CJ, Dyment DA, Sadovnick AD, Rothwell PM, Murray TJ, Ebers GC, Canadian Collaborative Study G. Timing of birth and risk of multiple sclerosis: population based study. *BMJ* 2005;330(7483):120.
12. Simpson S, Jr., Blizzard L, Otahal P, Van der Mei I, Taylor B. Latitude is significantly associated with the prevalence of multiple sclerosis: a meta-analysis. *Journal of Neurology, Neurosurgery & Psychiatry* 2011;82(10):1132-1141.

13. Willer CJ, Dyment DA, Risch NJ, Sadovnick AD, Ebers GC, Canadian Collaborative Study G. Twin concordance and sibling recurrence rates in multiple sclerosis. *Proc Natl Acad Sci U S A* 2003;100(22):12877-12882.
14. Cossburn M, Ingram G, Hirst C, Ben-Shlomo Y, Pickersgill T, Robertson N. Age at onset as a determinant of presenting phenotype and initial relapse recovery in multiple sclerosis. *Multiple Sclerosis Journal* 2012;18(1):45-54.
15. DeLuca GC, Yates RL, Beale H, Morrow SA. Cognitive Impairment in Multiple Sclerosis: Clinical, Radiologic and Pathologic Insights. *Brain Pathology* 2015;25(1):79-98.
16. Galea I, Ward-Abel N, Heesen C. Relapse in multiple sclerosis. *BMJ : British Medical Journal* 2015;350.
17. Naldi P, Collimedaglia L, Vecchio D, Rosso MG, Perl F, Stecco A, Monaco F, Leone MA. Predictors of attack severity and duration in multiple sclerosis: a prospective study. *Open Neurol J* 2011;5:75-82.
18. Saguil A, Kane S, Farnell E. Multiple sclerosis: a primary care perspective. *Am Fam Physician* 2014;90(9):644-652.
19. Atkins HL, Bowman M, Allan D, Anstee G, Arnold DL, Bar-Or A, Bence-Bruckler I, Birch P, Bredeson C, Chen J, Fergusson D, Halpenny M, Hamelin L, Huebsch L, Hutton B, Laneuville P, Lapierre Y, Lee H, Martin L, McDiarmid S, O'Connor P, Ramsay T, Sabloff M, Walker L, Freedman MS. Immunoablation and autologous haemopoietic stem-cell transplantation for aggressive multiple sclerosis: a multicentre single-group phase 2 trial. *Lancet* 2016;388(10044):576-585.
20. Deshmukh VA, Tardif V, Lyssiotis CA, Green CC, Kerman B, Kim HJ, Padmanabhan K, Swoboda JG, Ahmad I, Kondo T, Gage FH, Theofilopoulos AN, Lawson BR, Schultz PG, Lairson LL. A regenerative approach to the treatment of multiple sclerosis. *Nature* 2013;502(7471):327-332.
21. Harlow DE, Honce JM, Miravalle AA. Remyelination Therapy in Multiple Sclerosis. *Front Neurol* 2015;6:257.
22. Brown RA, Narayanan S, Arnold DL. Imaging of repeated episodes of demyelination and remyelination in multiple sclerosis. *Neuroimage Clin* 2014;6:20-25.
23. McFarland HF, Martin R. Multiple sclerosis: a complicated picture of autoimmunity. *Nat Immunol* 2007;8(9):913-919.
24. Perry VH. 17 - Inflammation and Axon Degeneration. In: Waxman SG, editor. *Multiple Sclerosis As A Neuronal Disease*. Burlington: Academic Press; 2005. p 241-253.
25. Lucchinetti C, Brück W, Parisi J, Scheithauer B, Rodriguez M, Lassmann H. A quantitative analysis of oligodendrocytes in multiple sclerosis lesionsA study of 113 cases. *Brain* 1999;122(12):2279-2295.

26. Geurts JJ, Barkhof F. Grey matter pathology in multiple sclerosis. *Lancet Neurol* 2008;7(9):841-851.
27. Peterson JW, Bo L, Mork S, Chang A, Trapp BD. Transected neurites, apoptotic neurons, and reduced inflammation in cortical multiple sclerosis lesions. *Annals of Neurology* 2001;50(3):389-400.
28. McDonald WI, Compston A, Edan G, Goodkin D, Hartung HP, Lublin FD, McFarland HF, Paty DW, Polman CH, Reingold SC, Sandberg-Wollheim M, Sibley W, Thompson A, van den Noort S, Weinshenker BY, Wolinsky JS. Recommended diagnostic criteria for multiple sclerosis: guidelines from the International Panel on the diagnosis of multiple sclerosis. *Ann Neurol* 2001;50(1):121-127.
29. Polman CH, Reingold SC, Edan G, Filippi M, Hartung HP, Kappos L, Lublin FD, Metz LM, McFarland HF, O'Connor PW, Sandberg-Wollheim M, Thompson AJ, Weinshenker BG, Wolinsky JS. Diagnostic criteria for multiple sclerosis: 2005 revisions to the "McDonald Criteria". *Ann Neurol* 2005;58(6):840-846.
30. Polman CH, Reingold SC, Banwell B, Clanet M, Cohen JA, Filippi M, Fujihara K, Havrdova E, Hutchinson M, Kappos L, Lublin FD, Montalban X, O'Connor P, Sandberg-Wollheim M, Thompson AJ, Waubant E, Weinshenker B, Wolinsky JS. Diagnostic criteria for multiple sclerosis: 2010 revisions to the McDonald criteria. *Annals of Neurology* 2011;69(2):292-302.
31. Filippi M, Rocca MA, Ciccarelli O, De Stefano N, Evangelou N, Kappos L, Rovira A, Sastre-Garriga J, Tintore M, Frederiksen JL, Gasperini C, Palace J, Reich DS, Banwell B, Montalban X, Barkhof F, Group MS. MRI criteria for the diagnosis of multiple sclerosis: MAGNIMS consensus guidelines. *Lancet Neurol* 2016;15(3):292-303.
32. Vellinga MM, Geurts JJ, Rostrup E, Uitdehaag BM, Polman CH, Barkhof F, Vrenken H. Clinical correlations of brain lesion distribution in multiple sclerosis. *J Magn Reson Imaging* 2009;29(4):768-773.
33. Miller DH, Filippi M, Fazekas F, Frederiksen JL, Matthews PM, Montalban X, Polman CH. Role of magnetic resonance imaging within diagnostic criteria for multiple sclerosis. *Ann Neurol* 2004;56(2):273-278.
34. Anderson VM, Fox NC, Miller DH. Magnetic resonance imaging measures of brain atrophy in multiple sclerosis. *Journal of Magnetic Resonance Imaging* 2006;23(5):605-618.
35. Dalton CM, Brex PA, Jenkins R, Fox NC, Miszkiel KA, Crum WR, O'Riordan JI, Plant GT, Thompson AJ, Miller DH. Progressive ventricular enlargement in patients with clinically isolated syndromes is associated with the early development of multiple sclerosis. *Journal of Neurology, Neurosurgery & Psychiatry* 2002;73(2):141-147.
36. De Stefano N, Battaglini M, Smith SM. Measuring Brain Atrophy in Multiple Sclerosis. *Journal of Neuroimaging* 2007;17:10S-15S.

37. Horsfield MA, Rovaris M, Rocca MA, Rossi P, Benedict RHB, Filippi M, Bakshi R. Whole-brain atrophy in multiple sclerosis measured by two segmentation processes from various MRI sequences. *Journal of the Neurological Sciences* 2003;216(1):169-177.
38. Laule C, Vavasour IM, Whittall KP, Oger J, Paty DW, Li DK, MacKay AL, Arnold DL. Evolution of focal and diffuse magnetisation transfer abnormalities in multiple sclerosis. *J Neurol* 2003;250(8):924-931.
39. Rovaris M, Gass A, Bammer R, Hickman SJ, Ciccarelli O, Miller DH, Filippi M. Diffusion MRI in multiple sclerosis. *Neurology* 2005;65(10):1526-1532.
40. Schmierer K, Wheeler-Kingshott CAM, Boulby PA, Scaravilli F, Altmann DR, Barker GJ, Tofts PS, Miller DH. Diffusion tensor imaging of post mortem multiple sclerosis brain. *NeuroImage* 2007;35(2):467-477.
41. Schmierer K, Scaravilli F, Altmann DR, Barker GJ, Miller DH. Magnetization transfer ratio and myelin in postmortem multiple sclerosis brain. *Annals of Neurology* 2004;56(3):407-415.
42. Schmierer K, Tozer DJ, Scaravilli F, Altmann DR, Barker GJ, Tofts PS, Miller DH. Quantitative magnetization transfer imaging in postmortem multiple sclerosis brain. *J Magn Reson Imaging* 2007;26(1):41-51.
43. Loitfelder M, Fazekas F, Petrovic K, Fuchs S, Ropele S, Wallner-Blazek M, Jehna M, Aspeck E, Khalil M, Schmidt R, Neuper C, Enzinger C. Reorganization in cognitive networks with progression of multiple sclerosis: Insights from fMRI. *Neurology* 2011;76(6):526-533.
44. Rocca MA, Colombo B, Falini A, Ghezzi A, Martinelli V, Scotti G, Comi G, Filippi M. Cortical adaptation in patients with MS: a cross-sectional functional MRI study of disease phenotypes. *The Lancet Neurology* 2005;4(10):618-626.
45. Schmierer K, Thavarajah JR, An SF, Brandner S, Miller DH, Tozer DJ. Effects of formalin fixation on magnetic resonance indices in multiple sclerosis cortical gray matter. *J Magn Reson Imaging* 2010;32(5):1054-1060.
46. Chen JTH, Easley K, Schneider C, Nakamura K, Kidd GJ, Chang A, Staugaitis SM, Fox RJ, Fisher E, Arnold DL, Trapp BD. Clinically feasible MTR is sensitive to cortical demyelination in MS. *Neurology* 2013;80(3):246-252.
47. Derakhshan M, Caramanos Z, Giacomini PS, Narayanan S, Maranzano J, Francis SJ, Arnold DL, Collins DL. Evaluation of automated techniques for the quantification of grey matter atrophy in patients with multiple sclerosis. *NeuroImage* 2010;52(4):1261-1267.
48. Derakhshan M, Caramanos Z, Narayanan S, Arnold DL, Louis Collins D. Surface-based analysis reveals regions of reduced cortical magnetization transfer ratio in patients with multiple sclerosis: A proposed method for imaging subpial demyelination. *Human Brain Mapping* 2014;35(7):3402-3413.

49. Rudko DA, Derakhshan M, Maranzano J, Nakamura K, Arnold DL, Narayanan S. Delineation of cortical pathology in multiple sclerosis using multi-surface magnetization transfer ratio imaging. *Neuroimage Clin* 2016;12:858-868.
50. Narayanan A, Hartman JS, Bain AD. Characterizing Nonexponential Spin-Lattice Relaxation in Solid-State NMR by Fitting to the Stretched Exponential. *Journal of Magnetic Resonance, Series A* 1995;112(1):58-65.
51. Di Giovanni P, Azlan CA, Ahearn TS, Semple SI, Gilbert FJ, Redpath TW. The accuracy of pharmacokinetic parameter measurement in DCE-MRI of the breast at 3 T. *Physics in Medicine & Biology* 2010;55(1):121-132.
52. Yuan J, Chow SK, Yeung DK, Ahuja AT, King AD. Quantitative evaluation of dual-flip-angle T1 mapping on DCE-MRI kinetic parameter estimation in head and neck. *Quant Imaging Med Surg* 2012;2(4):245-253.
53. Drain LE. A Direct Method of Measuring Nuclear Spin-Lattice Relaxation Times. *Proceedings of the Physical Society of London Section A* 1949;62(353):301-306.
54. Hahn EL. An Accurate Nuclear Magnetic Resonance Method for Measuring Spin-Lattice Relaxation Times. *Physical Review* 1949;76(1):145-146.
55. Barral JK, Gudmundson E, Stikov N, Etezadi-Amoli M, Stoica P, Nishimura DG. A robust methodology for in vivo T1 mapping. *Magn Reson Med* 2010;64(4):1057-1067.
56. Stikov N, Boudreau M, Levesque IR, Tardif CL, Barral JK, Pike GB. On the accuracy of T1 mapping: searching for common ground. *Magn Reson Med* 2015;73(2):514-522.
57. Look DC, Locker DR. Time Saving in Measurement of NMR and EPR Relaxation Times. *Review of Scientific Instruments* 1970;41(2):250-251.
58. Crawley AP, Henkelman RM. A comparison of one-shot and recovery methods in T1 imaging. *Magn Reson Med* 1988;7(1):23-34.
59. Marques JP, Kober T, Krueger G, van der Zwaag W, Van de Moortele PF, Gruetter R. MP2RAGE, a self bias-field corrected sequence for improved segmentation and T1-mapping at high field. *Neuroimage* 2010;49(2):1271-1281.
60. Kober T, Granziera C, Ribes D, Browaeys P, Schluerp M, Meuli R, Frackowiak R, Gruetter R, Krueger G. MP2RAGE Multiple Sclerosis Magnetic Resonance Imaging at 3 T. *Investigative Radiology* 2012;47(6):346-352.
61. Fram EK, Herfkens RJ, Johnson GA, Glover GH, Karis JP, Shimakawa A, Perkins TG, Pelc NJ. Rapid Calculation of T1 Using Variable Flip Angle Gradient Refocused Imaging. *Magnetic Resonance Imaging* 1987;5(3):201-208.

62. Cheng HL, Wright GA. Rapid high-resolution T(1) mapping by variable flip angles: accurate and precise measurements in the presence of radiofrequency field inhomogeneity. *Magn Reson Med* 2006;55(3):566-574.
63. Deoni SC, Rutt BK, Peters TM. Rapid combined T1 and T2 mapping using gradient recalled acquisition in the steady state. *Magn Reson Med* 2003;49(3):515-526.
64. Liberman G, Louzoun Y, Ben Bashat D. T(1) mapping using variable flip angle SPGR data with flip angle correction. *J Magn Reson Imaging* 2014;40(1):171-180.
65. Leppert IR, Narayanan S, Araujo D, Giacomini PS, Lapierre Y, Arnold DL, Pike GB. Interpreting therapeutic effect in multiple sclerosis via MRI contrast enhancing lesions: now you see them, now you don't. *J Neurol* 2014;261(4):809-816.
66. Sung K, Daniel BL, Hargreaves BA. Transmit B1+ field inhomogeneity and T1 estimation errors in breast DCE-MRI at 3 tesla. *J Magn Reson Imaging* 2013;38(2):454-459.
67. Traficante DD. Relaxation. Can T2, be longer than T1? *Concepts in Magnetic Resonance* 1991;3(3):171-177.
68. Anet FAL, O'Leary DJ. The shielding tensor part II: Understanding its strange effects on relaxation. *Concepts in Magnetic Resonance* 1992;4(1):35-52.
69. Budimir J, Skinner JL. On the relationship between T1 and T2 for stochastic relaxation models. *Journal of Statistical Physics* 1987;49(5):1029-1042.
70. Sevian HM, Skinner JL. T2 can be greater than 2T1. *The Journal of Chemical Physics* 1989;91(3):1775-1782.
71. Bojorquez JZ, Bricq S, Acquitter C, Brunotte F, Walker PM, Lalande A. What are normal relaxation times of tissues at 3 T? *Magnetic Resonance Imaging* 2017;35(Supplement C):69-80.
72. Fullerton GD, Potter JL, Dornbluth NC. NMR relaxation of protons in tissues and other macromolecular water solutions. *Magnetic Resonance Imaging* 1982;1(4):209-226.
73. Bloembergen N, Purcell EM, Pound RV. Relaxation Effects in Nuclear Magnetic Resonance Absorption. *Physical Review* 1948;73(7):679-712.
74. Li TQ, Yao B, van Gelderen P, Merkle H, Dodd S, Talagala L, Koretsky AP, Duyn J. Characterization of T(2)* heterogeneity in human brain white matter. *Magn Reson Med* 2009;62(6):1652-1657.
75. Underhill HR, Rostomily RC, Mikheev AM, Yuan C, Yarnykh VL. Fast bound pool fraction imaging of the in vivo rat brain: association with myelin content and validation in the C6 glioma model. *NeuroImage* 2011;54(3):2052-2065.

76. Mackay A, Whittall K, Adler J, Li D, Paty D, Graeb D. In vivo visualization of myelin water in brain by magnetic resonance. *Magnetic Resonance in Medicine* 1994;31(6):673-677.
77. MacKay A, Laule C, Vavasour I, Bjarnason T, Kolind S, Madler B. Insights into brain microstructure from the T2 distribution. *Magn Reson Imaging* 2006;24(4):515-525.
78. Moore GR, Leung E, MacKay AL, Vavasour IM, Whittall KP, Cover KS, Li DK, Hashimoto SA, Oger J, Sprinkle TJ, Paty DW. A pathology-MRI study of the short-T2 component in formalin-fixed multiple sclerosis brain. *Neurology* 2000;55(10):1506-1510.
79. Laule C, Yung A, Pavolva V, Bohnet B, Kozlowski P, Hashimoto SA, Yip S, Li DK, Moore GW. High-resolution myelin water imaging in post-mortem multiple sclerosis spinal cord: A case report. *Mult Scler* 2016;22(11):1485-1489.
80. Alonso-Ortiz E, Levesque IR, Pike GB. MRI-based myelin water imaging: A technical review. *Magnetic Resonance in Medicine* 2015;73(1):70-81.
81. Collins CM, Wang Z. Calculation of radiofrequency electromagnetic fields and their effects in MRI of human subjects. *Magnetic Resonance in Medicine* 2011;65(5):1470-1482.
82. Liu J, Zhang X, Schmitter S, Van de Moortele PF, He B. Gradient-based electrical properties tomography (gEPT): A robust method for mapping electrical properties of biological tissues *in vivo* using magnetic resonance imaging. *Magn Reson Med* 2015;74(3):634-646.
83. Katscher U, Voigt T, Findeklee C, Vernickel P, Nehrke K, Dossel O. Determination of electric conductivity and local SAR via B1 mapping. *IEEE Trans Med Imaging* 2009;28(9):1365-1374.
84. Jin J, Chen J. On the SAR and field inhomogeneity of birdcage coils loaded with the human head. *Magn Reson Med* 1997;38(6):953-963.
85. Sled JG, Pike GB. Standing-wave and RF penetration artifacts caused by elliptic geometry: an electrodynamic analysis of MRI. *IEEE Trans Med Imaging* 1998;17(4):653-662.
86. Van de Moortele P-F, Akgun C, Adriany G, Moeller S, Ritter J, Collins CM, Smith MB, Vaughan JT, Uğurbil K. B1 destructive interferences and spatial phase patterns at 7 T with a head transceiver array coil. *Magnetic Resonance in Medicine* 2005;54(6):1503-1518.
87. Insko EK, Bolinger L. Mapping of the Radiofrequency Field. *Journal of Magnetic Resonance Series A* 1993;103(1):82-85.
88. Stollberger R, Wach P. Imaging of the active B1 field *in vivo*. *Magnetic Resonance in Medicine* 1996;35(2):246-251.

89. Wang J, Qiu M, Constable RT. In vivo method for correcting transmit/receive nonuniformities with phased array coils. *Magn Reson Med* 2005;53(3):666-674.
90. Samson RS, Wheeler-Kingshott CA, Symms MR, Tozer DJ, Tofts PS. A simple correction for B1 field errors in magnetization transfer ratio measurements. *Magn Reson Imaging* 2006;24(3):255-263.
91. Sled JG, Pike GB. Correction for B1 and B0 variations in quantitative T2 measurements using MRI. *Magnetic Resonance in Medicine* 2000;43(4):589-593.
92. Yarnykh VL. Actual flip-angle imaging in the pulsed steady state: a method for rapid three-dimensional mapping of the transmitted radiofrequency field. *Magn Reson Med* 2007;57(1):192-200.
93. Sacolick LI, Wiesinger F, Hancu I, Vogel MW. B1 mapping by Bloch-Siegert shift. *Magn Reson Med* 2010;63(5):1315-1322.
94. Nehrke K. On the steady-state properties of actual flip angle imaging (AFI). *Magn Reson Med* 2009;61(1):84-92.
95. Yarnykh VL. Optimal radiofrequency and gradient spoiling for improved accuracy of T1 and B1 measurements using fast steady-state techniques. *Magn Reson Med* 2010;63(6):1610-1626.
96. Pohmann R, Scheffler K. A theoretical and experimental comparison of different techniques for B(1) mapping at very high fields. *NMR Biomed* 2013;26(3):265-275.
97. Versluis MJ, Tsekos N, Smith NB, Webb AG. Simple RF design for human functional and morphological cardiac imaging at 7tesla. *Journal of Magnetic Resonance* 2009;200(1):161-166.
98. Zhang B, Seifert AC, Kim J-w, Borrello J, Xu J. 7 Tesla 22-channel wrap-around coil array for cervical spinal cord and brainstem imaging. *Magnetic Resonance in Medicine* 2017;78(4):1623-1634.
99. Avdievich NI, Giapitzakis IA, Pfrommer A, Henning A. Decoupling of a tight-fit transceiver phased array for human brain imaging at 9.4T: Loop overlapping rediscovered. *Magn Reson Med* 2017;n/a-n/a.
100. Chavez S, Xiang QS, An L. Understanding phase maps in MRI: a new cutline phase unwrapping method. *IEEE Trans Med Imaging* 2002;21(8):966-977.
101. Clarke WT, Robson MD, Rodgers CT. Bloch-Siegert B1+-mapping for human cardiac 31P-MRS at 7 Tesla. *Magnetic Resonance in Medicine* 2016;76(4):1047-1058.
102. Schneider E, Glover G. Rapid in vivo proton shimming. *Magnetic Resonance in Medicine* 1991;18(2):335-347.

103. Edzes HT, Samulski ET. Cross relaxation and spin diffusion in the proton NMR of hydrated collagen. *Nature* 1977;265(5594):521-523.
104. Edzes HT, Samulski ET. The measurement of cross-relaxation effects in the proton NMR spin-lattice relaxation of water in biological systems: Hydrated collagen and muscle. *Journal of Magnetic Resonance* (1969) 1978;31(2):207-229.
105. Wolff SD, Balaban RS. Magnetization transfer contrast (MTC) and tissue water proton relaxation in vivo. *Magn Reson Med* 1989;10(1):135-144.
106. Levesque IR, Pike GB. Characterizing healthy and diseased white matter using quantitative magnetization transfer and multicomponent T(2) relaxometry: A unified view via a four-pool model. *Magn Reson Med* 2009;62(6):1487-1496.
107. Dixon WT, Engels H, Castillo M, Sardashti M. Incidental magnetization transfer contrast in standard multislice imaging. *Magn Reson Imaging* 1990;8(4):417-422.
108. Santyr GE. Magnetization transfer effects in multislice MR imaging. *Magn Reson Imaging* 1993;11(4):521-532.
109. Berry I, Barker GJ, Barkhof F, Campi A, Dousset V, Franconi J-M, Gass A, Schreiber W, Miller DH, Tofts PS. A multicenter measurement of magnetization transfer ratio in normal white matter. *Journal of Magnetic Resonance Imaging* 1999;9(3):441-446.
110. Horsfield MA, Barker GJ, Barkhof F, Miller DH, Thompson AJ, Filippi M. Guidelines for using quantitative magnetization transfer magnetic resonance imaging for monitoring treatment of multiple sclerosis. *Journal of Magnetic Resonance Imaging* 2003;17(4):389-397.
111. Barker GJ, Schreiber WG, Gass A, Ranjeva JP, Campi A, Waesberghe JHTMv, Franconi J-M, Watt HC, Tofts PS. A standardised method for measuring magnetisation transfer ratio on MR imagers from different manufacturers—the EuroMT sequence. *Magnetic Resonance Materials in Physics, Biology and Medicine* 2005;18(2):76-80.
112. Ropele S, Filippi M, Valsasina P, Korteweg T, Barkhof F, Tofts PS, Samson R, Miller DH, Fazekas F. Assessment and correction of B1-induced errors in magnetization transfer ratio measurements. *Magn Reson Med* 2005;53(1):134-140.
113. Levesque I, Sled JG, Narayanan S, Santos AC, Brass SD, Francis SJ, Arnold DL, Pike GB. The role of edema and demyelination in chronic T1 black holes: a quantitative magnetization transfer study. *J Magn Reson Imaging* 2005;21(2):103-110.
114. Van Waesberghe JHTM, Kamphorst W, De Groot CJA, Van Walderveen MAA, Castelijns JA, Ravid R, Lycklama à Nijeholt GJ, Van Der Valk P, Polman CH, Thompson AJ, Barkhof F. Axonal loss in multiple sclerosis lesions: Magnetic resonance imaging insights into substrates of disability. *Annals of Neurology* 1999;46(5):747-754.

115. Dousset V, Gayou A, Brochet B, Caille J-M. Early structural changes in acute MS lesions assessed by serial magnetization transfer studies. *Neurology* 1998;51(4):1150-1155.
116. Chen JT, Collins DL, Atkins HL, Freedman MS, Arnold DL. Magnetization transfer ratio evolution with demyelination and remyelination in multiple sclerosis lesions. *Annals of Neurology* 2008;63(2):254-262.
117. Altmann DR, Button T, Schmierer K, Hunter K, Tozer DJ, Wheeler-Kingshott CA, Coles A, Miller DH. Sample sizes for lesion magnetisation transfer ratio outcomes in remyelination trials for multiple sclerosis. *Multiple Sclerosis and Related Disorders* 2014;3(2):237-243.
118. Traboulsee A, Dehmeshki J, Peters KR, Griffin CM, Brex PA, Silver N, Ciccarrelli O, Chard DT, Barker GJ, Thompson AJ, Miller DH. Disability in multiple sclerosis is related to normal appearing brain tissue MTR histogram abnormalities. *Multiple Sclerosis Journal* 2003;9(6):566-573.
119. Mangia S, Carpenter AF, Tyan AE, Eberly LE, Garwood M, Michaeli S. Magnetization transfer and adiabatic T1rho MRI reveal abnormalities in normal-appearing white matter of subjects with multiple sclerosis. *Mult Scler* 2014;20(8):1066-1073.
120. Vrenken H, Pouwels PJ, Ropele S, Knol DL, Geurts JJ, Polman CH, Barkhof F, Castelijns JA. Magnetization transfer ratio measurement in multiple sclerosis normal-appearing brain tissue: limited differences with controls but relationships with clinical and MR measures of disease. *Mult Scler* 2007;13(6):708-716.
121. Fisniku LK, Altmann DR, Cercignani M, Tozer DJ, Chard DT, Jackson JS, Miszkiel KA, Schmierer K, Thompson AJ, Miller DH. Magnetization transfer ratio abnormalities reflect clinically relevant grey matter damage in multiple sclerosis. *Mult Scler* 2009;15(6):668-677.
122. Chen JT, Collins DL, Freedman MS, Atkins HL, Arnold DL, Canadian MSBMTSG. Local magnetization transfer ratio signal inhomogeneity is related to subsequent change in MTR in lesions and normal-appearing white-matter of multiple sclerosis patients. *Neuroimage* 2005;25(4):1272-1278.
123. Crespy L, Zaaraoui W, Lemaire M, Rico A, Faivre A, Reuter F, Malikova I, Confort-Gouny S, Cozzzone PJ, Pelletier J, Ranjeva JP, Audoin B. Prevalence of grey matter pathology in early multiple sclerosis assessed by magnetization transfer ratio imaging. *PLoS One* 2011;6(9):e24969.
124. Audoin B, Ranjeva J-P, Duong MVA, Ibarrola D, Malikova I, Confort-Gouny S, Soulier E, Viout P, Ali-Chérif A, Pelletier J, Cozzzone PJ. Voxel-based analysis of MTR images: A method to locate gray matter abnormalities in patients at the earliest stage of multiple sclerosis. *Journal of Magnetic Resonance Imaging* 2004;20(5):765-771.

125. Richert ND, Ostuni JL, Bash CN, Leist TP, McFarland HF, Frank JA. Interferon beta-1b and intravenous methylprednisolone promote lesion recovery in multiple sclerosis. *Multiple Sclerosis Journal* 2001;7(1):49-58.
126. Kita M, Goodkin DE, Bacchetti P, Waubant E, Nelson SJ, Majumdar S. Magnetization transfer ratio in new MS lesions before and during therapy with IFN β -1a. *Neurology* 2000;54(9):1741-1745.
127. Button T, Altmann D, Tozer D, Dalton C, Hunter K, Compston A, Coles A, Miller D. Magnetization transfer imaging in multiple sclerosis treated with alemtuzumab. *Mult Scler* 2013;19(2):241-244.
128. Tao Y, Zhang X, Zivadinov R, Dwyer MG, Kennedy C, Bergsland N, Ramasamy D, Durfee J, Hojnacki D, Hayward B, Dangond F, Weinstock-Guttman B, Markovic-Plese S. Immunologic and MRI markers of the therapeutic effect of IFN-beta-1a in relapsing-remitting MS. *Neurol Neuroimmunol Neuroinflamm* 2015;2(6):e176.
129. Kubicki M, Park H, Westin CF, Nestor PG, Mulkern RV, Maier SE, Niznikiewicz M, Connor EE, Levitt JJ, Frumin M, Kikinis R, Jolesz FA, McCarley RW, Shenton ME. DTI and MTR abnormalities in schizophrenia: analysis of white matter integrity. *Neuroimage* 2005;26(4):1109-1118.
130. Antosik-Biernacka A, Peuskens H, De Hert M, Peuskens J, Sunaert S, Van Hecke P, Goraj B. Magnetization transfer imaging in chronic schizophrenia. *Med Sci Monit* 2006;12(4):MT17-21.
131. Ge Y, Kolson DL, Babb JS, Mannon LJ, Grossman RI. Whole brain imaging of HIV-infected patients: quantitative analysis of magnetization transfer ratio histogram and fractional brain volume. *AJNR Am J Neuroradiol* 2003;24(1):82-87.
132. Fornari E, Maeder P, Meuli R, Ghika J, Knyazeva MG. Demyelination of superficial white matter in early Alzheimer's disease: a magnetization transfer imaging study. *Neurobiol Aging* 2012;33(2):428 e427-419.
133. Chen Z, Zhang H, Jia Z, Zhong J, Huang X, Du M, Chen L, Kuang W, Sweeney JA, Gong Q. Magnetization transfer imaging of suicidal patients with major depressive disorder. *Sci Rep* 2015;5:9670.
134. Helms G, Dathe H, Kallenberg K, Dechent P. High-resolution maps of magnetization transfer with inherent correction for RF inhomogeneity and T1 relaxation obtained from 3D FLASH MRI. *Magnetic Resonance in Medicine* 2008;60(6):1396-1407.
135. Helms G, Dathe H, Kallenberg K, Dechent P. High-resolution maps of magnetization transfer with inherent correction for RF inhomogeneity and T1 relaxation obtained from 3D FLASH MRI (vol 60, pg 1396, 2008). *Magnetic Resonance in Medicine* 2010;64(6):1856-1856.

136. Lema A, Bishop C, Malik O, Mattoscio M, Ali R, Nicholas R, Muraro PA, Matthews PM, Waldman AD, Newbould RD. A Comparison of Magnetization Transfer Methods to Assess Brain and Cervical Cord Microstructure in Multiple Sclerosis. *Journal of Neuroimaging* 2017;27(2):221-226.
137. Campbell JSW, Leppert IR, Narayanan S, Boudreau M, Duval T, Cohen-Adad J, Pike GB, Stikov N. Promise and pitfalls of g-ratio estimation with MRI. *NeuroImage* 2017.
138. Mohammadi S, Carey D, Dick F, Diedrichsen J, Sereno MI, Reisert M, Callaghan MF, Weiskopf N. Whole-Brain In-vivo Measurements of the Axonal G-Ratio in a Group of 37 Healthy Volunteers. *Frontiers in Neuroscience* 2015;9(441).
139. Helms G, Draganski B, Frackowiak R, Ashburner J, Weiskopf N. Improved segmentation of deep brain grey matter structures using magnetization transfer (MT) parameter maps. *NeuroImage* 2009;47(1):194-198.
140. Helms G. Volume correction for edema in single-volume proton MR spectroscopy of contrast-enhancing multiple sclerosis lesions. *Magn Reson Med* 2001;46(2):256-263.
141. Solomon I. Relaxation Processes in a System of Two Spins. *Physical Review* 1955;99(2):559-565.
142. Bloembergen N, Shapiro S, Pershan PS, Artman JO. Cross-Relaxation in Spin Systems. *Physical Review* 1959;114(2):445-459.
143. Henkelman RM, Huang X, Xiang QS, Stanisz GJ, Swanson SD, Bronskill MJ. Quantitative interpretation of magnetization transfer. *Magn Reson Med* 1993;29(6):759-766.
144. Sled JG, Pike GB. Quantitative interpretation of magnetization transfer in spoiled gradient echo MRI sequences. *Journal of Magnetic Resonance* 2000;145(1):24-36.
145. Sled JG, Pike GB. Quantitative imaging of magnetization transfer exchange and relaxation properties in vivo using MRI. *Magn Reson Med* 2001;46(5):923-931.
146. Morrison C, Henkelman RM. A model for magnetization transfer in tissues. *Magn Reson Med* 1995;33(4):475-482.
147. Hu BS, Conolly SM, Wright GA, Nishimura DG, Macovski A. Pulsed saturation transfer contrast. *Magnetic Resonance in Medicine* 1992;26(2):231-240.
148. Pike GB, Glover GH, Hu BS, Enzmann DR. Pulsed magnetization transfer spin-echo MR imaging. *Journal of Magnetic Resonance Imaging* 1993;3(3):531-539.
149. Listerud J. Off-resonance pulsed magnetization transfer in clinical MR imaging: Optimization by an analysis of transients. *Magnetic Resonance in Medicine* 1997;37(5):693-705.

150. Ramani A, Dalton C, Miller DH, Tofts PS, Barker GJ. Precise estimate of fundamental in-vivo MT parameters in human brain in clinically feasible times. *Magn Reson Imaging* 2002;20(10):721-731.
151. Yarnykh VL. Pulsed Z-spectroscopic imaging of cross-relaxation parameters in tissues for human MRI: theory and clinical applications. *Magn Reson Med* 2002;47(5):929-939.
152. Portnoy S, Stanisz GJ. Modeling pulsed magnetization transfer. *Magn Reson Med* 2007;58(1):144-155.
153. Cabana J-F, Gu Y, Boudreau M, Levesque IR, Atchia Y, Sled JG, Narayanan S, Arnold DL, Pike GB, Cohen-Adad J, Duval T, Vuong M-T, Stikov N. Quantitative magnetization transfer imaging made easy with qMTLab: Software for data simulation, analysis, and visualization. *Concepts in Magnetic Resonance Part A* 2015;44A(5):263-277.
154. Levesque IR, Giacomini PS, Narayanan S, Ribeiro LT, Sled JG, Arnold DL, Pike GB. Quantitative magnetization transfer and myelin water imaging of the evolution of acute multiple sclerosis lesions. *Magn Reson Med* 2010;63(3):633-640.
155. Sled JG, Levesque I, Santos AC, Francis SJ, Narayanan S, Brass SD, Arnold DL, Pike GB. Regional variations in normal brain shown by quantitative magnetization transfer imaging. *Magnetic Resonance in Medicine* 2004;51(2):299-303.
156. Levesque IR, Sled JG, Narayanan S, Giacomini PS, Ribeiro LT, Arnold DL, Pike GB. Reproducibility of quantitative magnetization-transfer imaging parameters from repeated measurements. *Magn Reson Med* 2010;64(2):391-400.
157. Rausch M, Tofts P, Lervik P, Walmsley A, Mir A, Schubart A, Seabrook T. Characterization of white matter damage in animal models of multiple sclerosis by magnetization transfer ratio and quantitative mapping of the apparent bound proton fraction f. *Mult Scler* 2009;15(1):16-27.
158. Turati L, Moscatelli M, Mastropietro A, Dowell NG, Zucca I, Erbetta A, Cordigliero C, Brenna G, Bianchi B, Mantegazza R, Cercignani M, Baggi F, Minati L. In vivo quantitative magnetization transfer imaging correlates with histology during de- and remyelination in cuprizone-treated mice. *NMR Biomed* 2015;28(3):327-337.
159. Giulietti G, Bozzali M, Figura V, Spano B, Perri R, Marra C, Lacidogna G, Giubilei F, Caltagirone C, Cercignani M. Quantitative magnetization transfer provides information complementary to grey matter atrophy in Alzheimer's disease brains. *Neuroimage* 2012;59(2):1114-1122.
160. Arlinghaus LR, Dortch RD, Whisenant JG, Kang H, Abramson RG, Yankeelov TE. Quantitative Magnetization Transfer Imaging of the Breast at 3.0 T: Reproducibility in Healthy Volunteers. *Tomography : a journal for imaging research* 2016;2(4):260-266.
161. Stikov N, Keenan KE, Pauly JM, Smith RL, Dougherty RF, Gold GE. Cross-relaxation imaging of human articular cartilage. *Magn Reson Med* 2011;66(3):725-734.

162. Stikov N, Campbell JS, Stroh T, Lavelee M, Frey S, Novek J, Nuara S, Ho MK, Bedell BJ, Dougherty RF, Leppert IR, Boudreau M, Narayanan S, Duval T, Cohen-Adad J, Picard PA, Gasecka A, Cote D, Pike GB. In vivo histology of the myelin g-ratio with magnetic resonance imaging. *Neuroimage* 2015;118:397-405.
163. Bajd F, Škrlep M, Čandek-Potokar M, Vidmar J, Serša I. Application of quantitative magnetization transfer magnetic resonance imaging for characterization of dry-cured hams. *Meat Science* 2016;122(Supplement C):109-118.
164. Cercignani M, Alexander DC. Optimal acquisition schemes for in vivo quantitative magnetization transfer MRI. *Magn Reson Med* 2006;56(4):803-810.
165. Levesque IR, Sled JG, Pike GB. Iterative optimization method for design of quantitative magnetization transfer imaging experiments. *Magn Reson Med* 2011;66(3):635-643.
166. Lustig M, Donoho D, Pauly JM. Sparse MRI: The application of compressed sensing for rapid MR imaging. *Magn Reson Med* 2007;58(6):1182-1195.
167. Lustig M, Pauly JM. SPIRiT: Iterative self-consistent parallel imaging reconstruction from arbitrary k-space. *Magn Reson Med* 2010;64(2):457-471.
168. Underhill HR, Yuan C, Yarnykh VL. Direct quantitative comparison between cross-relaxation imaging and diffusion tensor imaging of the human brain at 3.0 T. *Neuroimage* 2009;47(4):1568-1578.
169. Gupta RK. New Look at Method of Variable Nutation Angle for Measurement of Spin-Lattice Relaxation-Times Using Fourier-Transform Nmr. *Journal of Magnetic Resonance* 1977;25(1):231-235.
170. Sled JG, Zijdenbos AP, Evans AC. A nonparametric method for automatic correction of intensity nonuniformity in MRI data. *IEEE Trans Med Imaging* 1998;17(1):87-97.
171. Wang J, Qiu M, Kim H, Constable RT. T1 measurements incorporating flip angle calibration and correction in vivo. *J Magn Reson* 2006;182(2):283-292.
172. Collins DL, Zijdenbos A, Baaré WC, Evans A. ANIMAL+INSECT: Improved Cortical Structure Segmentation. In: Kuba A, Šámal M, Todd-Pokropek A, editors. *Information Processing in Medical Imaging*. Volume 1613, Lecture Notes in Computer Science: Springer Berlin Heidelberg; 1999. p 210-223.
173. Lutti A, Hutton C, Finsterbusch J, Helms G, Weiskopf N. Optimization and validation of methods for mapping of the radiofrequency transmit field at 3T. *Magn Reson Med* 2010;64(1):229-238.
174. Liu T, Wisniewski C, Lou M, Chen W, Spincemaille P, Wang Y. Nonlinear formulation of the magnetic field to source relationship for robust quantitative susceptibility mapping. *Magn Reson Med* 2013;69(2):467-476.

175. Morrell GR, Schabel MC. An analysis of the accuracy of magnetic resonance flip angle measurement methods. *Physics in Medicine & Biology* 2010;55(20):6157-6174.
176. Park DJ, Bangerter NK, Javed A, Kaggie J, Khalighi MM, Morrell GR. A statistical analysis of the Bloch-Siegert B1 mapping technique. *Physics in Medicine & Biology* 2013;58(16):5673-5691.
177. Balezeau F, Eliat PA, Cayamo AB, Saint-Jalmes H. Mapping of low flip angles in magnetic resonance. *Physics in Medicine & Biology* 2011;56(20):6635-6647.
178. Lutti A, Weiskopf N. Optimizing the accuracy of T1 mapping accounting for RF nonlinearities and spoiling characteristics in FLASH imaging. abstract 2478; 2014; Milan. (abstract 2478).
179. Parker GJ, Barker GJ, Tofts PS. Accurate multislice gradient echo T(1) measurement in the presence of non-ideal RF pulse shape and RF field nonuniformity. *Magn Reson Med* 2001;45(5):838-845.
180. Mitsouras D, Mulkern RV, Rybicki FJ. Strategies for inner volume 3D fast spin echo magnetic resonance imaging using nonselective refocusing radio frequency pulses. *Med Phys* 2006;33(1):173-186.
181. Helms G, Finsterbusch J, Weiskopf N, Dechent P. Rapid radiofrequency field mapping in vivo using single-shot STEAM MRI. *Magn Reson Med* 2008;60(3):739-743.
182. Kellner E, Dhital B, Kiselev VG, Reisert M. Gibbs-ringing artifact removal based on local subvoxel-shifts. *Magn Reson Med* 2016;76(5):1574-1581.
183. Nehrke K, Bornert P. Eigenmode analysis of transmit coil array for tailored B1 mapping. *Magn Reson Med* 2010;63(3):754-764.
184. Saranathan M, Khalighi MM, Glover GH, Pandit P, Rutt BK. Efficient Bloch-Siegert B1 (+) mapping using spiral and echo-planar readouts. *Magn Reson Med* 2013;70(6):1669-1673.
185. Lutti A, Stadler J, Josephs O, Windischberger C, Speck O, Bernarding J, Hutton C, Weiskopf N. Robust and fast whole brain mapping of the RF transmit field B1 at 7T. *PLoS One* 2012;7(3):e32379.
186. Lutti A, Dick F, Sereno MI, Weiskopf N. Using high-resolution quantitative mapping of R1 as an index of cortical myelination. *NeuroImage* 2014;93, Part 2:176-188.
187. Schmierer K, Wheeler-Kingshott CAM, Tozer DJ, Boulby PA, Parkes HG, Yousry TA, Scaravilli F, Barker GJ, Tofts PS, Miller DH. Quantitative magnetic resonance of postmortem multiple sclerosis brain before and after fixation. *Magnetic Resonance in Medicine* 2008;59(2):268-277.

188. Tozer D, Ramani A, Barker GJ, Davies GR, Miller DH, Tofts PS. Quantitative magnetization transfer mapping of bound protons in multiple sclerosis. *Magn Reson Med* 2003;50(1):83-91.
189. Davies GR, Tozer DJ, Cercignani M, Ramani A, Dalton CM, Thompson AJ, Barker GJ, Tofts PS, Miller DH. Estimation of the macromolecular proton fraction and bound pool T2 in multiple sclerosis. *Mult Scler* 2004;10(6):607-613.
190. Gloor M, Scheffler K, Bieri O. Quantitative magnetization transfer imaging using balanced SSFP. *Magn Reson Med* 2008;60(3):691-700.
191. Dortch RD, Li K, Gochberg DF, Welch EB, Dula AN, Tamhane AA, Gore JC, Smith SA. Quantitative magnetization transfer imaging in human brain at 3 T via selective inversion recovery. *Magn Reson Med* 2011;66(5):1346-1352.
192. Pike GB. Pulsed magnetization transfer contrast in gradient echo imaging: a two-pool analytic description of signal response. *Magn Reson Med* 1996;36(1):95-103.
193. Cercignani M, Symms MR, Schmieder K, Boulby PA, Tozer DJ, Ron M, Tofts PS, Barker GJ. Three-dimensional quantitative magnetisation transfer imaging of the human brain. *NeuroImage* 2005;27(2):436-441.
194. Levesque IR, Chia CL, Pike GB. Reproducibility of in vivo magnetic resonance imaging-based measurement of myelin water. *J Magn Reson Imaging* 2010;32(1):60-68.
195. Cruz JB. System sensitivity analysis: Dowden, Hutchinson & Ross; 1973.
196. Grad J, Mendelson D, Hyder F, Bryant RG. Applications of nuclear magnetic cross-relaxation spectroscopy to tissues. *Magn Reson Med* 1991;17(2):452-459.
197. Skinner TE, Glover GH. An extended two-point Dixon algorithm for calculating separate water, fat, and B0 images. *Magn Reson Med* 1997;37(4):628-630.
198. Yarnykh VL. Fast macromolecular proton fraction mapping from a single off-resonance magnetization transfer measurement. *Magn Reson Med* 2012;68(1):166-178.
199. Wiggins GC, Triantafyllou C, Potthast A, Reykowski A, Nittka M, Wald LL. 32-channel 3 Tesla receive-only phased-array head coil with soccer-ball element geometry. *Magn Reson Med* 2006;56(1):216-223.
200. Caines GH, Schleich T, Rydzewski JM. Incorporation of magnetization transfer into the formalism for rotating-frame spin-lattice proton NMR relaxation in the presence of an off-resonance-irradiation field. *Journal of Magnetic Resonance (1969)* 1991;95(3):558-566.
201. Battiston M, Grussu F, Ianus A, Schneider T, Prados F, Fairney J, Ourselin S, Alexander DC, Cercignani M, Gandini Wheeler-Kingshott CAM, Samson RS. An optimized framework for quantitative magnetization transfer imaging of the cervical spinal cord in vivo. *Magn Reson Med* 2017.

202. Boudreau M, Stikov N, Pike GB. B1 -sensitivity analysis of quantitative magnetization transfer imaging. *Magn Reson Med* 2017.
203. Boudreau M, Tardif CL, Stikov N, Sled JG, Lee W, Pike GB. B1 mapping for bias-correction in quantitative T1 imaging of the brain at 3T using standard pulse sequences. *J Magn Reson Imaging* 2017.
204. Lankford CL, Does MD. Propagation of error from parameter constraints in quantitative MRI: Example application of multiple spin echo T2 mapping. *Magn Reson Med* 2017.
205. Mclean M, MacDonald ME, Lebel RM, Boudreau M, Pike B. Accelerated z-Spectrum Imaging. In: Proceedings of the 25th Annual Meeting of ISMRM 2017;25.
206. Baudrexel S, Noth U, Schure JR, Deichmann R. T1 mapping with the variable flip angle technique: A simple correction for insufficient spoiling of transverse magnetization. *Magn Reson Med* 2017.
207. Smith AK, Dortch RD, Dethrage LM, Smith SA. Rapid, high-resolution quantitative magnetization transfer MRI of the human spinal cord. *Neuroimage* 2014;95:106-116.
208. Menzel MI, Tan ET, Khare K, Sperl JI, King KF, Tao XD, Hardy CJ, Marinelli L. Accelerated Diffusion Spectrum Imaging in the Human Brain Using Compressed Sensing. *Magnetic Resonance in Medicine* 2011;66(5):1226-1233.
209. Li W, Griswold M, Yu X. Fast cardiac T1 mapping in mice using a model-based compressed sensing method. *Magn Reson Med* 2012;68(4):1127-1134.
210. Huang C, Graff CG, Clarkson EW, Bilgin A, Altbach MI. T2 mapping from highly undersampled data by reconstruction of principal component coefficient maps using compressed sensing. *Magn Reson Med* 2012;67(5):1355-1366.
211. Zhao B, Lu W, Hitchens TK, Lam F, Ho C, Liang ZP. Accelerated MR parameter mapping with low-rank and sparsity constraints. *Magn Reson Med* 2015;74(2):489-498.
212. Dopfert J, Witte C, Kunth M, Schroder L. Sensitivity enhancement of (Hyper-)CEST image series by exploiting redundancies in the spectral domain. *Contrast Media & Molecular Imaging* 2014;9(1):100-107.
213. Ashburner J, Friston KJ. Nonlinear spatial normalization using basis functions. *Hum Brain Mapp* 1999;7(4):254-266.
214. Ma D, Gulani V, Seiberlich N, Liu K, Sunshine JL, Duerk JL, Griswold MA. Magnetic resonance fingerprinting. *Nature* 2013;495(7440):187-192.
215. Cohen O, Huang S, McMahon MT, Rosen MS, Farrar CT. Rapid and Quantitative Chemical Exchange Saturation Transfer (CEST) Imaging with Magnetic Resonance Fingerprinting (MRF). ArXiv e-prints. Volume 1710; 2017.

